Assessment of Fracture Properties and Rate effects on Fracture of Materials by Micro Scratching: Application to Gas Shale

by

Ange-Therese Akono

Ingenieur Diplomée de l'Ecole Polytechnique (2009)
Ingénieur de l'Ecole Polytechnique (2011)
S. M., Massachusetts Institute of Technology (2011)

Submitted to the Department of Civil and Environmental Engineering
in partial fulfillment of the requirements for the degree of

Doctor of Philosophy

at the

MASSACHUSETTS INSTITUTE OF TECHNOLOGY

September 2013

Signature of Author .....
Department of Civil and Environmental Engineering
August 10, 2013

Certified by.....
Franz-Josef Ulm
Professor of Civil and Environmental Engineering
Thesis Supervisor

Accepted by.....
Heidi M. Nepf
Chairman, Departmental Committee on Graduate Students

Assessment of Fracture Properties and Rate effects on Fracture of Materials by Micro Scratching: Application to Gas Shale

by

Ange-Therese Akono

Submitted to the Department of Civil and Environmental Engineering
on August 10, 2013, in partial fulfillment of the
requirements for the degree of
Doctor of Philosophy

Abstract

Since 1921, several experimental methods have been implemented to measure the Griffith fracture energy. The challenge lies in providing a measure that is intrinsic and invariant with respect to external factors such as specimen geometry, loading conditions and prescribed rates. In this thesis, by combining multi-scale experiments and advanced theoretical modeling, we provide a means to characterize the intrinsic fracture toughness using microscopic scratch tests.

The scratch test consists in plowing and cutting with a scratch device the surface of a weaker material and it is relevant in many fields of science and engineering, ranging from thin films and coatings, to wear of metals and polymers, and strength of rocks. In this thesis, Dimensional Analysis and Advanced Imaging are employed to demonstrate the predominance of fracture processes in scratch tests with a Rockwell C diamond probe. Based on experimental observations, Linear Fracture Mechanics models are developed that utilize an energy-based approach in order to link the scratch forces to the scratch probe geometry and the fracture properties of the scratched material. The analytical models are implemented into inverse experimental methods for the calibration of the scratch probe geometry and for the determination of the fracture toughness. In particular, the method for fracture toughness determination is shown to be precise, accurate and reproducible. This method is then extended to rate-dependent materials in order to decouple creep and fracture and assess the intrinsic fracture toughness. In particular, for homogeneous materials, a handshake is achieved between macroscopic and microscopic scratch tests. Finally this method is applied to gas shale materials, which exhibit a higher degree of complexity, including heterogeneity, anisotropy and rate-dependence. In particular, a strong directionality of the fracture behavior is observed at the microscopic scale, which is also confirmed at the macroscopic scale.

Thus, throughout this work, we elucidate the physical mechanisms of failure underlying scratch tests and build a method for the multi-scale assessment of intrinsic fracture

properties, which is robust, accurate, precise and reproducible, and which is applicable to a wide range of material behaviors. This in turn opens additional venues of application for scratch tests.

Thesis Supervisor: Franz-Josef Ulm
Title: Professor of Civil and Environmental Engineering

Contents

List of Figures

List of Tables

Acknowledgments

I thank Franz-Josef Ulm for being an awesome research supervisor and a continual source of inspiration.

To my mother, Liliane, and my family, I am grateful for your prayers and words of encouragement. I also acknowledge the support of my spiritual family: Pentecostal Tabernacle, AfriLife Group, MIT Graduate Christian Fellowship and Tang Small Group.

I acknowledge my committee members (Prof. Pedro M. Reis, Prof. Herbert H. Einstein and Prof. David M. Parks) for their guidance and insight.

Thank you to the CSH-Hub community and the CEE graduate students, staff and faculty, especially Donna Hudson, Kris Kipp and Jeanette Marchocki for their patience and efficiency.

Special thanks to Nicholas Randall from CSM-Instruments for his vast technical knowledge and expertise about microscopic scratch tests.

I gratefully acknowledge the funding provided by the X-Shale and X-Cem projects, which have made this work possible.

Last but not least, I give thanks to God who has done great things for me.

Part I

General Presentation

Chapter 1

Introduction

1.1 Industrial Context

A scratch test consists in drawing a stylus across the surface of a material under constant, stepwise or linearly increasing vertical load as depicted in Figure. 1-1. The advance in instrumented scratch testing has been motivated by the increasing use of ceramics, metals and polymers and thin films and coatings in industrial, medical and army applications. For instance the field of applications of thin films and coatings[33, 51, 42, 61, 67] includes automotive applications (wheel bearings, polymer varnishes, rubber seals, Diamond Like Carbon-coatings,...), aerospace applications (thermal barrier coatings for gas-turbine engine applications, surface coatings,...) and biomedical applications (dental implants, arterial implants, hip prostheses...). Therefore, there is a crucial need to assess their performance under normal loading conditions. For instance scratches in automotive coatings can lead to a degradation of the optical, aesthetic and mechanical properties [98]. As for metals and ceramics, that are often used under severe conditions including high temperatures, high pressure or highly corrosive environments; it is crucial to study their tribological performance so as to reduce the maintenance work and increase the components' lifetime.

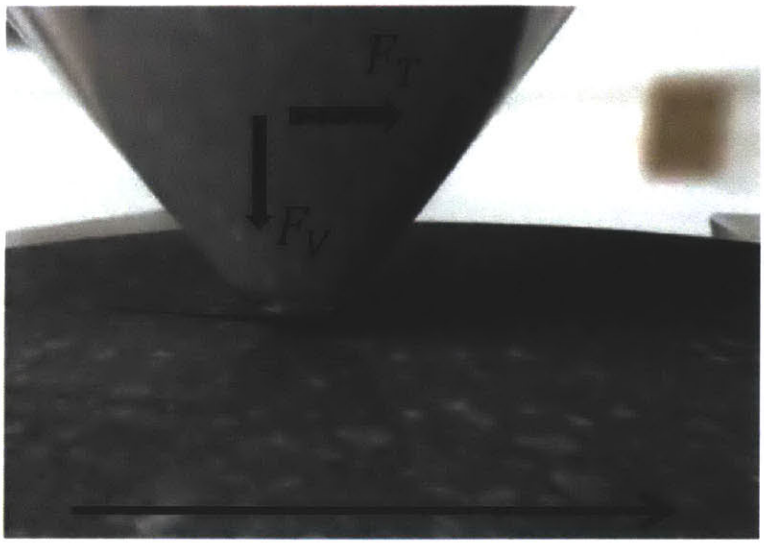

Figure 1-1: Scratch test with an axisymmetric probe.

Typically, a single scratch test under increasing vertical force is used to investigate the failure mechanism and multi-pass scratches under constant vertical force are used to study material wear [26]. Acoustic emission, optical microscopy and friction force measurements are some techniques used to identify and characterize specific failure events during the test. Acoustic emission enables to capture subsurface crack nucleation and crack growth during the test whereas microscopy (optical microscopy or scanning electron microscopy) makes it possible to qualitatively characterize the damage at the surface. Moreover, several analytical models [103, 96, 27] have been developed to quantitatively predict the wear resistance assuming a ductile failure mode. Initially two critical loads where defined: the critical cohesive load L_c that corresponds to the minimum load for crack initiation within the coating and the critical adhesive load L_A that corresponds to coating detachment from substrate. However, further investigations[85, 28, 29] revealed additional failure modes depending on the nature of the coating and the substrate. For instance, plastic deformation prevails at low normal loads in the case of soft coatings on hard substrates, whereas through-coating cracking occurs for hard coatings on hard

substrates. Finally in the case of hard substrates on soft coatings, adhesive failure at the coating-substrate interface, characterized by spalling and buckling, takes place.

The difficulty lies in providing a quantitative and intrinsic measure of the material resistance to fracture. For instance, the "critical load", L_c or L_A, has been shown[52, 88] to depend on extrinsic parameters such as the substrate properties (elasticity, hardness, surface roughness prior to coating), the coating properties (elasticity, hardness, surface roughness) and the friction coefficient between the tip and the coating. There is also a dependence on rate and geometry parameters such as the loading rate, the scratching speed, the indenter tip radius, the diamond tip wear and the machine stiffness and design. This makes it challenging and imperative to come up with innovative scratch-test based methods to characterize the fracture resistance of materials.

1.2 Research Motivation

As said previously, the fast development of thin films and coatings in the past decades has given rise to a high demand for mechanical testing procedures at the micro scale, including fracture toughness testing techniques. At that scale, most conventional fracture testing methods such as the three-point bending tests on single edge notched specimen or the compact tension test do not apply, due to the requirement of having all dimensions at least an order of magnitude greater than the material fracture process zone. In turn, several methods have been developed that evaluate the fracture toughness through micro indentation with a sharp probe. Most popular is the Vickers Indentation Fracture Test where the fracture toughness, K_c, is determined using a Vickers probe and according to:

$$K_c = \alpha \sqrt{\frac{E}{H}} \frac{P}{\sqrt{c_0}}$$

where P is the indentation load, E is the Young's modulus, H is the hardness, c_o is the average length of the radial cracks generated by the indentation and α is a dimensionless constant. Several refinements to the equation above have been put forward so as to

account for the nature of the cracks, the residual stresses and the plastic dissipation inside the material. Although these expressions were derived from a combination of dimensional analysis and empirical observations, they are not supported by a closed-form analytical or by a numerical model. Moreover, indentation fracture testing techniques require considerable care to measure the average length of the cracks that expand from the four corners of the probe. Despite recent advances in optical imaging devices, considerable uncertainties can arise due to the observer skill and subjectivity or due to possible spalling around the indentation impression. The question is then to build an objective and rigorous framework for the characterization of fracture properties at the microscopic scale based on a closed-form analytical model.

1.3 Research Objectives

Our research objective is then to answer the following three questions:

- Can micro scratch tests provide an alternative means to evaluate the fracture toughness of materials?
- What is the influence of the displacement/loading rate on the measured fracture toughness during a scratch test?
- What is the influence of the heterogeneity on the fracture toughness?

Our research approach closely combines multi-scale experiments with advanced analytical tools such as Dimensional Analysis, Linear Fracture Mechanics modeling and numerical simulations.

1.4 Outline of Thesis

This thesis is divided in three parts. The first part investigates physical evidence of fracture processes at work in the scratch tests through dimensional analysis, numerical

simulations and advanced imaging of the residual groove after scratch test. Part II builds analytical models based on Fracture Mechanics to relate the force and depth measurements from the scratch test to the material fracture toughness and the probe geometry considering consecutively a linear elastic isotropic and a linear visco-elastic mechanical behavior. Part III deals with the experimental validation of the analytical models and the development of experimental standards, protocols and procedures for the incorporation of the analytical models in daily scratch testing applications. Finally part III applies the inverse methods to a specific class of materials, shale, characterized by a high anisotropy, heterogeneity and by rate-dependence, in order to identify trends and patterns in the fracture resistance.

Chapter 2

Scratch Test as a Fracture-Driven Process

The scratch test has been used in the industry for over 30 years for a wide range of applications ranging from the adhesion of coatings and thin films to the strength of ceramics [7, 16, 27, 29, 41]. In this chapter, we establish the predominance of fracture processes and determine the shape of the cracks generated during the test. First, we introduce the scratch test technique as well as the apparatus employed to perform the test. Second, Dimensional Analysis and Finite Element simulations enable us to predict the scaling of the horizontal scratch force for both a strength-dominated and a fracture-dominated process. The theoretical predictions are then confronted to experimental measurements to assess the dominant dissipative process. Finally, with optical and scanning electron imaging, we investigate the shape of the cracks generated during a scratch test.

2.1 Scratch Test Technique and Instrumentation

2.1.1 Technique

Scratch test consists of drawing a diamond stylus across the surface of a sample under increasing or constant vertical load. The test presents three phases: 'prescan', 'scratch' and 'panorama'. In the 'prescan' phase a surface profiling is performed at low loads to measure the background profile of the surface of the sample. In the 'scratch' phase, the vertical force is prescribed (constant or linearly increasing) whereas the resulting horizontal force, penetration depth and acoustic emission are simultaneously recorded. The penetration depth is obtained as the difference in displacement of the indenter between the 'prescan' and 'scratch' phase. This allows one to account for any tilt or curvature of the surface. After the first two phases, the sample is brought under an optical microscope to image the residual groove. In particular, in the panorama mode, multiple images are taken along the scratch path and digitally stitched resulting in a panoramic view of the entire scratch that is later synchronized with the measurement taken during the test.

2.1.2 Instrumentation

Scratch test experiments were performed on two platforms: the CSM Intruments Revetest Scratch Tester and the CSM Instruments Micro Scratch Tester illustrated on Figure 2-1 respectively a) and b). Although both apparatus have similar operating principles, they differ in terms of load range and sample positioning system. In particular, the Revetest Scratch Tester has a load capacity of 200 N, much higher than that of the Micro Scratch Tester, 30 N. On both platforms, acoustic emission is detected with a high resolution piezoelectric transducer. Furthermore, both equipments feature a motorized X-Y stage for precise positioning of specimen within 1 μm of lateral resolution and high quality optical microscopes to select the area to be tested. The stylus is mounted to a double cantilever design system that reduces the torsional effect and increases the accuracy of measurement by maintaining the stylus in a vertical plane during the test. This double

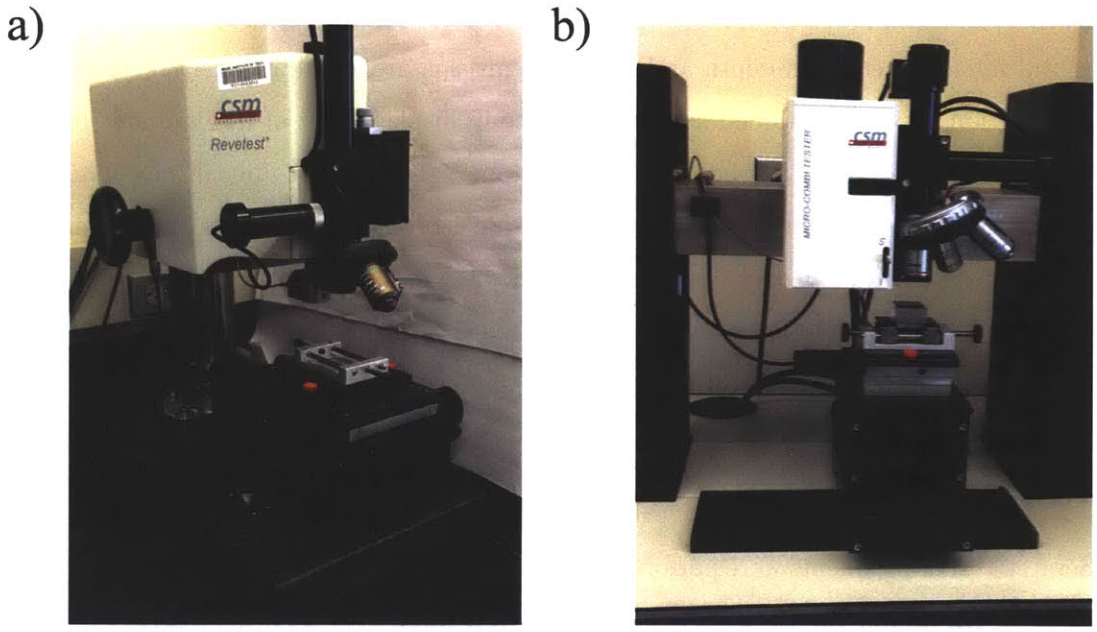

Figure 2-1: Scratch test equipments. a) CSM Instruments Revetest Scratch Tester. b) CSM Instruments Micro Scratch Tester.

Specification	Revetest Scratch Tester	Micro Scratch Tester
Maximal Normal Load	200 N	30 N
Load Resolution	3 mN	0.3 mN
Frame Compliance	0.37 μm	0.79 μm
Maximum Scratch Length	70 mm	120 mm
Scratch Speed	0.4 to 600 mm/min	0.4 to 600 mm/min
Maximum depth	1 mm	1 mm
Resolution	1.5 nm	0.3 nm
XY Stage Resolution	0.25 μm	0.25 μm

Table 2.1: Technical Specifications for the Revetest Scratch Tester and the Micro Scratch Tester. Data courtesy of CSM Instruments [35].

cantilever system is connected to a piezoelectric displacement actuator that monitors the load applied to the displacement head at a high rate, with a response in the order of a few milliseconds. Moreover, an active force-feedback loop that ensures that the load applied remains at the programmed level, yields reproducible test results even with complex geometries such as rough, curved, non-parallel or non-uniform surfaces. Finally, experimental control, data acquisition and preliminary data analysis can be programmed via a computer interface. The technical specifications for the Revetest Scratch Tester and the Micro Scratch Tester are given in Table 2.1. In particular, both equipments are extremely accurate with a load resolution of 0.0015% the maximum possible load and a depth resolution of 0.00015% the maximum possible depth. Moreover, the testing can be performed over a wide range of scratch speeds, spanning three orders of magnitude. Furthermore, the Micro Scratch Tester has a higher force resolution, which makes it adequate for low force testing. In contrast, the Revetest Scratch Tester exhibits a lower frame compliance, which makes it fit for high force testing. In practice, the Revetest Scratch Tester is used to characterize hard materials such as metals, whereas the Micro Scratch Tester is used to characterize soft materials, such as polymers, rocks and cementitious materials.

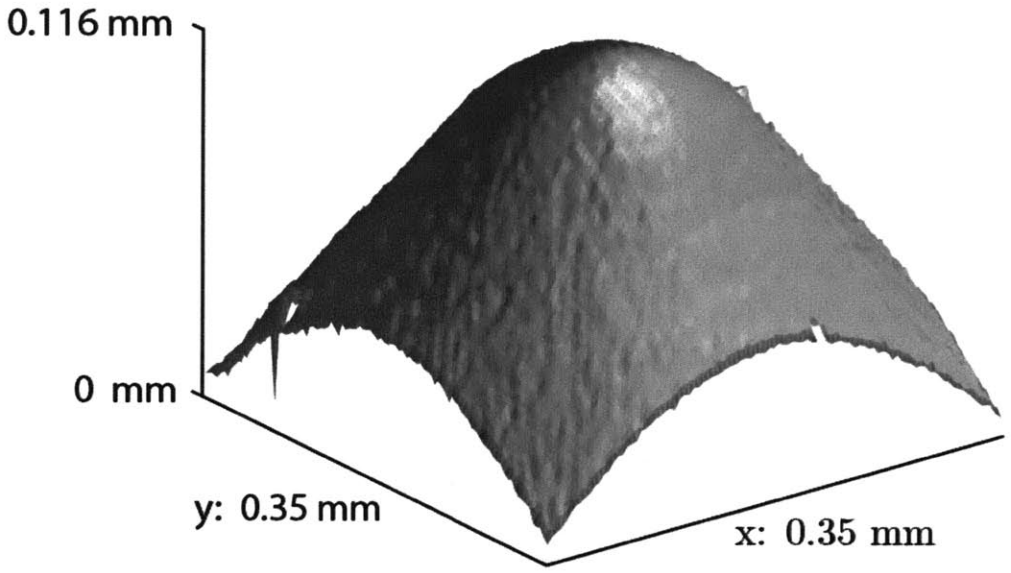

Figure 2-2: 3-D Geometry of a Rockwell diamond indenter with tip radius of 200 μm and a half-apex angle $\theta = 60°$. The picture was obtained using a CSM Instruments ConScan surface profilometer.

2.1.3 Scratch Probe

The probe used for scratch testing is a 200-μm Rockwell diamond indenter, which consists in a cone of half-apex angle θ=60° ending into a hemispherical tip of radius R=200 μm. The transition from the cone to the sphere occurs at a depth of $d_0 = (1 - \sin\theta)R = 0.134\ R = 26.8\ \mu$m. Figure 2-2 represents a 3D image of the tip of the indenter, obtained with a CSM Instruments ConScan surface profilometer. In the next section we introduce basic concepts of Dimensional Analysis and then apply them to characterize the scaling of the horizontal scratch force.

2.2 Dimensional Analysis

Dimensional analysis is a problem-solving method that enables to simplify complex physical problems and has broad application in experiment design or data analysis in several fields of engineering (aerodynamics, hydraulics, astrophysics, etc) [13, 38]. In this section, we apply Dimensional Analysis to express the dependence of the horizontal scratch force F_T in function of relevant parameters such as the geometry of the probe, the probe-material interface, the mechanical material properties and the prescribed loading. The geometry of the scratch probe, Rockwell C, is accounted for via the half-apex angle, θ, and the tip radius, R. The probe-material interface is assumed to be described by Amontons' laws of friction: this means that the friction coefficient, μ, is a material property independent of the contact area [19]. Moreover, we assume the material to be isotropic linear elastic characterized by a Young modulus E and a Poisson's ratio ν. A rate-independent plasticity model with isotropic exponential hardening is used to capture the work hardening at high level of stresses. In particular, three material constants are introduced: yield strength, Y_0, hardening coefficient, H, and hardening exponent, n. The material resistance to fracture propagation is represented by the fracture toughness K_c. Finally, the last category of parameters relates to the loading conditions: neglecting any rate variable we can either choose the depth of penetration d or the prescribed maximal

force $F_{V_{max}}$; however, we cannot choose both as they are not independent. The physical relation we are thus interested in reads as:

$$F_T = f\left(R, \theta, \mu, E, \nu, Y_0, H, n, K_c, d\right) \tag{2.1}$$

2.2.1 Physical Quantities and Dimensions

The basic idea of Dimensional Analysis is that physical laws are independent of the units arbitrarily chosen to measure physical variables. As a result, the mathematical functions expressing physical laws must be homogeneous. This in turn allows us to contract the number of arguments involved in a given relation between physical quantities, by examining the units of measurement of the relevant physical parameters as expressed in a given system of units. For instance, the length/mass/time system is commonly adopted in Newtonian Mechanics. As a consequence, for any physical quantity x, the dimension function denoted by $[x]$, is invariant with respect to the units chosen, and can be shown to be a power function of the base dimension LMT:

$$[x] = L^{\alpha} M^{\beta} T^{\gamma} \tag{2.2}$$

where L, M and T are the dimensions respectively of length, mass and time variables. The exponents α, β and γ are real and associated with x. We can then conveniently summarize the dimension functions of the physical variables of our problem (2.2) in form of a matrix in which the columns list the exponents as expressed in the base dimension:

	$[F_T]$	$[R]$	$[\theta]$	$[\mu]$	$[E]$	$[\nu]$	$[Y]$	$[H]$	$[n]$	$[K_c]$	$[d]$
L	1	1	0	−1	0	0	−1	−1	0	−1/2	1
M	1	0	0	1	0	0	1	1	0	1	0
T	−2	0	0	−2	0	0	−2	−2	0	−2	0

(2.3)

Before proceeding any further, we will introduce the Π-theorem.

2.2.2 Π-Theorem

The Π-theorem resides at the heart of Dimensional Analysis and reduces the number of independent quantities in the problem. It is stated below:

Theorem 1 *Consider a relation between $N+1$ dimensional physical quantities q_0, q_1, $\ldots$,q_N of the form:*

$$q_0 = f(q_1, \cdots, q_N) \tag{2.4}$$

Let k be the number of dimensionally independent variables. Let $\{q_1, \ldots, q_k\}$ be the complete dimensionally independent subset of $\{q_1, \ldots, q_N\}$. The initial physical relation can be reduced to a dimensionless relation between $N-k+1$ similarity parameters Π_0, Π_1, $\ldots$, Π_{N-k}:

$$\Pi_0 = \mathcal{F}(\Pi_1, \ldots, \Pi_{N-k}) \tag{2.5}$$

defined by:

$$\Pi_i = \frac{q_i}{q_1^{a_1^i} q_2^{a_2^i} \cdots q_k^{a_k^i}}; \quad i = 0,\ N-k \tag{2.6}$$

where the exponents a_1^i,$\ldots$,a_i^k are determined from the dimension functions:

$$[q_i] = [q_1]^{a_1^i} [q_2]^{a_2^i} \cdots [q_k]^{a_k^i} \tag{2.7}$$

2.2.3 Application to Scratch Testing

By application of the Π-theorem to the physical relation Eq. (2.1), the rank of the dimension matrix (2.3) is $k = 2$. We can thus choose two dimensionally independent

variables, (K_c, d), and express the others:

$$[F_T] = [K_c][d]^{3/2}; \quad [R] = [K_c]^0[d]^1; \quad [E] = [Y_0] = [H] = [K_c][d]^{-1/2}$$
$$[\theta] = [\mu] = [\nu] = [n] = [K_c]^0[d]^0; \tag{2.8}$$

This allows us to reduce the problem to:

$$\Pi_0 = \frac{F_T}{K_c d^{3/2}} = \mathcal{F}\left(\Pi_1 = \frac{d}{R}, \Pi_2 = \frac{R}{(K_c/Y_0)^2}, \right.$$
$$\left. \Pi_3 = \frac{Y_0}{E}, \Pi_4 = \frac{H}{E}, \Pi_5 = \theta, \Pi_6 = \nu, \Pi_7 = n, \Pi_8 = \mu \right) \tag{2.9}$$

Table 2.2 gives typical numerical values of the invariants $\Pi_2 = R/(K_c/Y_0^2)$ and $\Pi_3 = Y_0/E$ for metals, polymers and ceramics. Π_2 is the ratio of the scratch probe tip radius, R, to a quantity proportional to the fracture process zone of the material, $1/(2\pi)(K_c/Y_0)^2$. Whereas Π_3 is usually two orders of magnitude below unity, Π_2 values span three orders of magnitudes from approximately 10^{-3} for metals to 1 for ceramics. As a consequence, in the ideal case of a purely brittle fracture-driven mechanism, the horizontal force F_T depends only on the fracture toughness, the depth of penetration and the probe half-apex angle and tip radius:

$$\frac{F_T}{K_c d^{3/2}} = \mathcal{F}\left(\frac{d}{R}, \frac{R}{(K_c/Y_0)^2}, \theta, \nu, \mu\right) \tag{2.10}$$

In particular, if the probe is a perfect cone, $(R \to 0)$, then the horizontal force scales as the penetration depth to the power 3/2.

To validate those findings, scratch tests were performed on three polymers with a Vickers probe. The Vickers probe is a square-based pyramidal cone with a half-included angle of $\theta = 68°$ and a tip radius of $R = 150$ nm, which is almost three orders of magnitude smaller than the maximum depth of penetration. The materials considered include amorphous (polycarbonate Lexan 9034 and polyvinylchloride) and semi-crystalline (polyoxymethylene Delrin) polymers. Each test consisted of a series of seven three-millimeter

Material	E (GPa)	Y (MPa)	K_c (MPa$\sqrt{m}$)	Π_2	Π_3
Steel AISI-1045	210	310	50	$7.69\ 10^{-3}$	$1.5\ 10^{-3}$
Lexan 9034	2.5	62	2.8	$9.81\ 10^{-2}$	0.02
Aluminum Oxide	300	250	3.5	1.02	$8.3\ 10^{-4}$

Table 2.2: Typical values of the invariants $\Pi_2 = R/(K_c/Y_0)^2$ and $\Pi_3 = Y/E$ for a metal (Steel AISI-1045), a polymer (Lexan 9034) and a ceramic (Alumina Oxide). E is the Young's modulus, Y is the yield strength and K_c is the fracture toughness. The indenter radius is $R = 200$ μm.

scratches arranged two-millimeter apart. The prescribed maximum force was 30 N and the scratching speed was 6 mm/min; finally, all tests were performed on the CSM Instruments Micro Scratch Tester, which exhibit a high load resolution convenient for low normal force range (0.01- 30 N). Figure 2-3 displays the evolution of the measured horizontal force in function of the depth of penetration. The microscopic scratch test is seen to be repeatable, because, for each material, all seven tests collapse in a single red curve. The resulting horizontal force increases from 0.01 N to 16.23 N for Lexan, 0.01 N to 16.31 N for polyvinylchloride (PVC) and 0.01 N to 10.76 N for Delrin. The resulting maximum penetration depth is 135.46 μm for Lexan, 118.83 μm for PVC and 108.29 μm for Delrin. In Figure 2-3, the theoretical fracture law scaling in 3/2 is represented by a black line. The power law scaling in 3/2 is valid only for depths of penetration greater than 2 μm. Therefore, these experiments suggest that, during scratch tests with a conical probe, brittle fracture becomes predominant at large depths of penetration. In the next section we investigate the presence of plastic flow by performing numerical simulations with a purely elasto-plastic mechanical behavior.

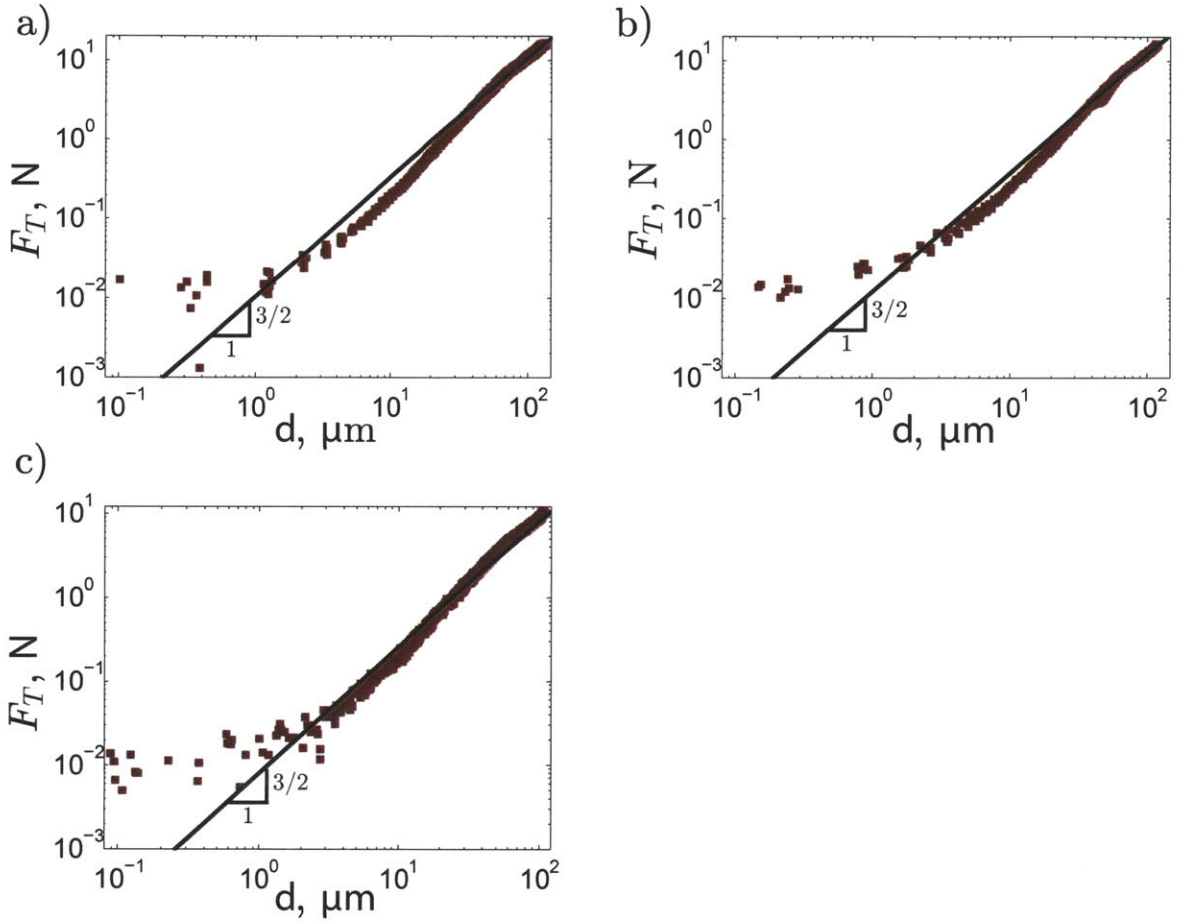

Figure 2-3: Force scaling during a scratch test with a Vickers probe. The experimental measurement is in red and the theoretical fracture scaling in 3/2 is in black. a) Polycarbonate Lexan 9034. b) Polyvinylchloride. c) Polyoxymethylene Delrin.

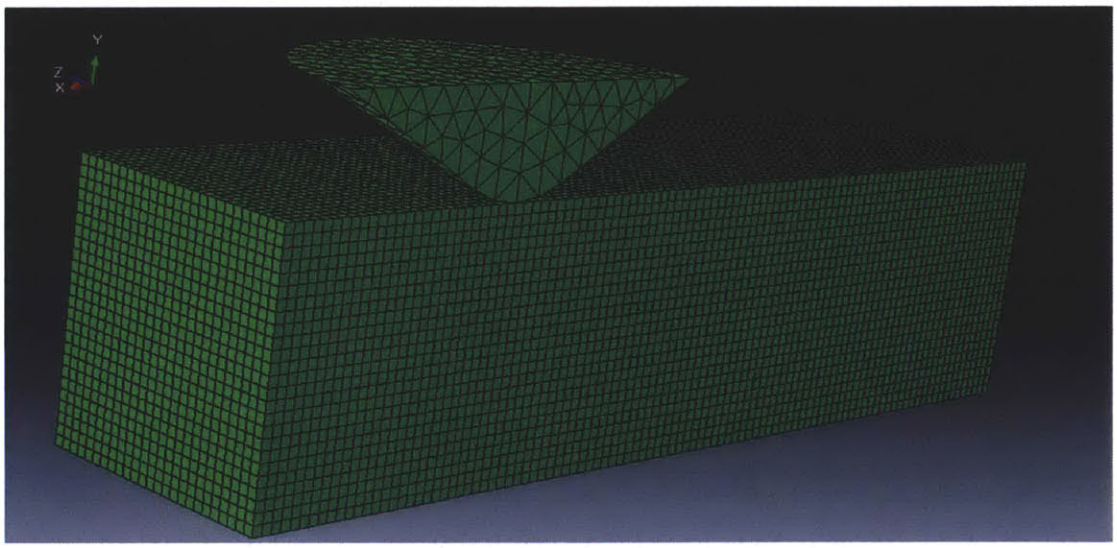

Figure 2-4: 3-D Finite Element mesh for numerical modelling of scratch test in ABAQUS.

2.3 Numerical Simulations of Scratch Tests

2.3.1 Finite Element Model

Three-dimensional simulations were confronted with experiments in order to investigate the predominance of plasticity during scratch tests with a Rockwell C diamond probe. The finite element simulations of scratch tests were performed using ABAQUS (Dassault Systemes, Nanterre, France). To reduce the computation time, only one half of the geometry was modeled as illustrated in Figure 2-5, and symmetric boundary conditions were prescribed. The probe geometry, an ideal Rockwell C probe, consisted of a cone of half-apex angle 60° ending in a sphere of radius 200 μm and 4-node (C3D4) linear tetrahedron elements were used for meshing. As for the material, it was meshed using either 6-node (C3D6) linear triangular prisms or 8-node 9C3D8R) linear bricks. The contact between the probe and the material was frictionless and the hard contact law was used to model the normal behavior so as to prevent any interpenetration.

During the simulations, the vertical and horizontal displacement of the scratch probe was prescribed. The horizontal and vertical displacement were both set to be linearly increasing from zero to maximum values of ($u_x = 500$ μm, $u_y = -140$ μm) for Lexan and ($u_x = 500$ μm, $u_y = -55$ μm) for Steel AISI-1045. The maximum vertical displacement represents the maximum penetration depth that was reached during micro scratch tests on Lexan (respectively steel AISI-1045) with a Rockwell C probe and a prescribed maximal vertical force of 30 N (respectively 150 N).

2.3.2 Material Properties

Both a soft, Lexan, and a hard, Steel AISI-1045, material behaviors were simulated. Figure 2-5 displays the stress-strain behavior, based on data from the scientific literature [30, 78]. In particular, for steel in uniaxial tension, the behavior is initially linear, followed by strain hardening after a strain of $\varepsilon = 2\%$. As for Lexan in uniaxial compression, the curves at both strain rates, low ($\dot{\varepsilon} = 10^{-3}$ s^{-1}) and high ($\dot{\varepsilon} = 5050$ s^{-1}), exhibit an

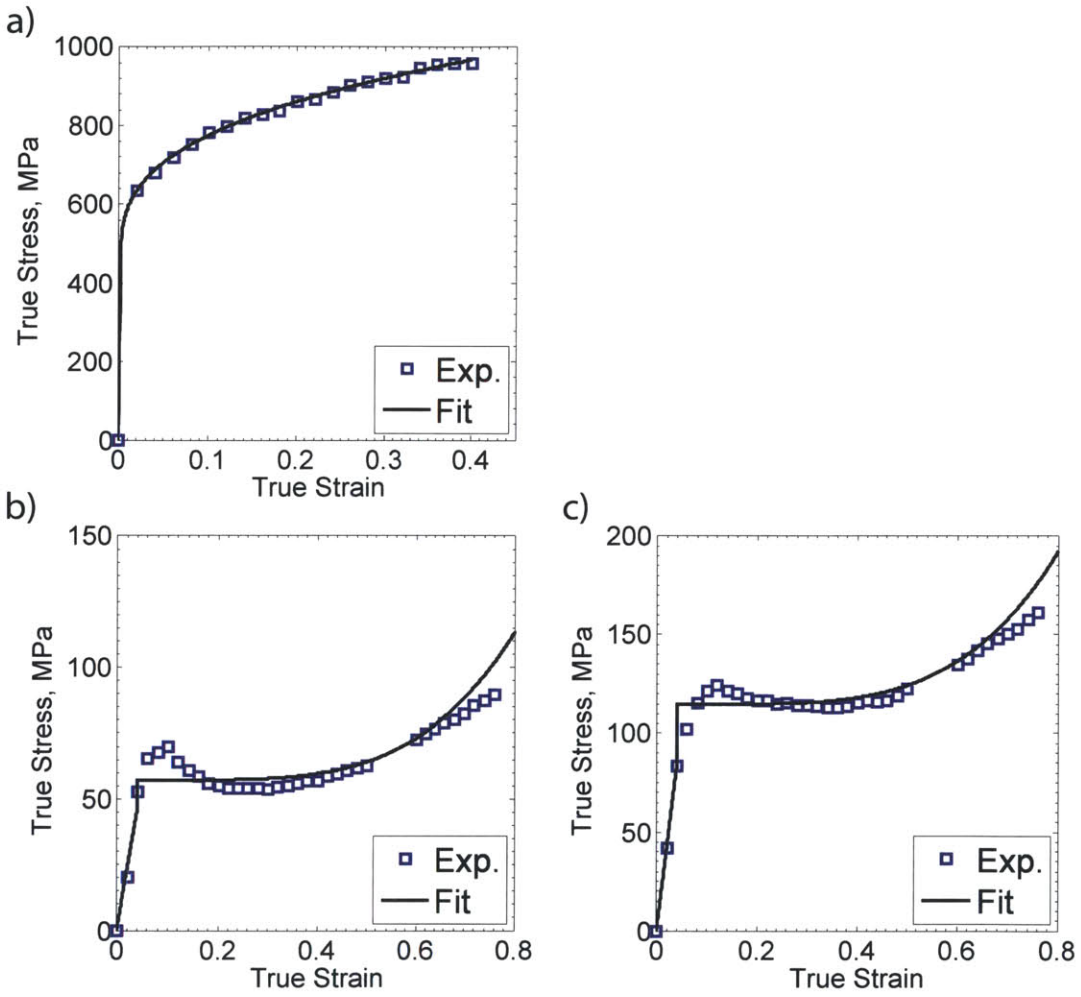

Figure 2-5: Material properties. a) Steel AISI-1045. True stress-true strain curves in uniaxial tension at a strain rate of C. Source [30]. b) Lexan. True stress-true strain curves in uniaxial compression and at low strain rate: $\dot{\varepsilon} = 10^{-3}\ s^{-1}$. Source [78]. c) Lexan. True stress-true strain curves in uniaxial compression and at high strain rate: $\dot{\varepsilon} = 5050\ s^{-1}$. Source [78].

Material	E (GPa)	ν	Y_0 (MPA)	H (MPa)	n
Diamond (probe)	10^3	0.2			
Steel AISI-1045	210	0.33	452	702	0.33
Lexan $\dot{\varepsilon} = 10^{-3}\ s^{-1}$	1.14	0.37	57.2	177.8	4.21
Lexan $\dot{\varepsilon} = 5050\ s^{-1}$	2.09	0.37	114.8	244.5	4.19

Table 2.3: Material elasto-plastic constants used in the numerical simulations of scratch test with a 200 μm Rockwell probe. E is the Young's modulus, ν is the Poisson's ratio, Y_0 is the yield strength, H is the hardening coefficient and n is the hardening exponent.

initial linear portion, then a yield peak followed by strain softening and eventual strain hardening at large strains ($\varepsilon > 0.5$). Moreover, the yield peak increases with the strain rates. We choose to represent both materials using a rate-independent plasticity model with isotropic hardening, where the flow strength obeys a power-law hardening relationship of the form: $Y = Y_0 + H\,(\bar{\epsilon}^p)^n$, where $\bar{\epsilon}^p$ is the accumulated plastic distortion, Y_0 is the yield strength, H the hardening coefficient and n the hardening exponent. Table 2.3 lists the elasto-plastic constants for steel AISI-1045 and Lexan that were fitted from data found in the scientific literature [30, 78] and plotted in Figure 2-5. In particular, the Young's modulus for steel AISI-1045 is two orders of magnitude greater than that of Lexan where as the hardening exponent for Lexan is an order of magnitude greater than that of steel AISI-1045.

2.3.3 Results

Figures 2-6 and 2-7 display the residual groove after numerical scratch test. In particular, the ratio of the yield strength to the Young's modulus, Y/E, influences the pattern of deformation. For Lexan, the value is high, $Y_0/E = 0.02$, and this leads to material sink-in behind the scratch probe. Whereas for low values, $Y/E = 0.0015$ for steel AISI-1045, there is a pile-up of material in front of the scratch probe. Similar results were obtained by Bucaille *et al.* [25] who performed numerical simulation of scratch tests on

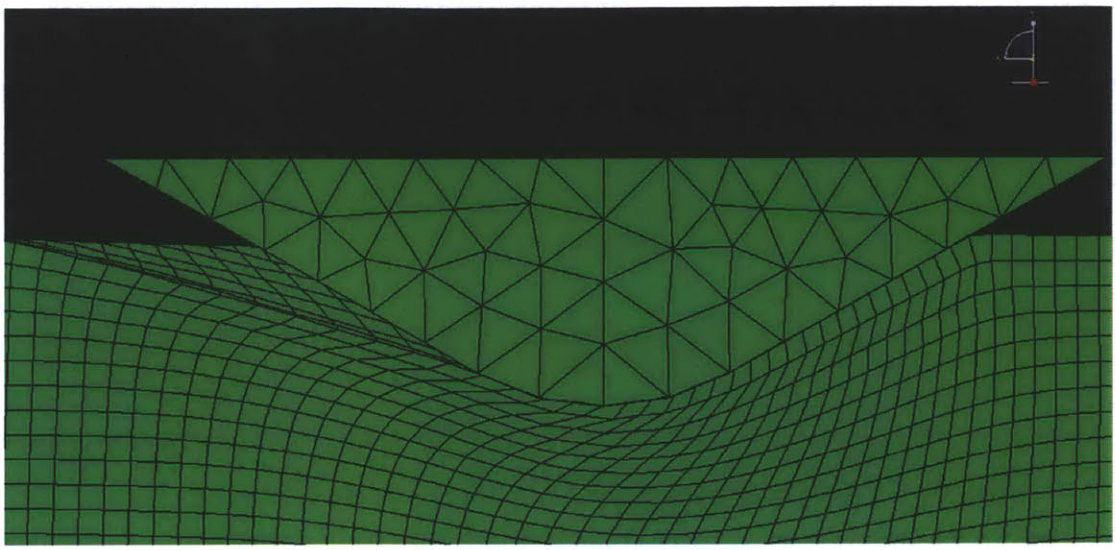

Figure 2-6: Deformed mesh. Numerical simulation of scratch test on Lexan with a 200 μm Rockwell probe assuming a frictionless contact and a high strain rate, $\dot{\epsilon} = 5050\ s^{-1}$.

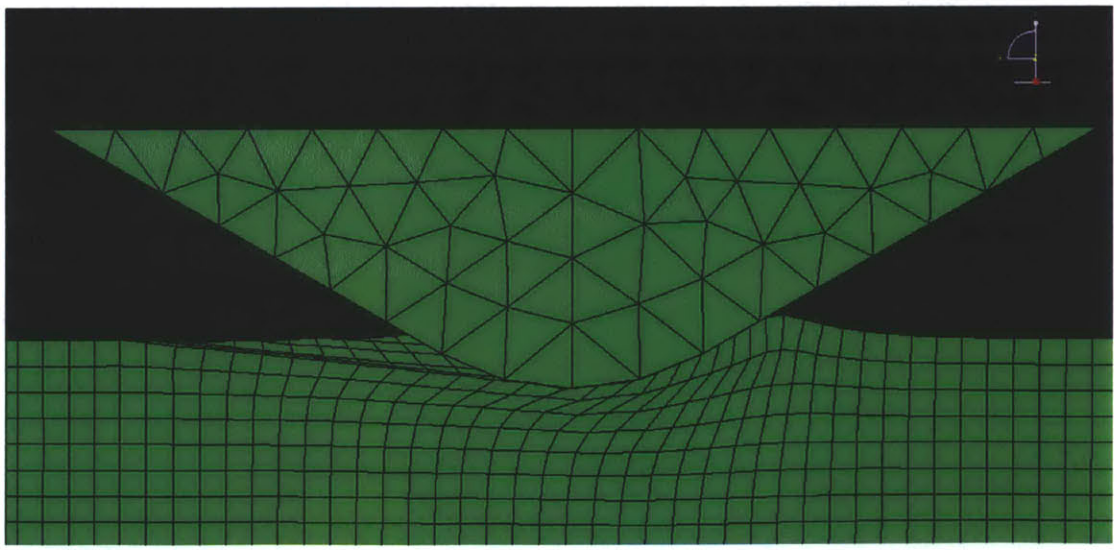

Figure 2-7: Deformed mesh. Numerical simulation of scratch test on steel AISI-1045 with a 200 μm Rockwell probe assuming a frictionless contact.

elasto-plastic materials with a conical probe.

To identify the dominant dissipative mechanism, fracture or plastic flow, the horizontal scratch force $F_T(t)$ and the penetration depth history $d(t)$ were fitted to a power function, $y = ax^b$, for both experiments and numerical simulations. For a strength-dominated process, Dimensional Analysis predicts the following relationship between the horizontal force F_T and the penetration depth d:

$$\frac{F_T}{Y_0 d^2} = \mathcal{F}\left(\frac{d}{R}, \frac{Y_0}{E}, \frac{H}{E}, \theta, \nu, \mu\right) \tag{2.11}$$

Meanwhile, for fracture-driven process the scratch force, F_T, is a cubic function of the penetration depth, d, as expressed in Eq. (2.10).

Figure 2-8 displays the horizontal force, F_T, versus the penetration depth, d. For steel AISI-1045, F_T steadily increases with the penetration depth. Whereas for Lexan, F_T increases and then reaches a plateau for penetration depths greater than 100 μm. This saturation of the force signal might be due to the hardening exponent, n, which is an order magnitude greater for Lexan ($n = 4.21$ for low strain rate and $n = 4.19$ for high strain rate) than for steel AISI-1045 ($n = 0.33$). Moreover, for both Lexan and steel, the horizontal force, F_T, admits an horizontal initial tangent due to prescribed frictionless contact conditions.

For both Lexan and steel AISI-1045, the numerical simulations predict a scaling of the scratch force, F_T, close to d^2; with the penetration depth, d, being equal to the displacement of the scratch probe, as is the case in experiments. In fact, numerical simulations on Lexan yield a power law exponent, b, equal to 2.34, assuming a slow strain rate ($\dot{\varepsilon} = 10^{-3}\ s^{-1}$), and equal to 2.47, assuming a high strain rate ($\dot{\varepsilon} = 5050\ s^{-1}$). As for steel AISI-1045, the simulated power law coefficient, b, is 1.91.

In parallel to numerical simulations, micro scratch tests were performed on both Lexan and steel AISI-1045 with a maximum vertical force of 30 N and 150 N, respectively. The resulting horizontal force- penetration depth curves are also displayed in Figure 2-8. In particular, the experimental scratch force for both materials, Lexan and steel

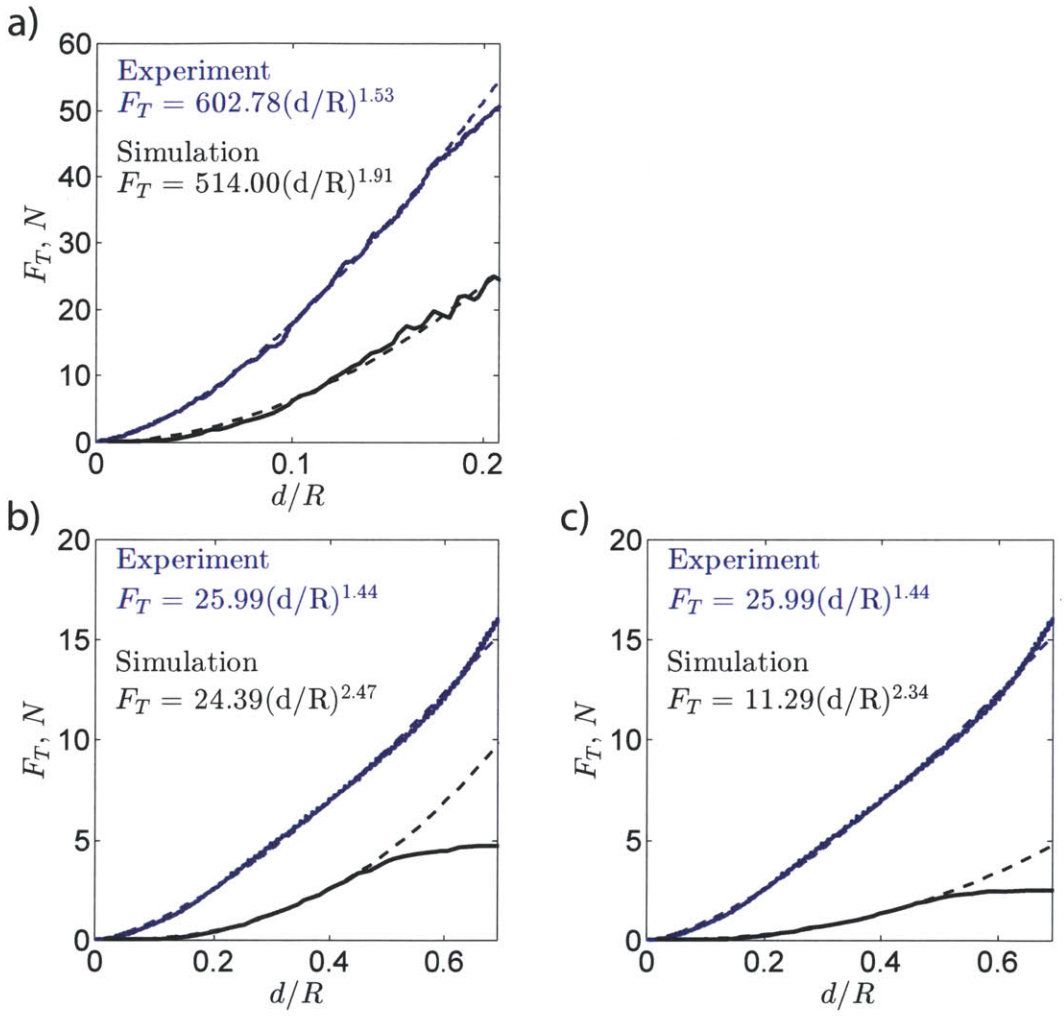

Figure 2-8: Scaling of the horizontal force, F_T. Numerical simulations of scratch test with a 200 μm Rockwell probe. a) Steel AISI-1045. b) Lexan - high strain rate $\dot{\epsilon} = 550\ s^{-1}$. c) Lexan - low strain rate $\dot{\epsilon} = 10^{-3}\ s^{-1}$.

AISI-1045, exhibits a scaling in $d^{3/2}$, characteristic of a fracture-dominated process. The exponent b calculated from micro-scratch tests measurements is 1.44 for Lexan and 1.53 for steel AISI-1045. The Finite Element simulations of scratch tests slightly differ from the experiments in that the vertical displacement (and not the vertical force) is prescribed and frictionless conditions are assumed. Nevertheless, these simulations capture the essence of scratch tests, pushing a hard probe across the surface of a softer material, and therefore can provide meaningful insights in the physics of the test. Based on the Dimensional Analysis and the Finite Element simulations, we conclude that a scaling of the scratch force in $d^{3/2}$ is an indicator of the predominance of fracture processes during scratch testing. Moreover the evidence presented supports the assumption that crack propagation is the main dissipative process in scratch tests with a Rockwell C diamond probe and for penetration depths in the conical range: $d_{max} = 55$ μm for steel AISI-1045 and $d_{max} = 140$ μm for Lexan. In the next section, we investigate the pattern of crack formation with optical imaging and scanning electron microscopy.

2.4 Imaging of the Crack

Optical imaging and scanning electron imaging were used to look for physical cracks on the residual groove after scratch tests. Scratch tests were performed on alumina using a 200 μm Rockwell diamond probe on the CSM Instruments Revetest Scratch Tester. Alumina was purchased from Accuratus (Phillisburg, NJ) as a cylinder of 25 mm diameter and 12 mm height. Prior to testing, the specimen was polished on a rotating lapping plate using a Texmet P polishing cloth, and a diamond suspension oil solution using the following abrasive sizes: 15, 9 and 1 μm. Afterward, a scratch test was carried out with a maximum vertical force of 30 N and a scratch speed of 6 mm/min. After scratch testing, pictures of the residual groove were taken using the CSM Instruments Micro Scratch Tester optical microscope, at a magnification level of 800X. At the beginning of the scratch the surface is almost-crack free. However, as the probe moves deeper into

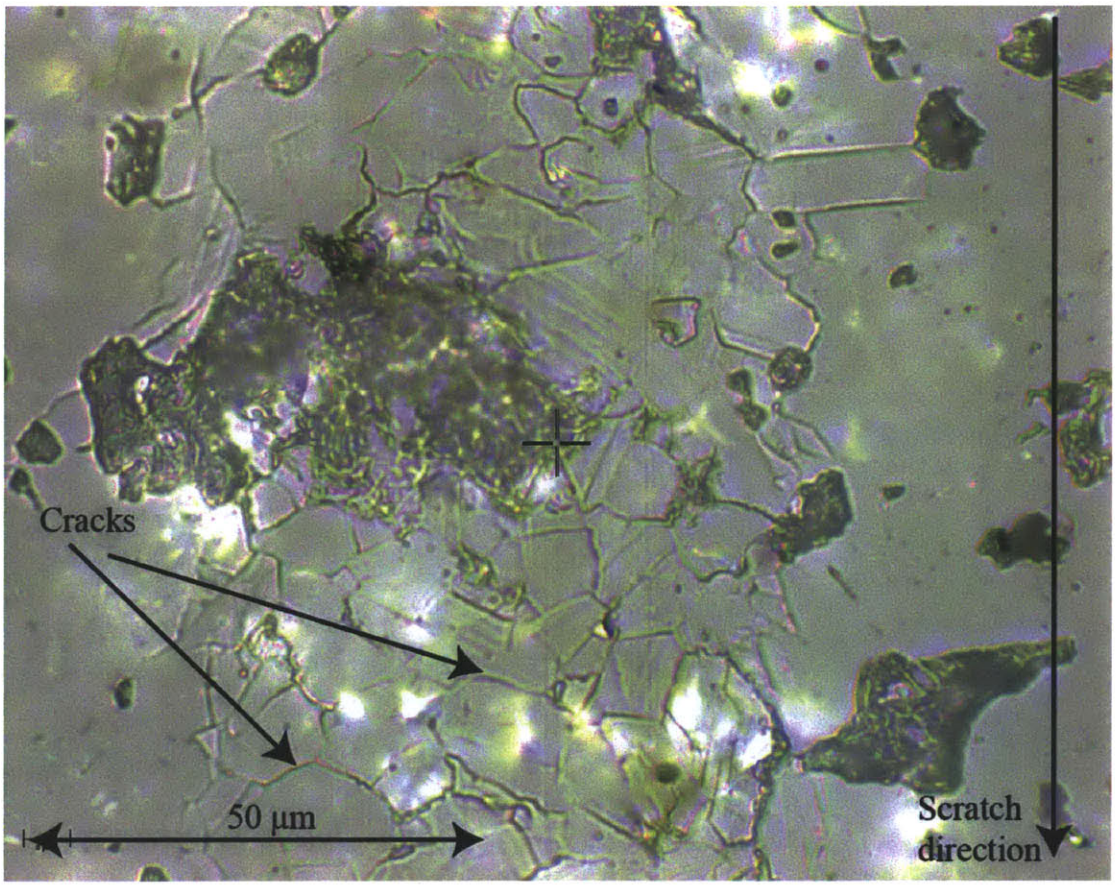

Figure 2-9: Cracks on residual grooves. Scratch tests on alumina with a maximal penetration depth of $d_{max} = 15\mu$m. The arrow indicates the scratch direction.

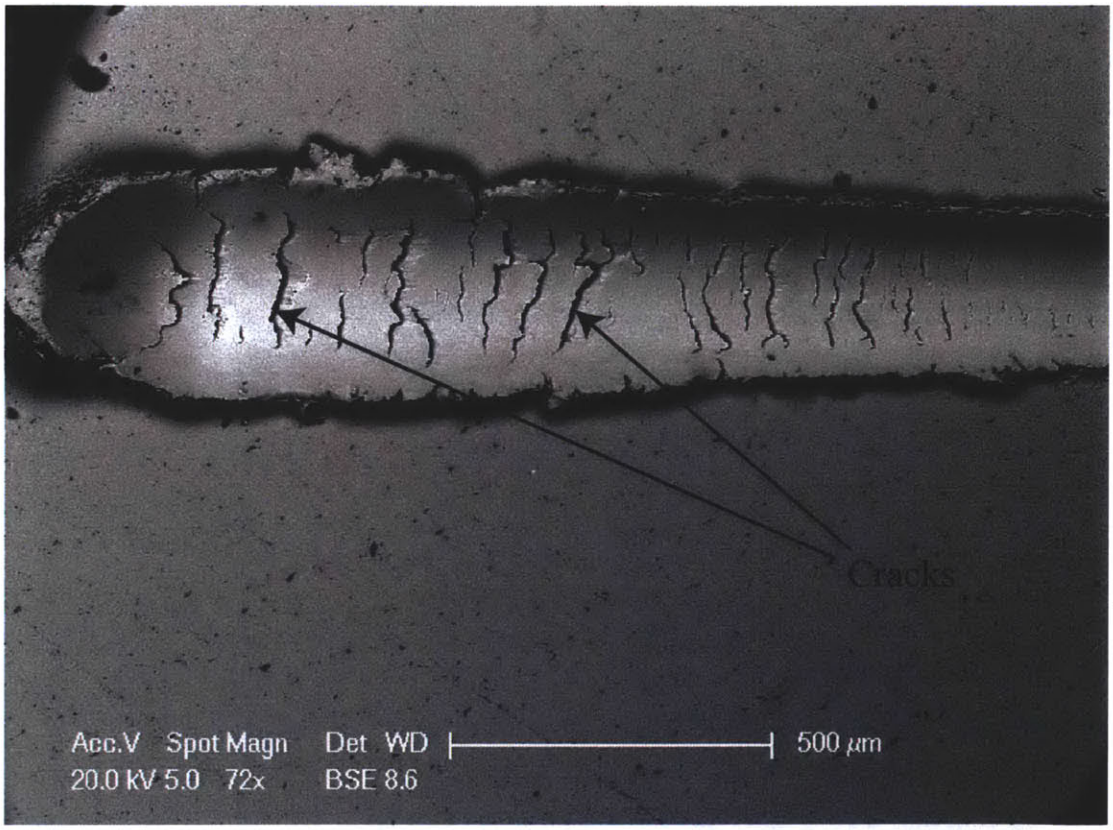

Figure 2-10: Transverse cracks on residual grooves. Scratch tests on cold drawn steel AISI-1144 with a maximal penetration depth of $d_{max} \geq 50\mu$m. The scratch direction is from right to left.

the material, several curved cracks appear and material removal occurs as can be seen in Figure 2-9.

A similar process was observed on cold drawn steel AISI-1144. Figure 2-10 displays a scanning electron image of the residual groove after scratch testing. Steel AISI-1144 was provided by McMaster-Carr (Robbinsville, NJ) as a rod with a diameter of 12 mm. The specimen preparation procedure involved machining with an horizontal metal cutting band saw and a diamond table top saw, coarse dry grinding with alumina oxide paper sanding discs on a rotating lapping table, coarse wet polishing with a 15-μm diamond suspension oil solution and finally dry fine polishing with a polishing cloth on a rotating lapping table. The scratch tests were performed with the CSM Instruments Revetest Scratch Tester at a maximum vertical force of 150 N, resulting in a maximum penetration depth of 50 μm. After scratch testing, environmental scanning electron microscopy was used to image the residual groove. For low penetration depths, the groove is smooth. However as the penetration depth increases, there is an accumulation of curved cracks perpendicular to the scratch direction. The fracture pattern observed here is not through-thickness cracking, which has been reported during the scratch testing of coatings [29, 85]. On the contrary, the cracks are horizontal. Thus, with increasing depth, crack propagation is the dominant mechanism of failure.

2.5 Chapter Summary

The goal of this chapter was to investigate the presence of fracture processes at work during scratch tests. First, Dimensional Analysis was used to investigate the scaling of the force, assuming a brittle fracture-driven material failure mode. It was found that for a perfect cone, and an elasto-plastic material, the horizontal force is proportional to $d^{3/2}$. This scaling was witnessed on scratch tests on polymers with a Vickers probe. The question was then whether this scaling of the horizontal force in $d^{3/2}$ is a sufficient condition for predominant brittle fracture processes.

To this purpose, numerical simulations of scratch tests with a Rockwell probe on metals and polymers were carried out using ABAQUS, assuming a frictionless contact. In both cases, an elasto-plastic behavior led to a force proportional to the square of the penetration depth. However, there was a discrepancy between the force scaling from numerical simulations and the experimental measurements, for which the horizontal scratch force scales as $d^{3/2}$. Therefore, crack propagation is the predominant dissipative process for scratch tests on metals and polymers with a Rockwell C probe and for penetration depths in the conical range.

Furthermore, optical imaging and scanning electron microscopy were chosen to investigate the pattern of physical cracks or surface discontinuities after scratch testing. For both ceramics and metals, as the penetration depth increased, there was an increase of fracture phenomena characterized by material removal, and curved cracks perpendicular to the direction of scratch testing. Moreover, the crack was not vertical, but slightly inclined with respect to the horizontal axis.

Therefore, fracture processes can be assumed to be predominant for scratch tests performed with a 200 μm Rockwell probe and for large depths of penetration. In the next part, based on the experimentally observed fracture pattern, we develop an analytical model that employs Fracture Mechanics to link the forces to the geometry of the probe and to the material elastic and fracture properties.

Part II

Theoretical Analysis

Chapter 3

Linear Elastic Fracture Mechanics Model

In Chapter 2 we have shown that, during scratch tests with a Rockwell C probe, fracture processes becomes predominant as the penetration depth increases. For subsequent theoretical developments, we shall assume that brittle fracture is the main mode of energy dissipation. In this chapter in particular, we express the forces in function of the penetration depth, the scratch probe geometry and the mechanical properties of the material.

In fact, most mechanical models developed in the scientific literature have assumed plowing or plastic flow to be the main model of material failure, as opposed to debris formation. In particular, several models have been proposed to predict the forces involved during the sliding of a rigid indenter over a ductile material [39, 115] based on the slip-line field theory [115] or on numerical simulations [25, 24]. Two quantities are usually introduced: the scratch hardness, H_S, which is the ratio of the horizontal force F_T over the horizontally projected load-bearing contact area A and the friction coefficient, μ which is the ratio of the horizontal force F_T to the applied vertical force F_V. However, there is a lack of consensus and both the scratch hardness H and the friction coefficient μ are not intrinsic as they usually depend on the material behavior (elastic, perfectly plastic, elasto-plastic with work hardening,..) and the probe geometry (spherical, conical, Vickers,

Berkovich, Rockwell, etc) [23, 115]. Another limitation of these models is the necessity to image the surface after scratching in order to measure geometrical quantities such as the residual groove width or depth. This introduces inaccuracy in the measurement, linked to the observer's subjectivity or skills. Therefore there is a need for an alternative quantitative approach to relate the scratch test results to intrinsic material properties.

In this part Linear Fracture Mechanics is used to relate the forces to the material fracture toughness and to the geometry of the test. In particular, Chapter 3 studies linear elastic isotropic materials, whereas Chapter 4 focuses on linear visco-elastic isotropic materials. In both cases, an energy balance of the dissipation processes (fracture, plastic yielding, viscous bulk dissipation,...) is performed. A path-independent contour integral is then used to evaluate the energy release rate. Finally, a threshold criterion is introduced to define the onset of crack propagation.

This chapter is articulated as follows: first, the Airy stress function method is introduced as a powerful tool to solve for the stress and strain fields for plane stress and plane strain problems. Secondly, a brief presentation of the essential concepts of Linear Elastic Fracture Mechanics is given. Thirdly, a fracture model applicable to scratch test is developed by neglecting or taking into account the contribution of the vertical force to the fracture process. Finally, the validity of the analytical model is tested by confronting it with experimental data.

3.1 Airy stress function

This section succinctly introduces the Airy stress function concept; for an exhaustive presentation, the reader is referred to [36]. An *Airy stress function* $\varphi(x, z)$ is a sufficiently smooth scalar function introduced to satisfy the equations of equilibrium of plane

problems when the body forces are negligible:

$$\frac{\partial \sigma_{xx}}{\partial x} + \frac{\partial \sigma_{xz}}{\partial z} = 0 \tag{3.1}$$

$$\frac{\partial \sigma_{xz}}{\partial x} + \frac{\partial \sigma_{zz}}{\partial z} = 0 \tag{3.2}$$

The Airy stress function φ is then defined by (3.3).

$$\sigma_{xx} = \frac{\partial^2 \varphi}{\partial z^2}; \quad \sigma_{xz} = -\frac{\partial^2 \varphi}{\partial x \partial z}; \quad \sigma_{zz} = \frac{\partial^2 \varphi}{\partial x^2}; \tag{3.3}$$

With this definition, it is straightforward to verify that the equilibrium equations (3.1) and (3.2) are automatically satisfied. Moreover, if the material is linear elastic isotropic, the compatibility equation, expressed in terms of stress, reads:

$$\frac{\partial}{\partial x^2}\left(\sigma_{xx} + \sigma_{zz}\right) + \frac{\partial}{\partial z^2}\left(\sigma_{xx} + \sigma_{zz}\right) = 0 \tag{3.4}$$

Therefore, φ is biharmonic, that is:

$$\Delta\Delta\varphi = 0 \tag{3.5}$$

where Δ is the Laplace operator defined in 2-D by:

$$\Delta\varphi(x, z) = \frac{\partial^2 \varphi}{\partial x^2} + \frac{\partial^2 \varphi}{\partial z^2} \tag{3.6}$$

Eq. (3.5) is exact in plane strain conditions and yields a good approximation for thin plates in plane stress conditions [4]. Therefore, solving for a statically compatible stress field boils down to finding an Airy stress function $\varphi(x, z)$ satisfying Eq. (3.5) in a way that verifies the stress boundary conditions.

Moreover, denoting by E and ν respectively the Young's modulus and the Poisson's

ratio, the displacements are related to the Airy stress function by:

$$u_x(x,z) = \frac{1}{E}\left(-(1+\nu)\frac{\partial \phi}{\partial x} + \kappa \frac{\partial V}{\partial z}\right) + U_x \tag{3.7}$$

$$u_z(x,z) = \frac{1}{E}\left(-(1+\nu)\frac{\partial \phi}{\partial z} + \kappa \frac{\partial V}{\partial x}\right) + U_z \tag{3.8}$$

where (U_x, U_z) is a rigid displacement, that does not provoke strains, and $V(x,z)$ is a potential function that satisfies:

$$\Delta V = 0; \quad \frac{\partial^2 V}{\partial x \partial z} = \Delta \varphi \tag{3.9}$$

3.2 Linear Elastic Fracture Mechanics

Linear Elastic Fracture Mechanics describes the behavior of materials to fail, under loading, in a brittle manner that involves the propagation of cracks or surface displacement discontinuities. When a fracture occurs in a quasi-brittle material, the elastic energy stored in the system is released in an almost instantaneous way and is dissipated through the formation of new crack surfaces. Moreover, fracture occurs when the energy provided from the outside reaches a critical energy threshold called the "fracture energy". Fracture mechanics deals with the description of fracture processes. In the next paragraph, we will introduce elements of Fracture Mechanics, restricting ourselves to isothermal and quasi-static variations.

3.2.1 Thermodynamics of Irreversible Processes

Given a material domain Ω of boundary $\partial\Omega$, the energy balance of the system is expressed by the First Law of thermodynamics:

$$d\mathcal{U} = \delta \mathcal{W}_{ext} + \delta Q \tag{3.10}$$

The First Law states that the internal energy variation, $d\mathcal{U}$, is the sum of the energy supplied in form of work, $\delta\mathcal{W}_{ext}$, and heat, δQ. Moreover, the Second Law of thermodynamics yields the entropy balance of the system:

$$\int_{\Omega} \varphi dt d\Omega = d\mathcal{D} = \theta_0 d\mathcal{S} - \delta Q \geq 0 \tag{3.11}$$

where φdt is the dissipation volume density and θ_0 is the reference temperature expressed in the absolute scale. Inequality (3.11) asserts that the entropy variation of the system, dS, must be greater or equal to the entropy supplied in form of heat, $\delta Q/\theta_0$, from the outside of the system. The difference between the first and the second term on the right hand side of Eq. (3.11) is the dissipation of the entire system, $d\mathcal{D}$: it is the amount of useful mechanical energy that is irreversibly transformed into heat form; it has units of Joules ($[d\mathcal{D}] = L^2MT^{-2}$).

We introduce the global free energy of the system, which is its maximum capacity to do work:

$$W = \int_{\Omega} \psi d\Omega = \mathcal{U} - \theta_0 \mathcal{S} \tag{3.12}$$

where ψ is the Helmholtz free energy volume density and $\mathcal{S}$ is the total entropy of the system. A substitution of (3.10) in (3.11) allows us with the help of (3.12) to rewrite the Second Law in terms of the Clausius-Duhem inequality:

$$d\mathcal{D} = \delta\mathcal{W}_{ext} - dW \geq 0 \tag{3.13}$$

In particular, an elastic system is non-dissipative ($d\mathcal{D} = 0$), meaning that the externally supplied work is entirely stored as recoverable energy in the system.

We define the potential energy of the system as the difference between the free energy

and the external work due to prescribed body and surface forces:

$$\mathcal{E}_{pot} = W - \Phi = \int_{\Omega} \psi d\Omega - \left[\int_{\Omega} \rho \underline{f} \cdot \underline{\xi} d\Omega + \int_{\partial\Omega_{\underline{T}^d}} \underline{T}^d \cdot \underline{\xi} d\Omega \right] \tag{3.14}$$

Using the Theorem of Virtual Work, it can be shown that, for a distribution of volume force density, prescribed surface forces and prescribed displacements that is time-invariant, the dissipation is the negative of the variation of the potential energy:

$$d\mathcal{D} = -d\mathcal{E}_{pot} \geq 0 \tag{3.15}$$

3.2.2 Energy Release Rate and Fracture Energy

Consider a crack surface Γ in a linear elastic body. Let $\mathcal{E}_{pot}(\Gamma)$ be the potential energy associated with the fracture surface under prescribed loading conditions. We assume that the prescribed surface forces $\underline{T}^d$ and displacements $\underline{\xi}^d$ are increased until the onset of crack propagation and then held constant. Our goal is to evaluate whether or not the crack will continue to propagate under fixed loading. For this purpose, we express the intrinsic dissipation:

$$d\mathcal{D} = -d\mathcal{E}_{pot}(\Gamma + d\Gamma) = \mathcal{G} d\Gamma \geq 0; \quad \mathcal{G} = -\frac{\partial \mathcal{E}_{pot}(\Gamma)}{\partial \Gamma} \tag{3.16}$$

$\mathcal{G}$ is the amount of potential energy stored in the system which is released when the crack propagates by $d\Gamma$. Eq. (3.16) identifies the energy release rate $\mathcal{G}$ as the global thermodynamic force associated, in the dissipation, with the crack propagation $d\Gamma$.

We use a threshold law to define the onset of crack propagation:

$$f := \mathcal{G} - \mathcal{G}_f \leq 0; \quad d\Gamma \geq 0; \quad (\mathcal{G} - \mathcal{G}_f) d\Gamma = 0 \tag{3.17}$$

Eq. (3.17) is the standard format of evolution laws set up within the framework of thermodynamics of irreversible processes. The crack propagates when the energy release

rate $\mathcal{G}$ reaches a threshold $\mathcal{G}_f$, which is the fracture energy. It is also the amount of potential energy, $\mathcal{E}_{pot}$, dissipated per unit of newly created crack surface.

Eq. (3.17) is a global fracture criterion based on energy balance. Alternatively a local fracture criterion can be written, based on the singular stress field at the crack tip [53]:

$$f := K_I - K_c \leq 0; \quad d\Gamma \geq 0; \quad (K_I - K_c)d\Gamma = 0 \tag{3.18}$$

In (3.18), K_I is the stress intensity factor that depends on the stress/displacement boundary conditions and on the geometry of the system. Meanwhile, K_c is a material property called *fracture toughness* and it is related to the fracture energy, $\mathcal{G}_f$ through the Griffith-Irwin relationship:

$$K_c = \sqrt{E'\mathcal{G}_f} \tag{3.19}$$

where $E' = E$ in plane stress and $E = E/(1-\nu^2)$ in plane strain.

3.2.3 J-Integral

The J-integral is a way of evaluating the energy release rate, $\mathcal{G}$, using a contour integral surrounding the crack tip, that was proposed simultaneously by Rice [89] and Cherepanov [32]. Consider a crack Γ oriented in the direction $\underline{e}_1$ that propagates from length ℓ to $\ell + d\ell$ at a velocity $\dot{\ell}\underline{e}_1$. The objective is to evaluate the energy release rate $\mathcal{G}$ from the variation of the potential energy, $-\partial\mathcal{E}_{pot}/\partial\Gamma$, in a sub-domain Ω' of a material domain Ω enclosing the crack surface (cf. Figure 3-1 a)). As can be seen on Figure 3-1 a), the boundary $\partial\Omega'$ of the material sub-domain Ω' comprises the crack front Γ and the remaining boundary $\mathcal{C}$. Here, the crack surface, Γ, is assumed to be stress-free, and $\mathcal{C}$, is a displacement boundary. Therefore the change of potential energy is equal to the

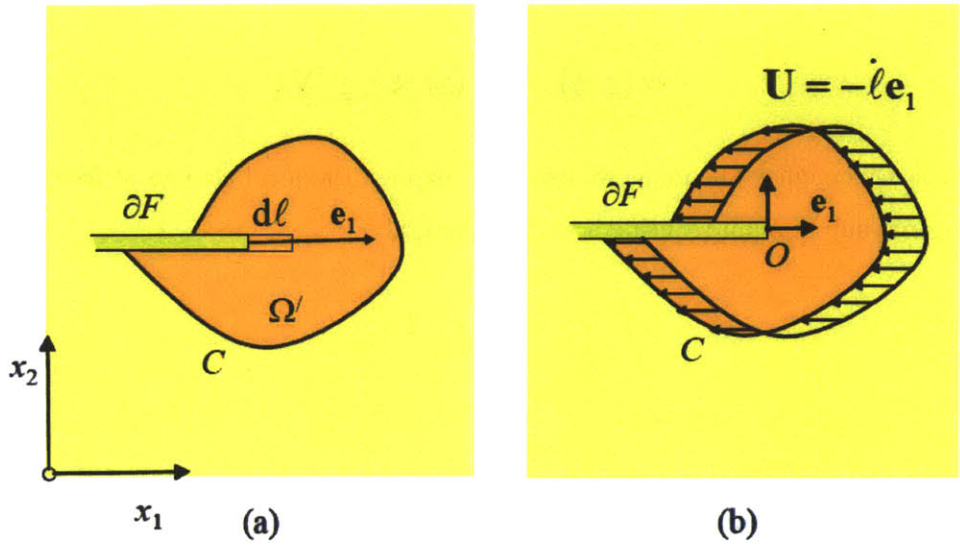

Figure 3-1: Crack propagation from the perspective of a) a fixed observer b) of an observer attached to the tip of the crack . Source [106]

change in the free energy in Ω':

$$\frac{d\mathcal{E}_{pot}}{dt} = \frac{dW}{dt} = \frac{d}{dt}\int_{\Omega'} \psi d\Omega' \tag{3.20}$$

In a moving reference system attached to the crack tip (cf Fig. 3-1 b)), the change in free energy has two contributions: one due to the change of free energy in the material sub-domain Ω', the other due to the energy release that is convectively transported at a speed $\underline{U} \cdot \underline{n} = -\dot{\ell}\,\underline{e}_1$ past the boundary $\partial\Omega'$:

$$\frac{d}{dt}\int_{\Omega'} \psi d\Omega' = \int_{\Omega'} \frac{\partial \psi}{\partial t} d\Omega' + \int_{\partial\Omega'} \psi\,(\underline{U} \cdot \underline{n})\, ds \tag{3.21}$$

For a linear elastic system, the change of free energy is the double product of the stress tensor with the strain rate tensor: $\partial\psi/\partial t = \underline{\underline{\sigma}} : \left(\partial\underline{\underline{\varepsilon}}/\partial t\right) = \underline{\underline{\sigma}} : \left(\underline{\nabla}\partial\underline{\xi}/\partial t\right)$. Moreover, in the absence of body forces, the local momentum balance states that the divergence of

the stress tensor is zero. We then have the equality:

$$\mathtt{div}\left(\underline{\underline{\sigma}}\cdot\underline{\xi}\right)=\mathtt{div}\left(\underline{\underline{\sigma}}\right)\cdot\underline{\xi}+\underline{\underline{\sigma}}:\underline{\nabla}\underline{\xi} \tag{3.22}$$

Using the Divergence Theorem, we can then express the local change of free energy in the material sub-domain Ω' using a surface integral:

$$\int_{\Omega'}\frac{\partial\psi}{\partial t}d\Omega'=\int_{\partial\Omega'}\underline{T}\cdot\frac{\partial\underline{\xi}}{\partial t}ds \tag{3.23}$$

where $\underline{T}=\underline{\underline{\sigma}}\cdot\underline{n}$ is the traction vector on the boundary Ω'. The crack faces are traction-free ($\underline{\underline{\sigma}}\cdot\underline{n}=0$ on F) and oriented along $\underline{e_1}$ ($\underline{U}\cdot\underline{n}=0$ on F), therefore, the right hand side of Eq. (3.21) and the convective term in Eq. (3.23) need only to be evaluated along the boundary $\mathcal{C}$ of Ω'. Assuming that the displacement boundary $\mathcal{C}$ remains fixed during the fracture process, the rate of variation of displacement on $\mathcal{C}$ can then be related to the crack velocity $\dot{\ell}$: $\partial\underline{\xi}/\partial t=\dot{\ell}\,\partial\underline{\xi}/\partial x_1$. We can then rewrite the variation of potential energy as:

$$\frac{d\mathcal{E}_{pot}}{dt}=-\dot{\ell}J;\quad J=\int_{\mathcal{C}}\left[\psi n_1-\underline{T}\cdot\frac{\partial\underline{\xi}}{\partial x_1}\right]ds \tag{3.24}$$

On the other hand, from Eq. (3.16), the variation of potential energy is the negative of the product of the energy release rate $\mathcal{G}$ and the crack velocity $\dot{\ell}$. The energy release rate is thus given by the J-integral:

$$\mathcal{G}=\int_{\mathcal{C}}\left[\psi n_1-\underline{T}\cdot\frac{\partial\underline{\xi}}{\partial x_1}\right]ds \tag{3.25}$$

Case of an oblique crack In the case of an oblique crack propagating in both directions $\underline{e}_1$ and $\underline{e}_2$, two contour integrals are involved; and Eq. (3.15) becomes:

$$\mathcal{G}\dot{\ell}=\dot{\ell}_1\int_{\mathcal{C}}\left[\psi n_1-\underline{T}\cdot\frac{\partial\underline{\xi}}{\partial x_1}\right]ds+\dot{\ell}_2\int_{\mathcal{C}}\left[\psi n_2-\underline{T}\cdot\frac{\partial\underline{\xi}}{\partial x_2}\right]ds \tag{3.26}$$

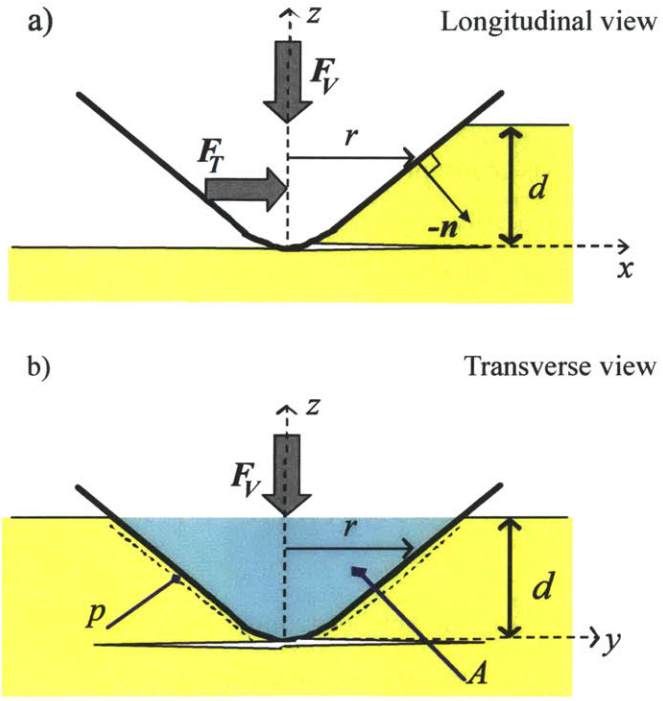

Figure 3-2: Axisymmetric scratch probe geometry. x is the scratch direction due to the application of the scratch force F_T. The scratch probe is maintained at a depth d through the application of a vertical force. a) Longitudinal view. b) Transverse view.

If the crack propagates more rapidly in direction $\underline{e}_1$ than in direction $\underline{e}_2$, then $\dot{\ell}_1 \gg \dot{\ell}_2$. As a consequence, the second term on the right hand side of Eq. (3.26) can be neglected; and the energy release rate can be evaluated using Eq. (3.25). This is the assumption that will be used for the fracture mechanics analysis of scratch tests.

3.3 Linear Elastic Fracture Model for Scratch Tests

In this section we apply the concepts of Linear Elastic Fracture Mechanics presented previously to develop an analytical model in order to derive the expression of the forces during scratch test. Consider thus an axisymmetric scratch probe. The origin of the coordinate system is at the tip of the probe (cf. Fig. 3-2) and the shape of the probe is defined by a single variable monomial function of the form, commonly used to study nano-indentation [70]:

$$z = Br^{\epsilon} \tag{3.27}$$

where B (of dimension $L^{1-\epsilon}$) is the height at unit radius and ϵ is the degree of the homogeneous function. The degree ϵ and the proportionality factor B for common probe shapes considered is given in Table 3.1. Some geometric relations will turn out useful for the following developments. These are the outward unit normal at the scratch probe/material interface, (S):

$$\underline{n} = -\frac{\epsilon B r^{\epsilon-1}\cos\phi}{\sqrt{1+(\epsilon B r^{\epsilon-1})^2}}\underline{e}_r + \frac{1}{\sqrt{1+(\epsilon B r^{\epsilon-1})^2}}\underline{e}_z \tag{3.28}$$

for $r \in [0(d/B)^{1/\epsilon}]$ and $\phi \in [-\pi/2, \pi/2]$; and the differential line element ds and surface element, dS:

$$ds = \sqrt{1+(\epsilon B r^{\epsilon-1})^2}dr \tag{3.29}$$

$$dS = r\, d\phi\, ds \tag{3.30}$$

$$\tag{3.31}$$

Some derived geometric quantities of interest are the contact area projected in the

Probe Type	ϵ	B
Conical	1	$\cot\theta$
Spherical	2	$1/(2R)$
Flat Punch	$\rightarrow +\infty$	$(1/R^{\epsilon-1})$

Table 3.1: Degree ϵ of the homogeneous function and proportionality factor B for several scratch probes

scratch direction $n_x = \underline{n} \cdot \underline{e}_x$:

$$A_{LB}(d) = -\int_{(S)} n_x dS = \frac{2B\epsilon}{\epsilon+1}\left(\frac{d}{B}\right)^{(1/\epsilon)+1} \tag{3.32}$$

and the perimeter of the scratch probe projected onto the scratch direction (Fig. 3-2):

$$p(d) = \int_{(S)} dS = \left(\frac{d}{B}\right)^{1/\epsilon}\beta \tag{3.33}$$

with β a noteworthy dimensionless paramter:

$$\beta = 2\int_0^1 \sqrt{1+(\epsilon d)^2\left(\frac{d}{B}\right)^{-2/\epsilon} x^{2\epsilon-2}}dx \tag{3.34}$$

It was shown in Chapter 2 that the cracks generated during scratch testing are not radial, but lateral. Figure 3-3 in particular displays a section of the residual groove of steel AISI-1045 after scratch testing with a Rockwell C probe and at a maximum vertical force of 150 N. There are two crack fronts perpendicular to the direction of scratch testing (from left to right). Within each crack front, there is the presence of several oblique fracture surfaces. From this figure we can conclude to the presence of several cracking events during a micro-scratch test. In our theoretical model we consider a single cracking event. Moreover, we assume that, the fracture energy, which is the energy required to propagate a unit fracture surface, is intrinsic and independent on external factors such as crack length and crack orientation.

We thus hypothesize the existence of a semi-circular lateral crack of length ℓ emanat-

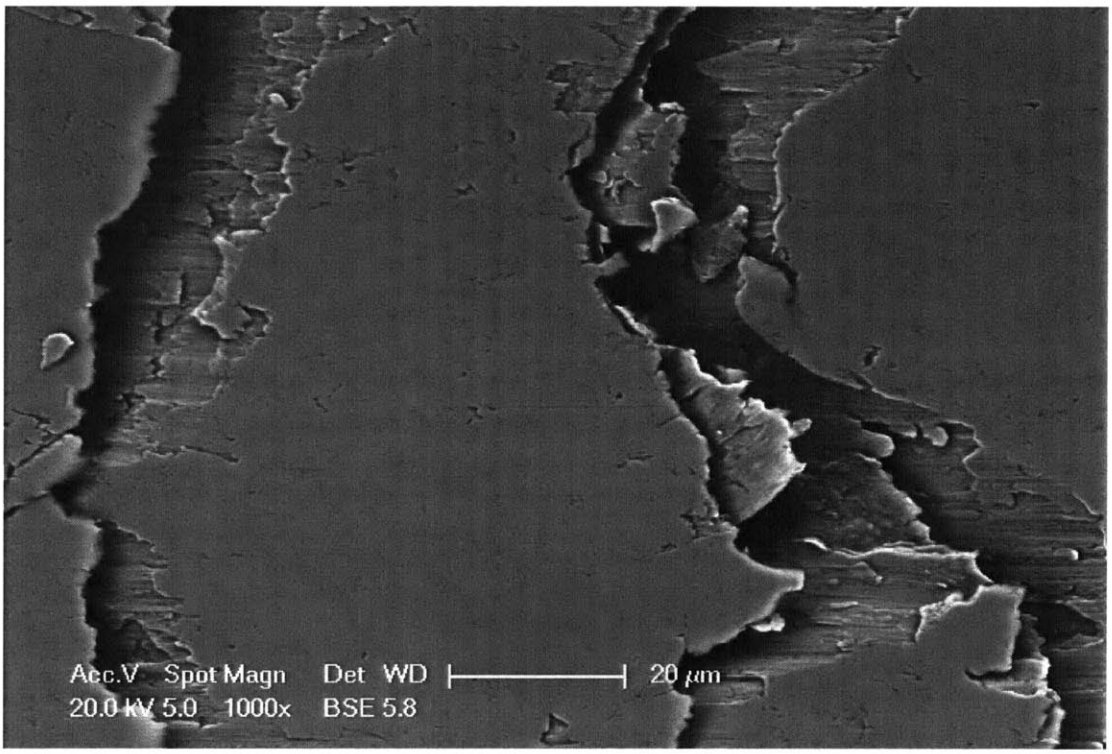

Figure 3-3: Crack pattern during a scratch test on steel AISI-1045 with a Rockwell C probe. The scratch direction is from right to left.

ing from the tip of the scratch probe. The crack is assumed to propagate in the direction $\underline{e}_x$ and the crack area is $\Gamma = p\ell$, with p the perimeter of the probe defined by Eq. (3.33). An extension of the contour integral method presented previously yields the following expression of the energy release rate:

$$\mathcal{G} = \frac{1}{p}\int_A \left[\psi n_1 - \underline{T}\cdot\frac{\partial \underline{\xi}}{\partial x}\right] dA \tag{3.35}$$

Compared to the classical form of the J-integral for planar cracks (Eq. (3.25)), in which the fracture perimeter coincides with the fracture width, $dA = pds$, we have chosen to consider a difference between these lengths, in order to employ the technique for different scratch geometries. For the scratch problem at hand, we choose a closed volume that includes the probe-material interface, the stress-free surface at the top ($n_x = 0$; $\underline{T} = 0$), the stress-free fracture surfaces in prolongation of the scratch probe surface ($n_x = 0$; $\underline{T} = 0$), and closing material surfaces far removed from the surfaces ($\psi = 0$; $\partial\xi/\partial x = 0$); so that the only contribution to the surface integral comes from the probe-material interface S:

$$\mathcal{G} = \frac{1}{p}\int_{(S)} \left[\psi n_1 - \underline{T}\cdot\frac{\partial \underline{\xi}}{\partial x}\right] dS \tag{3.36}$$

Physically speaking, the energy release rate so defined can be associated with the energy stored, prior to chipping, into a material domain in front of the scratch probe.

3.3.1 Uni-axial Stress Field

In a first approach, we consider that the sole stress contributing to energy changes ahead of the scratch device is σ_{xx}, which is related to the applied scratch force by:

$$F_T = \int_{(S)} \sigma_{xx} n_x dS = H_T A_{LB} \tag{3.37}$$

The free energy volume density is $\psi = (1/2)\kappa\sigma_{xx}^2/E$ and the work of the stress vector along $\partial\xi_x/\partial x = \epsilon_{xx}$ is $\sigma_{xx} = \kappa\sigma_{xx}^2 n_x/E$ (E is the Young's modulus and $\kappa = 1$ in plane stress and $\kappa = 1 - \nu^2$ in plane strain; ν= Poisson's ratio). The energy release rate thus obtained is the quadratic stress average over the projected contact area $n_x\, dS = dS_x$:

$$\mathcal{G} = \frac{\kappa}{2pE}\int_{(S)} \sigma_{xx}^2 n_x dS = \frac{\kappa}{2pE}\int_{(A_{LB})} \sigma_{xx}^2 da \tag{3.38}$$

The problem to be solved amounts to combining the linear stress average of the boundary condition Eq.(3.37) with the quadratic stress average of Eq. (3.38). For instance, assuming a constant stress field over the probe surface, we have:

$$\mathcal{G} = \frac{\kappa}{2pA_{LB}E}F_T^2 = \frac{\kappa A_{LB}}{2pE}H_T^2 \tag{3.39}$$

where we note that $A_{LB} = -S_x$ is the nominal projected surface area defined by Eq. (3.32), and p the perimeter defined by Eq. (3.33). Then using these expressions in Eq. (3.39), we obtain the following expression of the energy release rate for any axisymmetric probe:

$$\mathcal{G} = \frac{\kappa}{E}\frac{1+\epsilon}{4\beta}(\epsilon B)^{-1}\left(\frac{B}{d}\right)^{(2/\epsilon)+1} F_T^2 = \frac{\kappa}{E}\frac{B\epsilon}{\beta(\epsilon+1)}\left(\frac{d}{B}\right)H_T^2 \tag{3.40}$$

Finally, when the fracture propagates, the energy release rate equals the fracture energy, $\mathcal{G}_f$, which in turn relates to the fracture toughness by $\mathcal{G}_f = (\kappa/E)K_c^2$. We thus obtain the following criterion for fracture propagation:

$$F_T \leq F_c = 2K_c\left(\frac{d}{B}\right)^{(1/\epsilon)+(1/2)}\left(\frac{\epsilon}{1+\epsilon}\beta B\right)^{(1/2)} \tag{3.41}$$

or in terms of scratch hardness:

$$H_T \leq H_c = \frac{F_c}{A_{LB}} = K_c d^{-1/2}\left(\frac{1+\epsilon}{\epsilon}\beta\right)^{(1/2)} \tag{3.42}$$

The previous relation thus reveals that the scratch force and scratch hardness, upon fracture propagation (i.e. $F_T = F_c$, $H_T = H_c$) scale with the scratch depth according to:

$$\frac{F_c(\lambda d)}{F_c(d)} = \left(\frac{\beta(\lambda d)}{\beta(d)}\right)^{1/2} \lambda^{(1/\epsilon)+(1/2)} \tag{3.43}$$

$$\frac{H_c(\lambda d)}{H_c(d)} = \left(\frac{\beta(\lambda d)}{\beta(d)}\right)^{1/2} \lambda^{-1/2} \tag{3.44}$$

Due to the lack of geometrical self-similarity of the dimensionless perimeter function Eq. (3.34), that is $\beta(\lambda d) \neq \lambda^{\kappa}\beta(d)$, there is no reason that the scratch force or scratch hardness should obey to self-similar transformation rules, except for special yet highly relevant cases; as illustrated later on.

3.3.2 Theory Refinement: Account for Shear Stresses

Arguably, the assumption that the axial stress solely contributes to energy changes may be an oversimplification of the actual stress field that develops ahead of the scratch probe. A refined analysis will, in addition consider (at least) shear stresses at the probe-material interface due to the presence of a vertical force, F_V, that maintains the scratch probe at depth d (Fig. 3-2). The focus of this section is to incorporate this effect. Instead of Eq. (3.38) we thus consider the following force-stress boundary condition:

$$\underline{F} = F_T \underline{e}_x - F_V \underline{e}_Z = \int_{(S)} (\underline{\underline{\sigma}} \cdot \underline{n}) dS \tag{3.45}$$

with

$$F_T = \int_{(S)} (\sigma_{xx} n_x + \sigma_{xz} n_z) dS \tag{3.46}$$

$$-F_V = \int_{(S)} (\sigma_{xz} n_x) dS \tag{3.47}$$

The stresses, σ_{xx} and σ_{xz} are estimated using an Airy stress function approach as presented in Section 3.1. In particular, assuming an Airy stress function of the form:

$$\varphi(x,z) = bx\left(z^3 - \frac{3}{4}zd^2\right) + cz^2 \tag{3.48}$$

We can derive the stress components by using Eq. (3.3).

$$\sigma_{xx} = -6bxz + 2c \tag{3.49}$$

$$\sigma_{xz} = b\left(3z^2 - \frac{3}{4}d^2\right) \tag{3.50}$$

$$\sigma_{zz} = 0 \tag{3.51}$$

where (b, c) are constants that are determined from the force boundary condition Eq. (3.45):

$$b = -\frac{(2\epsilon+1)(3\epsilon+1)}{6\epsilon^2}\left(\frac{B}{d}\right)^{1/\epsilon}\frac{F_V}{d^3} \tag{3.52}$$

$$c = -\frac{(\epsilon+1}{4\epsilon}\left(\frac{B}{d}\right)^{1\epsilon}\frac{F_T}{d} \tag{3.53}$$

To evaluate the displacement field, we introduce the following potential function $V(x,z)$ that satisfies Eqs. (3.9):

$$V = -\frac{b}{2}\left(-\frac{x^4+z^4}{2} + 3\left(xz\right)^2\right) + 2cxz \tag{3.54}$$

where (b, c) are defined by Eqs. (3.52) and (3.53). In particular, the gradient of displacement along the x direction is given by:

$$\frac{\partial u_x}{\partial x} = \frac{1}{E}\left(-(1+\nu)\frac{\partial^2\varphi}{\partial x^2} + \kappa\frac{\partial^2 V}{\partial z \partial x}\right) = \frac{\kappa}{E}\sigma_{xx} \tag{3.55}$$

$$\frac{\partial u_z}{\partial x} = \frac{1}{E}\left(-(1+\nu)\frac{\partial^2\varphi}{\partial z \partial x} + \kappa\frac{\partial^2 V}{\partial x^2}\right) = \frac{1}{E}\left((1+\nu)\sigma_{xz} + \kappa\frac{\partial^2 V}{\partial x^2}\right) \tag{3.56}$$

Replacing the displacement gradient in the expression of the energy release rate given by Eq. (3.36), we obtain:

$$\mathcal{G} = -\frac{\kappa}{Ep}\int_{(S)}\left(\frac{\sigma_{xx}^2}{2}n_x + \sigma_{xz}\left(\sigma_{xx}n_z + \frac{\partial^2 V}{\partial x^2}n_x\right)\right)dS \tag{3.57}$$

After integration - (see Appendix A for details) - we thus obtain an expression of the energy release rate that is similar to (3.40):

$$\mathcal{G} = \frac{\kappa}{E}\frac{1+\epsilon}{4\beta}(\epsilon B)^{-1}\left(\frac{B}{d}\right)^{(2/\epsilon)+1}F_{eq}^2 \leq \mathcal{G}_f = \frac{\kappa}{E}K_c^2 \tag{3.58}$$

where the equivalent force, F_{eq}, accounts for both the scratch force, F_T, and the indentation force, F_V:

$$F_{eq} = \sqrt{F_T^2 + \frac{1}{2}\frac{(4\epsilon^2+\epsilon+1)(2\epsilon+1)(3\epsilon+1)}{\epsilon(\epsilon+1)(4\epsilon+1)(5\epsilon+1)}F_V^2} \tag{3.59}$$

The fracture criterion is of a similar form as Eq. (3.41):

$$F_{eq} \leq F_c = 2K_c\left(\frac{d}{B}\right)^{(1/\epsilon)+(1/2)}\left(\frac{\epsilon}{1+\epsilon}\beta B\right)^{1/2} \tag{3.60}$$

The most important result of the refined analysis is that a consideration of shear stresses at the probe-material interface does not affect the scaling relations, but only the scratch force definition, Eq. (3.59), the weighting function of the vertical force being a function of only the degree of the homogeneous function ϵ.

3.3.3 Application to Common Scratch Probes

To summarize, the forces during scratch test are linked to the fracture toughness and the depth of penetration according to:

$$F_{eq} = K_c\sqrt{2pA_{LB}} \tag{3.61}$$

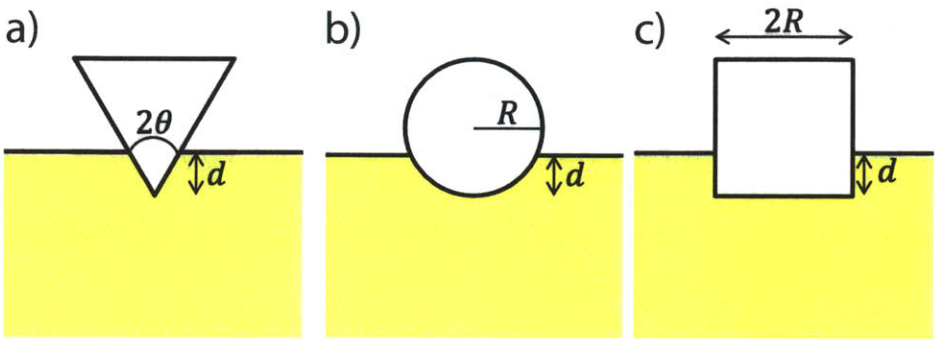

Figure 3-4: Common scratch probe geometries. a) Cone. b) Sphere. c) Flat punch.

Shape	perimeter p	shape function $2pA_{LB}$
Cone	$2d\cos\theta$	$2\frac{\sin\theta}{(\cos\theta)^2}d^3$
Sphere	$2R\cos^{-1}\left(1-\frac{d}{R}\right)$	$\frac{32}{3}Rd^2$
Flat Punch	$2R+d$	$8R^2d$

Table 3.2: Perimeter,p, and shape function, $2pA_{LB}$, of common scratch probe geometries

where F_{eq} is either equal to the horizontal force or given by Eq. (3.59) depending on whether or not we account for the shear stress. Table. 3.2 gives the expression of the scratch probe area function, $2pA_{LB}$ for common scratch probe geometries, cone, sphere and flat punch, as illustrated in Fig. 3-4. In what follows we illustrate the resulting scaling by considering these common scratch probes with the geometrical characteristics defined in Table 3.1.

Conical Scratch Probe

For a conical scratch probe of half apex angle θ (cf Figure 3-4 a)), the degree of the homogeneous function and the height at unit radius are given by respectively: $\epsilon = 1$; $B = \cot\theta$. Applications of Eqs. (3.32)-(3.34) gives:

$$A_{LB} = \frac{1}{\cot\theta}d^2; \quad p = \frac{d}{\cot\theta}\beta; \quad \beta = 2\int_0^1 \sqrt{1+(\cot\theta)^2}ds = \frac{2}{\sin\theta} \tag{3.62}$$

The energy release is given by:

$$\mathcal{G} = \frac{\kappa}{E}\frac{\cos^2\theta}{4\sin\theta}\frac{F_T^2}{d^3} \leq \mathcal{G}_f = \frac{\kappa}{E}K_c^2 \tag{3.63}$$

We then derive the following fracture criteria:

$$F_T \leq F_c = 2K_c d^{3/2}\frac{\sqrt{\sin\theta}}{\cos\theta}; \quad H_T \leq H_c = 2K_c d^{-1/2}\frac{1}{\sqrt{\sin\theta}} \tag{3.64}$$

Thus, due to the invariance of the β-function with respect to the scratch depth d of the conical probe, the scratch force and scratch hardness obey to self-similar scaling relations:

$$F_c(\lambda d) = \lambda^{3/2}F_c(d); \quad H_c(\lambda d) = \lambda^{-1/2}H_c(d) \tag{3.65}$$

with λ a strictly positive real number. Finally, the force-scaling relationship remains valid if one replaces F_T by F_{eq} defined by Eq. (3.59), using $\epsilon = 1$ for a cone:

$$F_{eq} = \sqrt{F_T^2 + \frac{3}{5}F_V^2} \tag{3.66}$$

Last, to put these developments in context, it is interesting to note that the scaling of the fracture force with depth $d^{3/2}$ was derived in Chapter 2 using Dimensional Analysis. Moreover, a similar scaling has been otained in the past from LEFM analysis of the pull-out force of axisymmetric anchors ([10, 58]). Given the difference in load and boundary conditions, and associated stress fields between a pull-out test and the scratch test, this scaling is readily attributed to the particular axisymmetric geometry.

Flat Punch

Consider a flat punch of radius R as illustrated in Figure 3-4 c) . The perimeter of the flat punch is then

$$p = 2R\left(1 + \frac{d}{R}\right) \tag{3.67}$$

Using the monomial function formulation ($\epsilon \to \infty$; $B = R^{1-\epsilon}$) we can derive a lower and an upper bound for the dimensionless perimeter function β. In fact, we have:

$$\frac{\beta}{2} = \lim_{\epsilon \to \infty} \int_0^1 \sqrt{1 + \left(\epsilon d \left(\frac{d}{B}\right)^{-(1/\epsilon)} x^{\epsilon-1}\right)^2}\, dx \tag{3.68}$$

From the triangle inequality applied with the Euclidean norm we have: $\forall y; \quad \sqrt{1+y^2} \leq 1 + ||y||$. We thus obtain:

$$1 \leq \sqrt{1 + \left(\epsilon d \left(\frac{d}{B}\right)^{-(1/\epsilon)} x^{\epsilon-1}\right)^2} \leq 1 + \epsilon d \left(\frac{d}{B}\right)^{-(1/\epsilon)} x^{\epsilon-1} \tag{3.69}$$

It follows:

$$1 \leq \frac{\beta}{2} \leq 1 + \frac{d}{R} \tag{3.70}$$

where the lower bound is relevant for small d/R ratios, whereas the upper bound is relevant for larger depth-to-radius values of the flat punch. As for the projected contact area A_{LB}, it reads:

$$A_{LB} = \lim_{\epsilon \to \infty} \frac{2\epsilon r^{1-\epsilon}}{\epsilon + 1} \left(\frac{d}{R^{1-\epsilon}}\right)^{(1/\epsilon)+1} = 2Rd \tag{3.71}$$

Expression (3.40) thus permits evaluating the energy release rate as:

$$\lim_{\epsilon\to\infty}\mathcal{G}=\frac{\kappa}{E}\frac{1}{8R^2d\left(1+\frac{d}{R}\right)}F_T^2=\frac{\kappa}{2E\left(1+\frac{d}{R}\right)}dH_T^2\leq\mathcal{G}_f=\frac{\kappa}{E}K_c^2 \tag{3.72}$$

The fracture criteria for the flat punch is therefore:

$$F_T\leq F_c=2R\sqrt{2d\left(1+\frac{d}{R}\right)}K_c;\quad H_T\leq H_c=\frac{2K_c}{\sqrt{d}}\sqrt{1+\frac{d}{R}} \tag{3.73}$$

thus, for small depth-to-radius values only, the fracture force and hardness obey to self-similarity:

$$(d/R)\ll 1;F_c(\lambda d)=\lambda^{1/2}F_c(d);H_c(\lambda d)=\lambda^{-1/2}H_c(d) \tag{3.74}$$

It needs to be emphasized that the LEFM solution derived here neglects by design any plastic zone ahead of the sharp corner of the punch, which may well affect the scaling even in a brittle material.

Spherical Scratch Probe

The loss of self-similarity found for the flat punch is even more pronounced for the (hemispherical) scratch probe, which is classically approximated by a parabolic shape, $\epsilon=2$, $B=1/(2R)$, for which:

$$A_{LB}=\frac{2}{3R}(2Rd)^{3/2};\quad p=\sqrt{2Rd}\,\beta \tag{3.75}$$

$$\beta\left(x=\frac{d}{R}\right)=\sqrt{1+2x}+\frac{1}{\sqrt{2x}}\text{arcsinh}\left(\sqrt{2x}\right) \tag{3.76}$$

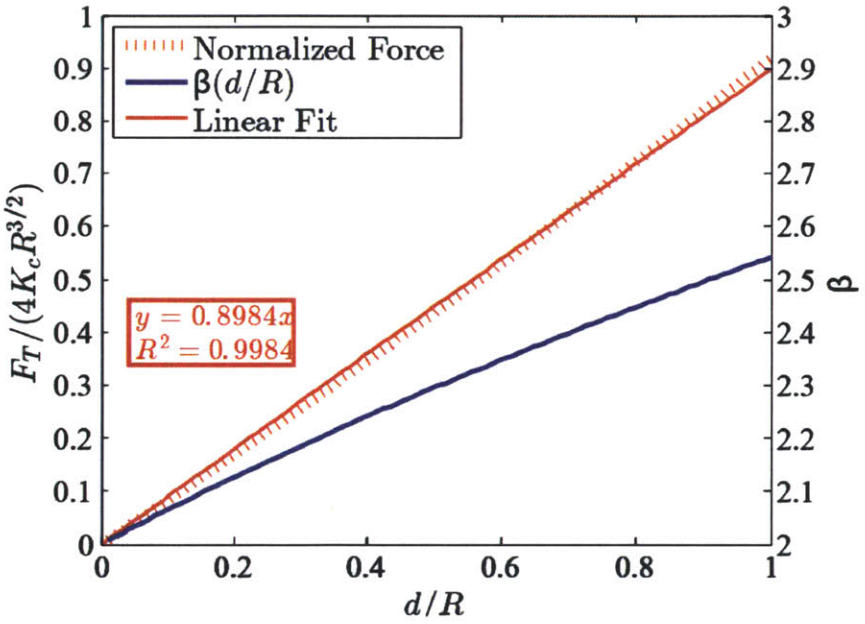

Figure 3-5: Scaling of the normalized fracture force and the perimeter function β, of the spherical scratch probe. The linear fit of the normalized force is almost indistinguishable from the actual curve within $d/R \in [0, 1]$.

The energy release rate is given by:

$$\mathcal{G} = \frac{\kappa}{E}\frac{3}{16\beta}\frac{F_T^2}{Rd^2} \leq \mathcal{G}_f = \frac{\kappa}{E}K_c^2 \tag{3.77}$$

Whence the fracture criteria:

$$F_T \leq F_c = 4K_c d\sqrt{R}\sqrt{\frac{1}{3}\beta\left(\frac{d}{R}\right)} \tag{3.78}$$

$$H_T \leq H_c = \frac{K_c}{\sqrt{d}}\sqrt{\frac{3}{2}\beta\left(\frac{d}{R}\right)} \tag{3.79}$$

Except for small values of $d/R \ll 1$, for which $\beta = 2$, and for which $F_T(\lambda d) = \lambda F_t(d)$ and $H_T(\lambda d) = \lambda^{-1/2}H_T(d)$, there is strictly no self-similar relation for the parabolic scratch probe. On the other hand, for all practical ranges of hemi-spherical scratch probes (that is, $d/R \in [0,1]$), $\beta(d/R)$ varies little between 2 and 2.5425, and does little affect the scaling as evidenced in Fig. 3-5; so that the following self-similar scaling relation can be used in a first, but very good approximation:

$$F_T(\lambda d) \approx \lambda F_t(d); \quad H_T(\lambda d) \approx \lambda^{-1/2}H_T(d) \tag{3.80}$$

Finally, replacing F_T by F_{eq} as defined by (3.59) provides a means to account for shear force transmission over the interface:

$$F_{eq} = \sqrt{F_T^2 + \frac{665}{1188}F_V^2} \tag{3.81}$$

3.4 Chapter Summary

Linear Elastic Fracture Mechanics provides a means to link the forces during a scratch test to the geometry of the scratch probe and to the fracture properties of the scratched materials. In this chapter, we considered only fracture-related dissipative mechanisms and showed that, upon crack propagation in linear elastic isotropic bodies, the equivalent

scratch force, F_{eq}, is proportional to the fracture toughness K_c and to the scratch probe area function, $2pA$; where F_{eq} is related to the horizontal and vertical force.

The scaling of the force is also rationalized. In particular self-similarity applies only for a conical scratch probe; in which case the force scales as $d^{3/2}$, d being the depth of penetration. This scaling is in agreement with results from Dimensional Analysis, as demonstrated in Chapter 2. For other probes, additional length scales are involved and the scaling of the scratch force does not strictly obey self-similarity relation. Nevertheless, an approximation can be made for shallow penetration depths with a spherical probe; in these cases the force scales linearly with the depth of penetration.

In this chapter the only mode of energy dissipation considered was crack propagation; this can be a restrictive assumption especially for rate-dependent materials where viscous dissipation is susceptible to occur. Therefore, the objective of the next chapter is to extend the solution derived here to account for possible rate effects.

Chapter 4

Linear Visco-elastic Fracture Mechanics Model

Rate and time-dependent crack propagation is pervasive in science and engineering. For instance, visco-elastic crack growth can be used to explain stick-slip crack motion [75]. In geotechnical engineering and geology, the gradual failure of dams led to the need to characterize the rate-dependent fracture toughness of concrete [14, 15, 17, 57]. In natural gas distribution, the creep crack growth of polyethylene generated expensive maintenance costs due to the time-dependent failure of plastic pipes [20].

In fact, most materials exhibit some rate-dependence, especially at the microscopic scale. [105, 14, 71]. Thus, the extension of the Linear Elastic Fracture Mechanics model of Chapter 3 to account for rate effects on fracture properties is the focus of this chapter. In particular, herein we neglect any temperature dependence of the mechanical behavior, and investigate the influence of a linear visco-elastic behavior of the scratched material on the scaling of the scratch forces. The first step is to develop a three-dimensional constitutive model under isothermal and quasi-static conditions. Then we present some generic methods to solve boundary value problems involving linear visco-elastic materials. Finally, these methods are applied to relate the forces and the geometry to the fracture and visco-elastic properties in the scratch test.

4.1 Three-Dimensional Constitutive Model for Linear Visco-elastic Materials

4.1.1 Stress-strain Relation

Consider an elementary system in a reference relaxed state $\underline{\underline{\sigma_0}} = \underline{\underline{0}}$. We decompose the stress and strain tensors (relative to the relaxed reference state) into a deviatoric and spherical part [31, 34]:

$$\underline{\underline{\sigma}} = \underline{\underline{\sigma^d}} + \sigma_m \underline{\underline{1}}; \quad \sigma_m = \frac{1}{3}\, \underline{\underline{\sigma}} : \underline{\underline{1}} \tag{4.1}$$

$$\underline{\underline{\varepsilon}} = \underline{\underline{e}} + \frac{1}{3}\epsilon \underline{\underline{1}}; \quad \epsilon = \underline{\underline{\varepsilon}} : \underline{\underline{1}} \tag{4.2}$$

In a linear visco-elastic material, the deviatoric stress (resp. spherical strain) tensor is related to the deviatoric strain (resp. spherical strain) tensor through linear partial differential equations of the form:

$$p_0 \underline{\underline{\sigma^d}}(t) + p_1 \frac{d}{dt}\underline{\underline{\sigma^d}}(t) + p_2 \frac{d^2}{dt^2}\underline{\underline{\sigma^d}}(t) + \cdots = q_0 \underline{\underline{e}}(t) + q_1 \frac{d}{dt}\underline{\underline{e}}(t) + q_2 \frac{d^2}{dt^2}\underline{\underline{e}}(t) + \cdots \tag{4.3}$$

$$m_0 \sigma_m(t) + m_1 \frac{d\sigma_m(t)}{dt} + m_2 \frac{d^2\sigma_m(t)}{dt^2} + \cdots = n_0 \epsilon(t) + n_1 \frac{d\epsilon(t)}{dt} + n_2 \frac{d^2\epsilon(t)}{dt^2} + \cdots \tag{4.4}$$

This can be rewritten in a more compact form using the differential operator $D = d/dt$:

$$P(D)\underline{\underline{\sigma^d}}(t) = Q(D)\underline{\underline{e}}(t) \tag{4.5}$$

$$M(D)\sigma_m(t) = N(D)\epsilon(t) \tag{4.6}$$

where

$$P(D) = \sum_{l=0}^{N} p_k D^k; \quad Q(D) = \sum_{l=0}^{N} q_k D^k \tag{4.7}$$

$$M(D) = \sum_{l=0}^{N} m_k D^k; \quad N(D) = \sum_{l=0}^{N} n_k D^k \tag{4.8}$$

Equations (4.3) and (4.4) admit the following integral form:

$$\underline{\underline{\sigma}}^d(t) = 2\int_{-\infty}^{t} G(t-\tau)\frac{\partial \underline{\underline{e}}(\tau)}{\partial \tau}d\tau; \quad \sigma_m(t) = \int_{-\infty}^{t} K(t-\tau)\frac{\partial \epsilon(\tau)}{\partial \tau}d\tau \tag{4.9}$$

where $G(t)$ and $K(t)$ are respectively the shear and bulk relaxation modulus.

Before proceeding further, we introduce the Laplace transform operator, which is a powerful tool to solve differential equations [92]. The Laplace transform of a function $f(t)$ of the real variable t, is a function of the complex variable s, which is denoted here by $\widehat{F(s)}$ or $\mathcal{L}(f)(s)$, and which is defined by:

$$\mathcal{L}(f)(s) = \widehat{F(s)} = \int_{0^-}^{+\infty} f(t)e^{-st}dt \tag{4.10}$$

In particular, the Laplace transforms of the time -derivative and of the time-integral of $f(t)$ can be expressed in function of $\widehat{F(s)}$ according to:

$$\mathcal{L}\left(\frac{d}{dt}f(t)\right) = s\widehat{F(s)} - f(0); \quad \mathcal{L}\left(\int_0^t f(t)dt\right) = \frac{1}{s}\widehat{F(s)} \tag{4.11}$$

Equation (4.11) enables one to transform a differential equation of the real time domain into an algebraic equation of the complex s-domain. Hence, we will refer to the complex s-domain as the Laplace domain.

4.1.2 Energy Balance

We consider a decomposition of the strain tensor into an elastic part and a viscous part:

$$\underline{\underline{\varepsilon}} = \underline{\underline{\varepsilon^{el}}} + \underline{\underline{\varepsilon^{v}}} \tag{4.12}$$

Similarly, the strain energy involves two contributions: an elastic and a viscous one.

$$\psi = u\left(\underline{\underline{\varepsilon^{v}}}\right) + \psi^{el}\left(\underline{\underline{\varepsilon^{el}}}\right) \tag{4.13}$$

The volume density of elastic strain energy, ψ^{el}, is the amount of energy stored within a unit volume of material that is recovered upon unloading. The energy $u\left(\underline{\underline{\epsilon^{v}}}\right)$ is not recovered due to viscous effects and is often referred to as *frozen* energy [34]. At the microscopic level, this results from residual stresses within the material, similar to hardening effects in plasticity. However, there exists an essential difference between plasticity and visco-elasticity. In the plastic case, the frozen energy value changes only when plastic loading occurs, and thus when the loading evolves. However in visco-elasticity, the frozen energy evolves and is dissipated into heat form until a relaxed equilibrium state is reached.

From the Clausius-Duhem inequality, the volume density of dissipation rate due to viscous processes reads: $\varphi^{v} = \underline{\sigma} : \left(\partial\underline{\varepsilon}/\partial t\right) - \partial\psi/\partial t$. Given that the elastic strain does not generate any energy dissipation, it comes that the stress tensor is the derivative of the elastic strain energy function, ψ, with respect to the elastic strain tensor. Moreover, if we assume the elastic strain energy to be a quadratic function of the elastic strain, a linear relationship between the stress and the elastic strain tensor is obtained:

$$\psi^{el} = \frac{1}{2}\underline{\underline{\varepsilon^{el}}} : \underline{\underline{\underline{\underline{C_0}}}} : \underline{\underline{\varepsilon^{el}}}; \quad \underline{\underline{\sigma}} = \frac{\partial\psi^{el}}{\partial\underline{\underline{\varepsilon^{el}}}} = \underline{\underline{\underline{\underline{C_0}}}} : \underline{\underline{\varepsilon^{el}}} \tag{4.14}$$

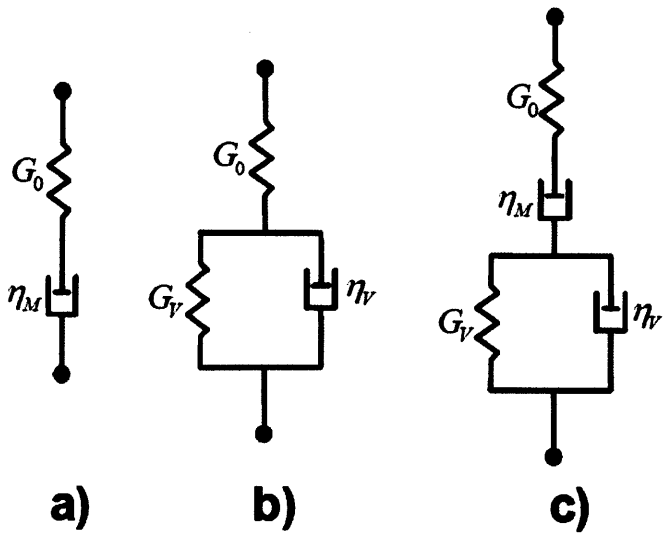

Figure 4-1: Schematic representation of classical linear visco-elasticity mechanical models. a) Three-parameter Maxwell model b) Four-parameter Zener model. c) Five-parameter Burger model. Source [112]

The final expression for the viscous dissipation rate is then:

$$\varphi^v = \left(\underline{\underline{\sigma}} - \frac{\partial u\left(\underline{\underline{\varepsilon}}^v\right)}{\partial \underline{\underline{\varepsilon}}^v} \right) : \frac{\partial \underline{\underline{\varepsilon}}^v}{\partial t} \tag{4.15}$$

In the next section, we will illustrate the constitutive equations (4.12), (4.13) and (4.14) by looking at four particular linear visco-elastic models.

4.2 Classical Linear Visco-elastic Behaviors

Several rheological models have been suggested to model the response of linear visco-elastic materials under diverse loading conditions. These models usually consists of an assembly of linear elastic springs and linear viscous dashpots: the springs store strain

energy whereas the dashpots dissipate mechanical energy into heat form. Herein, we consider a three-parameter Maxwell model, a four-parameter Zener model, a five-parameter Burger model and a generalized Maxwell model. Moreover, for the sake of simplicity, we assume a constant Poisson's ratio: this means that the shear and bulk moduli relaxation functions evolve in similar fashion according to:

$$K(t) = \frac{2}{3}\frac{1+\nu}{1-2\nu}G(t) \tag{4.16}$$

As a consequence, the stress-strain relationships read in the Laplace domain:

$$\widehat{\underline{\underline{\sigma(s)}}} = s\widehat{G(s)}\left[2\widehat{\underline{\underline{e(s)}}} + \frac{2}{3}\frac{1+\nu}{1-2\nu}\widehat{\epsilon(s)}\,\underline{\underline{1}}\right] \tag{4.17}$$

$$\widehat{\underline{\underline{\varepsilon(s)}}} = \frac{1}{s\widehat{G(s)}}\left[\frac{1}{2}\widehat{\underline{\underline{\sigma^d(s)}}} + \frac{1}{2}\frac{1-2\nu}{1+\nu}\widehat{\sigma_m(s)}\,\underline{\underline{1}}\right] \tag{4.18}$$

In particular, the elastic strain is given in the time domain by:

$$\underline{\underline{\varepsilon^{el}(t)}} = \frac{1}{G_0}\left[\frac{1}{2}\underline{\underline{\sigma^d(t)}} + \frac{1}{2}\frac{1-2\nu}{1+\nu}\sigma_m(t)\,\underline{\underline{1}}\right] \tag{4.19}$$

where $G_0 = G(t=0)$ is the initial shear modulus. As for the viscous strain, it is the difference between the total strain and the elastic one:

$$\underline{\underline{\varepsilon^v}}(t) = \underline{\underline{\varepsilon(t)}} - \underline{\underline{\varepsilon^{el}(t)}} \tag{4.20}$$

4.2.1 Maxwell Model

The Maxwell model is the simplest mechanical model for linear visco-elasticity and it consists of a spring and a dashpot in series as illustrated in Figure 4-1. The relaxation shear modulus reads in the Laplace domain:

$$\widehat{G(s)} = \left(\frac{s}{G_0} + \frac{1}{\eta_M}\right)^{-1} \tag{4.21}$$

There is no frozen energy is a Maxwell material, which means that the elastic strain energy is given by:

$$\psi^{el} = \frac{1}{2} G_0 \left[2\, \underline{\underline{e}}^{el}(t) : \underline{\underline{e}}^{el}(t) + \frac{2}{3} \frac{1+\nu}{1-2\nu} \left(\epsilon^{el}(t) \right)^2 \right] \tag{4.22}$$

The viscous dissipation rate associated with the viscous strain is given by:

$$\varphi^{v} = \eta_M \left[2\, \frac{\partial \underline{\underline{e}}^{v}(t)}{\partial t} : \frac{\partial \underline{\underline{e}}^{v}(t)}{\partial t} + \frac{2}{3} \frac{1+\nu}{1-2\nu} \left(\frac{\partial \epsilon^{v}(t)}{\partial t} \right)^2 \right] \tag{4.23}$$

4.2.2 Zener Model

This model is illustrated in Figure 4-1 b) and consists of a spring in series with a Kelvin-Voigt unit (a spring and a dashpot in parallel). The relaxation shear modulus reads in the Laplace domain:

$$\widehat{G(s)} = \left(\frac{s}{G_0} + \frac{s}{G_v + s\eta_v} \right)^{-1} \tag{4.24}$$

While the elastic strain energy is still given by Eq. (4.22), the Zener model has a frozen energy:

$$u\left(\underline{\underline{\varepsilon}}^{v}\right) = \frac{1}{2} G_V \left[2\, \underline{\underline{e}}^{v}(t) : \underline{\underline{e}}^{v}(t) + \frac{2}{3} \frac{1+\nu}{1-2\nu} \left(\epsilon^{v}(t) \right)^2 \right] \tag{4.25}$$

Finally the expression of the viscous dissipation rate is:

$$\varphi^{v} = \eta_V \left[2\, \frac{\partial \underline{\underline{e}}^{v}(t)}{\partial t} : \frac{\partial \underline{\underline{e}}^{v}(t)}{\partial t} + \frac{2}{3} \frac{1+\nu}{1-2\nu} \left(\frac{\partial \epsilon^{v}(t)}{\partial t} \right)^2 \right] \tag{4.26}$$

4.2.3 Burger Model

The Burger Model consists of a Maxwell and a Kelvin-Voigt unit in series, as shown in Figure 4-1 c). The relaxation shear modulus reads in Laplace domain:

$$\widehat{G(s)} = \left(\frac{s}{G_0} + \frac{1}{\eta_M} + \frac{s}{G_v + s\eta_v} \right)^{-1} \tag{4.27}$$

The viscous strain can be decomposed into a contribution from the Maxwell element, $\underline{\underline{\varepsilon^M}}$, and a contribution from the Kelvin-Voigt element, $\underline{\underline{\varepsilon^V}}$. Their Laplace transforms read:

$$\widehat{\underline{\underline{\varepsilon^M(s)}}} = \frac{1}{s\eta_M} \left[\frac{1}{2} \widehat{\underline{\underline{\sigma^d(s)}}} + \frac{1}{2} \frac{1-2\nu}{1+\nu} \widehat{\sigma_m(s)}\, \underline{\underline{1}} \right] \tag{4.28}$$

$$\widehat{\underline{\underline{\varepsilon^V(s)}}} = \frac{1}{G_V + s\eta_V} \left[\frac{1}{2} \widehat{\underline{\underline{\sigma^d(s)}}} + \frac{1}{2} \frac{1-2\nu}{1+\nu} \widehat{\sigma_m(s)}\, \underline{\underline{1}} \right] \tag{4.29}$$

The elastic strain energy is given by Eq. (4.22) and the frozen energy is given by Eq.(4.25). Finally, the viscous dissipation rate has two contributions associated respectively with the viscous Maxwell strain and the viscous Kelvin-Voigt strain:

$$\begin{aligned} \varphi^v = \eta_M & \left[2 \frac{\partial \underline{\underline{e^M(t)}}}{\partial t} : \frac{\partial \underline{\underline{e^M(t)}}}{\partial t} + \frac{2}{3} \frac{1+\nu}{1-2\nu} \left(\frac{\partial \epsilon^M(t)}{\partial t} \right)^2 \right] + \\ \eta_V & \left[2 \frac{\partial \underline{\underline{e^V(t)}}}{\partial t} : \frac{\partial \underline{\underline{e^V(t)}}}{\partial t} + \frac{2}{3} \frac{1+\nu}{1-2\nu} \left(\frac{\partial \epsilon^v(t)}{\partial t} \right)^2 \right] \end{aligned} \tag{4.30}$$

4.2.4 Generalized Maxwell Model

The Generalized Maxwell model consists of n Maxwell units in parallel as illustrated in Figure 4-2. The relaxation shear modulus reads in Laplace domain:

$$\widehat{G(s)} = \left[\frac{G_0}{s} + \sum_{i=1}^{n} \left(\frac{s}{G_i} + \frac{1}{\eta_i} \right)^{-1} \right] \tag{4.31}$$

For each Maxwell unit i, $i = 1 \ldots n$, the strain tensors in the spring, $\underline{\underline{\varepsilon^{el}_i}}$, and in the

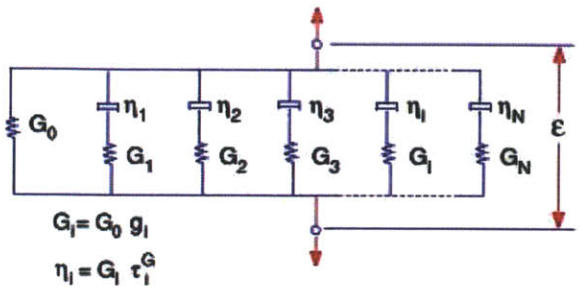

Figure 4-2: Schematic representation of generalized Maxwell model. Source [102]

dashpot, $\underline{\underline{\varepsilon}}^v_i$ are given in Laplace domain by:

$$\widehat{\underline{\underline{\varepsilon}}^{el}_i(s)} = \frac{\frac{s}{G_i}}{\frac{S}{G_i} + \frac{1}{\eta_i}} \widehat{\underline{\underline{\varepsilon}}(s)} \tag{4.32}$$

$$\widehat{\underline{\underline{\varepsilon}}^{v}_i(s)} = \frac{\frac{1}{\eta_i}}{\frac{S}{G_i} + \frac{1}{\eta_i}} \widehat{\underline{\underline{\varepsilon}}(s)} \tag{4.33}$$

The total free energy is then the sum of the contribution from each element:

$$\begin{aligned}\psi =& \frac{1}{2} G_0 \left[2\, \underline{\underline{e}}(t) : \underline{\underline{e}}(t) + \frac{2}{3} \frac{1+\nu}{1-2\nu}\, \epsilon(t) \times \epsilon(t) \right] \\ &+ \sum_{i=1}^{n} \frac{1}{2} G_i \left[2\, \underline{\underline{e}}^{el}_i(t) : \underline{\underline{e}}^{el}_i(t) + \frac{2}{3} \frac{1+\nu}{1-2\nu}\, \epsilon^{el}_i(t) \times \epsilon^{el}_i(t) \right]\end{aligned} \tag{4.34}$$

As for the viscous dissipation rate, it is the sum of the energy dissipation rate in each Maxwell unit:

$$\varphi^v = \sum_{i=1}^{n} \eta_i \left[2\, \frac{\partial \underline{\underline{e}}^v_i(t)}{\partial t} : \frac{\partial \underline{\underline{e}}^v_i(t)}{\partial t} + \frac{2}{3} \frac{1+\nu}{1-2\nu} \left(\frac{\partial \epsilon^v_i(t)}{\partial t} \right)^2 \right] \tag{4.35}$$

4.3 Stress Analysis for Isothermal Quasi-static Boundary Value Problems

In this section we develop methods to solve boundary value problems in linear visco-elastic material under isothermal conditions. First, we introduce the correspondence principle that enables solving boundary value problems by using the solution from the linear elastic case. Then, we develop a thermodynamic framework for the study of crack propagation.

4.3.1 Correspondence Principle

Under the assumption of isothermal, quasi-static evolutions and negligible body forces, the equations of equilibrium for a linear visco-elastic material involve the constitutive equation (4.9) and the momentum balance:

$$\texttt{div}\ \underline{\underline{\sigma}}(t) = 0 \tag{4.36}$$

The compatibility equation reads:

$$\frac{\partial^2 \varepsilon_{ij}}{\partial x_k \partial x_l} + \frac{\partial^2 \varepsilon_{kl}}{\partial x_i \partial x_j} = \frac{\partial^2 \varepsilon_{ik}}{\partial x_j \partial x_l} + \frac{\partial^2 \varepsilon_{jl}}{\partial x_i \partial x_k} \tag{4.37}$$

The traction and displacement boundary conditions read:

$$\underline{\underline{\sigma}}(t) : \underline{n} = \underline{T}^d(t) \quad \texttt{on} \quad \partial\Omega_{\underline{T}^d} \tag{4.38}$$

$$\underline{\xi}(t) = \underline{\xi}^d(t) \quad \texttt{on} \quad \partial\Omega_{\underline{\xi}^d} \tag{4.39}$$

where $\Omega_{\underline{T}^d}$ and $\Omega_{\underline{\xi}^d}$ are complementary portions of the boundary $\partial\Omega$ of the material domain Ω. Finally, the initial conditions of stress-free state must be taken into account:

$$\underline{\xi}(t) = \underline{0}; \quad \underline{\underline{\varepsilon}}(t) = \underline{\underline{\sigma}}(t) = 0 \tag{4.40}$$

It can then be shown [31] that equations (4.36) to (4.40) admit a unique solution provided that the initial values of the shear and bulk relaxation moduli are positive:

$$G(0) > 0 \quad \text{and} \quad K(0) > 0 \tag{4.41}$$

Under these conditions, the elasticvisco-elastic correspondence principle stipulates that, in the Laplace domain, the visco-elastic solution is obtained from the solution of the corresponding elastic problem where the shear and bulk moduli are replaced respectively by $s\widehat{G(s)}$ and $s\widehat{K(s)}$. The time-dependent visco-elastic solution can then be evaluated by performing a subsequent Laplace transform inversion.

The form of the correspondence principle presented above applies strictly only when the displacement and traction boundary conditions are time-invariant. However the correspondence principle can be extended to time-dependent boundary conditions [31] such as crack propagation provided that the loading is monotonically increasing, which is the case in scratch testing.

4.3.2 Thermodynamic Framework for Crack Propagation in Linear Visco-elastic Materials

Consider a steady-state propagation of a crack at a velocity $\dot{\ell}\, \underline{e_x}$. Let Ω' be a sub-domain of the material which encloses the crack surface so that its boundary $\partial\Omega'$ is comprised of the crack face ∂F and of a displacement boundary C. The global dissipation rate in the sub-domain Ω' during crack propagation equals with opposite sign the rate of change of

the potential energy:

$$\frac{d\mathcal{D}}{dt} = -\frac{dE_{pot}}{dt} \geq 0 \tag{4.42}$$

On the other hand, the change in potential energy is given by:

$$\frac{dE_{pot}}{dt} = \frac{d}{dt}\int_{\Omega'} \psi d\Omega' = \int_{\Omega'} \frac{\partial \psi}{\partial t} d\Omega' + \int_{\partial\Omega'} \psi \left(\underline{U} \cdot \underline{n}\right) dS \tag{4.43}$$

Using the Clausius-Duhem inequality along with Eq. (4.15), Eq. (4.43) can be developed as follows:

$$\frac{dE_{pot}}{dt} = \int_{\Omega'} \underline{\underline{\sigma}} : \underline{\underline{\dot{\varepsilon}}} d\Omega' + \int_{\partial\Omega'} \psi \left(\underline{U} \cdot \underline{n}\right) dS - \int_{\Omega'} \left(\underline{\underline{\sigma}} - \frac{\partial \mathcal{U}\left(\underline{\underline{\varepsilon^v}}\right)}{\partial \underline{\underline{\varepsilon^v}}}\right) : \underline{\underline{\dot{\varepsilon}^v}} d\Omega' \tag{4.44}$$

Finally, by using the Theorem of virtual work, we have the following expression of the global dissipation rate:

$$\frac{d\mathcal{D}}{dt} = \dot{\ell} \int_C \left[\psi n_1 - \underline{T} \cdot \frac{\partial \underline{\xi}}{\partial x_1}\right] dS + \int_{\Omega'} \left(\underline{\underline{\sigma}} - \frac{\partial \mathcal{U}\left(\underline{\underline{\varepsilon^v}}\right)}{\partial \underline{\underline{\varepsilon^v}}}\right) : \underline{\underline{\dot{\varepsilon}^v}} d\Omega' \tag{4.45}$$

The second integral on the right hand side of Eq. (4.45) is the viscous dissipation taking place in the bulk of the material. The first term is the fracture dissipation and the thermodynamic force is the energy release rate, $\mathcal{G}$, which is still given by a contour integral:

$$\mathcal{G} = \int_C \left[\psi n_1 - \underline{T} \cdot \frac{\partial \underline{\xi}}{\partial x_1}\right] dS \tag{4.46}$$

4.4 Linear Visco-Elastic Fracture Scratch Model

Consider then the scratch testing of a visco-elastic material as illustrated in Figure 4-3. We are looking for stress and strain fields that satisfy the linear visco-elastic constitutive

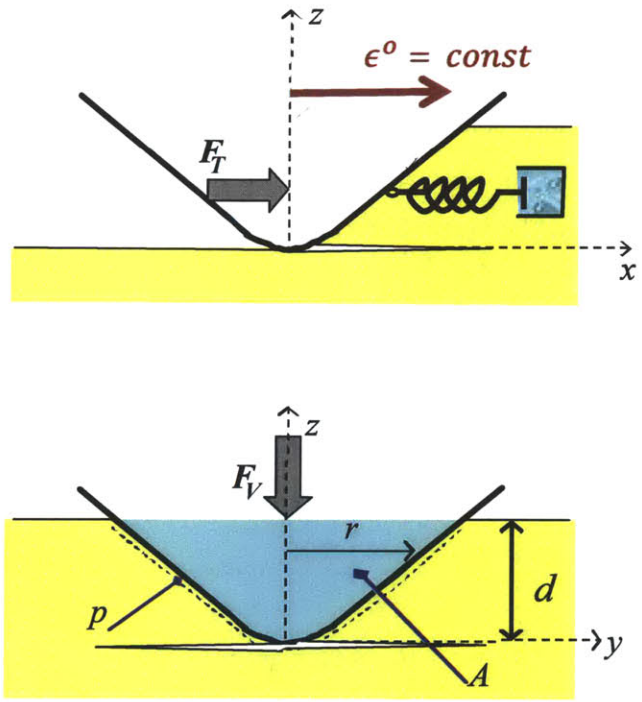

Figure 4-3: Scratch test on a visco-elastic material. Top) Side view. Bottom) Front view.

law (4.9), the momentum balance (4.36), initial conditions (4.40) as well as the traction boundary conditions relevant in our problem. With the origin of the coordinate system being at height $d/2$, the traction boundary conditions include:

- Stress-free boundary conditions on the crack face and on the top:

$$\sigma_{zz}(r, \theta, \pm d/2, t) = 0 \tag{4.47}$$

- The traction boundary conditions at the interface (S) between the scratch probe and the material: where we neglect the contribution to the crack propagation of shear stresses due to the vertical force :

$$\int_{(S)} \sigma_{xx}(r, \theta, z, t) n_x dS = F_T(t) \tag{4.48}$$

For the sake of simplicity, we assume a constant Poisson's ratio. Moreover,the axial strain rate is assumed to be constant $\varepsilon_{xx} = \dot{\epsilon}^0 t$ and the following shape of the strain tensor is considered:

$$\underline{\underline{\varepsilon}}(t) = \dot{\epsilon}^0 t \left[\underline{e}_x \otimes \underline{e}_x - \frac{\nu}{1-\nu} \underline{e}_z \otimes \underline{e}_z \right] \tag{4.49}$$

The resulting stress tensor reads in the Laplace domain:

$$\widehat{\underline{\underline{\sigma}}(s)} = 2s\widehat{G(s)} \frac{\dot{\epsilon}_0}{s^2} \left[\frac{1}{1-\nu} \underline{e}_x \otimes \underline{e}_x + \frac{\nu}{1-\nu} \underline{e}_y \otimes \underline{e}_y \right] \tag{4.50}$$

In particular, the stress field satisfies the traction boundary condition (4.47). We introduce the plane strain relaxation modulus:

$$s\widehat{M(s)} = 4s\widehat{G(s)} \frac{3s\widehat{K(s)} + s\widehat{G(s)}}{s\widehat{K(s)} + 4s\widehat{G(s)}} = \frac{2}{1-\nu} s\widehat{G(s)} \tag{4.51}$$

Then, the axial stress is related to the axial strain via $\widehat{\sigma_{xx}(s)} = s\widehat{M(s)}\widehat{\varepsilon_{xx}(s)}$. As a consequence, we introduce the plane strain visco-elastic coefficient defined by:

$$\lambda(t) = \frac{1}{Mt}\mathcal{L}^{-1}\left(\frac{s\widehat{M(s)}}{s^2}\right) \tag{4.52}$$

where $\mathcal{L}^{-1}(.)$ stands for the inverse Laplace transform, and $M = 4G(3K+G)/(3K+4G)$ is the instantaneous plane strain modulus. The axial stress is then related to the axial strain via:

$$\sigma_{xx} = \lambda(t)M\varepsilon_{xx}(t) \tag{4.53}$$

Furthermore, the elastic strain energy is given by $\psi^{el} = 1/2\sigma_{xx}^2/M$ [1]. We introduce the frozen energy correction factor defined as the ratio of the frozen strain energy to the elastic strain energy :

$$\chi = \frac{\mathcal{U}\left(\underline{\underline{\varepsilon}}^v\right)}{\frac{1}{2}\frac{\sigma_{xx}^2}{M}} \tag{4.54}$$

Using Eq. (4.46) to evaluate the energy release, we then find:

$$\mathcal{G} = \frac{1}{M}\frac{F_T^2}{2pA_{LB}}\left[\frac{2}{\lambda(t)} - 1 - \chi(t)\right] \tag{4.55}$$

The fracture criterion then reads:

$$\frac{F_T}{\sqrt{2pA_{LB}}} \leq \sqrt{MG_c}\,\mathcal{H}(t) \tag{4.56}$$

[1] It can be shown that this expression of the elastic free energy is valid provided that the Poisson's ratio is constant.

where $\mathcal{H}(t)$ is given by:

$$\mathcal{H}(t) = \left[\frac{2}{\lambda(t)} - 1 - \chi(t)\right]^{-\frac{1}{2}} \tag{4.57}$$

$K_c = \sqrt{MG_c}$ is the intrinsic fracture toughness of the material. In summary, in the linear visco-elastic case there is a an apparent fracture toughness due to the coupling between the fracture and the visco-elastic constants as well as the presence of frozen energy in the bulk of the material. In what follows, we will specify the expressions of the plane strain visco-elastic coefficient $\lambda(t)$ and of the frozen energy correction factor $\chi(t)$ for the visco-elastic models presented above.

4.5 Application to Some Visco-elastic Models

4.5.1 Maxwell Model

There is no frozen energy associated with a Maxwell material. Therefore the frozen energy correction factor is zero, while the plane strain visco-elastic coefficient is given by:

$$\chi(t) = 0; \quad \lambda(t) = \frac{1 - e^{-\frac{G_0}{\eta_M}t}}{\frac{G_0}{\eta_M}t} \tag{4.58}$$

In particular, the total strain tensor can be decomposed into its elastic and viscous components:

$$\underline{\underline{\varepsilon}} = \varepsilon_{xx}(t)\left[\underline{e}_x \otimes \underline{e}_x - \frac{\nu}{1-\nu}\underline{e}_z \otimes \underline{e}_z\right] \tag{4.59}$$

$$\underline{\underline{\varepsilon^v}} = [1 - \lambda(t)]\,\varepsilon_{xx}(t)\left[\underline{e}_x \otimes \underline{e}_x - \frac{\nu}{1-\nu}\underline{e}_z \otimes \underline{e}_z\right] \tag{4.60}$$

Because there is no frozen energy, the volume density of work provided to the system is either dissipated in the bulk of the material or stored as elastic strain energy. This elastic strain energy is later released to propagate the crack: $W = \int_0^t \underline{\underline{\sigma}} : \dot{\underline{\underline{\varepsilon}}}\, dt = \int_0^t \varphi^v\, dt + \psi^{el}$.

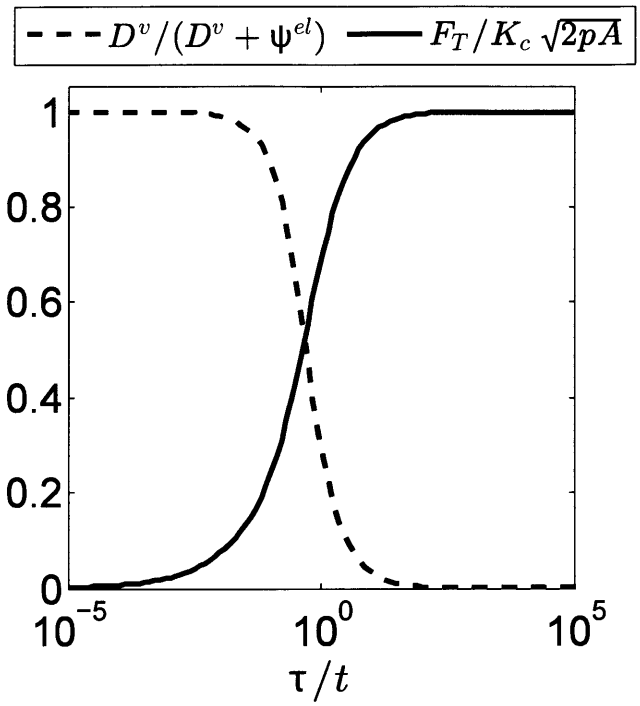

Figure 4-4: Energy balance in a Maxwell material during a scratch test.

Both the viscous dissipation rate and the elastic strain energy can be evaluated from Eqs. (4.19) and (4.23); that is,

$$\int_0^t \varphi^v \, dt = \int_0^t \frac{2}{1-\nu}\eta_M \left[\frac{d}{dt}\left(\varepsilon_{xx} - \lambda\,\varepsilon_{xx}\right)\right]^2 dt = \frac{2}{1-\nu}\frac{\eta_M^2}{G_0}\dot{\epsilon}_0^2 \left[x + 2x\frac{e^{-x}-1}{x} - x\frac{e^{-2x}-1}{2x}\right] \tag{4.61}$$

$$\psi^{el} = \frac{1}{1-\nu}G_0\left[\lambda\varepsilon_{xx}\right]^2 = \frac{1}{1-\nu}\frac{\eta_M^2}{G_0}\dot{\epsilon}_0^2 \left[x^2\frac{1-2e^{-x}+e^{-2x}}{x^2}\right] \tag{4.62}$$

where $x = t/\tau$ and $\tau = \eta_M/G_0$ is the characteristic relaxation time of the material.

Figure 4-4 plots the ratio of the viscous dissipation, $\mathcal{D}^v = \int_0^t \varphi^v$ to the total work, $W = \mathcal{D}^v + \psi^{el}$, as well as the ratio of the apparent to the intrinsic fracture toughness,

$F_T/(K_c\sqrt{2pA_{LB}})$. The x-axis displays the ratio of the characteristic time τ to the crack propagation time t. When the crack propagation time is very small compared to the characteristic time, the behavior is essentially elastic with a negligible viscous dissipation. As a result, the apparent fracture toughness accurately reflects the intrinsic fracture toughness. However, for long periods over which the loading is applied, viscous dissipation becomes predominant and the apparent fracture toughness, $F_T/\sqrt{2pA_{LB}}$, is very small compared to the intrinsic fracture toughness, K_c.

4.5.2 Zener Model

By combining Eqs. (4.24) and (4.52) we get the following expression of the plane strain visco-elastic coefficient for the Zener model:

$$\lambda(t) = \frac{G_V}{G_0 + G_V} + \frac{G_0}{G_0 + G_V} \frac{1 - e^{-\frac{G_0+G_V}{\eta_V}t}}{\frac{G_0+G_V}{\eta_V}t} \tag{4.63}$$

The viscous strain tensor is still given by Eq. (4.60). Using Eq.(4.25) to calculate the frozen energy, we find the following expression for the frozen energy correction factor:

$$\chi(t) = \frac{G_V}{G_0}\left[\frac{1}{\lambda(t)} - 1\right]^2 \tag{4.64}$$

4.5.3 Burger Model

The plane strain visco-elastic coefficient is calculated from equations (4.27) and (4.52). The elastic strain is still given by: $\underline{\underline{\varepsilon}}^{el} = \lambda(t)\varepsilon_{xx}\left[\underline{e}_x \otimes \underline{e}_x - \nu/(1-\nu)\underline{e}_z \otimes \underline{e}_z\right]$ and the viscous strain can be decomposed into a contribution from the Maxwell unit and a contribution from the Kelvin Voigt unit according to:

$$\underline{\underline{\varepsilon}}^M = \frac{1}{\eta_M}\int_0^t \underline{\underline{\sigma}}(\tau)d\tau = \frac{Mt}{\eta_M}\int_0^1 \lambda(ut)u^2 du\ \underline{\underline{\varepsilon}} \tag{4.65}$$

$$\underline{\underline{\varepsilon}}^V = \underline{\underline{\varepsilon}} - \underline{\underline{\varepsilon}}^{el} - \underline{\underline{\varepsilon}}^M = \left(1 - \lambda(t) - \frac{Mt}{\eta_M}\int_0^1 \lambda(ut)u^2 du\right)\ \underline{\underline{\varepsilon}} \tag{4.66}$$

We thus derive the frozen energy correction factor in the form:

$$\chi(t) = \frac{G_V}{G_0}\left[\frac{1}{\lambda(t)} - 1 - \frac{Mt}{\eta_M}\int_0^1 \frac{\lambda(ut)}{\lambda(t)}u^2 du\right]^2 \tag{4.67}$$

4.5.4 Generalized Maxwell Model

For a generalized Maxwell model, the elastic strain in each Maxwell unit is given by:

$$\underline{\underline{\varepsilon_i}} = \lambda_i(t)\underline{\underline{\varepsilon}} \tag{4.68}$$

where the functions λ_i are given by:

$$\lambda_0 = 1; \quad \lambda_i = \frac{1 - e^{-\frac{G_i}{\eta_i}t}}{\frac{G_i}{\eta_i}t}, \quad i = 1 \ldots n \tag{4.69}$$

The plane strain visco-elastic coefficient is given by a weighted average of function λ_i:

$$\lambda(t) = \sum_{i=0}^{n} \frac{G_i}{\sum_{i=0}^{n} G_i}\lambda_i(t) \tag{4.70}$$

Moreover, the total free energy is the sum of the contribution from each Maxwell unit. Using $M = 2/(1-\nu)\sum_{i=0}^{n} G_i$ we obtain the following expression of the frozen energy correction factor:

$$\chi(t) = \sum_{i=0}^{n} \frac{G_i}{\sum_{i=0}^{n} G_i}\left[\frac{\lambda_i(t)}{\lambda(t)}\right]^2 - 1 \tag{4.71}$$

4.6 Chapter Summary

The goal of this chapter was to relate the force measurement to the intrinsic fracture toughness considering a linear visco-elastic behavior of the scratched material. To this end, we introduced the correspondence principle, which enables to extract the linear

Rheological behavior	plane strain visco-elastic coefficient $\lambda(t)$	frozen energy correction factor $\chi(t)$
Maxwell	$\frac{1-e^{-\frac{G_0}{\eta_M}t}}{\frac{G_0}{\eta_M}t}$	0
Four Parameter	$\frac{G_V}{G_0+G_V} + \frac{G_0}{G_0+G_V}\frac{1-e^{-\frac{G_0+G_V}{\eta_V}t}}{\frac{G_0+G_V}{\eta_V}t}$	$\frac{G_V}{G_0}\left[\frac{1}{\lambda(t)}-1\right]^2$
Burger		$\frac{G_V}{G_0}\left[\frac{1}{\lambda(t)}-1-\frac{Mt}{\eta_M}\int_0^1\frac{\lambda(ut)}{\lambda(t)}u^2du\right]^2$
Generalized Maxwell	$\sum_{i=0}^n \frac{G_i}{\sum_{i=0}^n G_i}\lambda_i(t)$	$1-\sum_{i=0}^n \frac{G_i}{\sum_{i=0}^n G_i}\left[\frac{\lambda_i(t)}{\lambda(t)}\right]^2$

Table 4.1: Analytical expressions of the plane strain visco-elastic coefficient $\lambda(t)$ and of the frozen energy correction factor $\chi(t)$ for the linear visco-elastic models detailed in Section **??**

visco-elastic solution from the linear elastic solution. Using this principle, we proposed a framework to study crack propagation in linear visco-elastic materials. Using an energy approach based on the thermodynamics of irreversible processes we showed that the energy release rate remains the driving force for crack propagation, and that it can still be evaluated via a contour integral. These developments were illustrated for some common linear visco-elastic materials. Upon crack propagation the apparent fracture toughness had the generic form:

$$\frac{F_T}{\sqrt{2pA_{LB}}} = K_c\left[\frac{2}{\lambda(t)}-\chi(t)\right]^{-\frac{1}{2}} \tag{4.72}$$

where λ and χ are respectively the plane strain visco-elastic coefficient, and the frozen energy correction factor, given by Eqs. (4.52) and (4.54), respectively. Table 4.1 summarizes the expression of λ and χ for some classical linear visco-elastic behaviors.

Moreover, the ratio of the apparent to the intrinsic fracture toughness reflects the contribution of the respective dissipative mechanisms to the overall dissipation. In fact, the work rate is either dissipated via viscous processes or stored as an elastic or frozen strain energy that is later released to create new fracture surfaces. The ratio of the characteristic time to the crack propagation time, τ/t is crucial: for small values of this ratio, the viscous dissipation is negligible: the material behavior is essentially elastic and the

apparent fracture toughness, $F_T/\sqrt{2pA_{LB}}$, provides an accurate measure of the intrinsic fracture toughness, K_c. However, for large values of this ratio, the viscous dissipation is predominant compared to the fracture dissipation, and the apparent fracture toughness is very negligible compared to the intrinsic fracture toughness. For intermediate values, the knowledge of the visco-elastic properties is essential to decouple creep from fracture.

The model presented rests on several limiting assumptions: quasi-static isothermal evolution, constant Poisson's ratio,uni-axial stress field in front of the probe and fracture behavior influenced only by the horizontal scratch force. The hypothesis of a time-independent Poisson's ratio assumes a similar relaxation behavior for both the shear and bulk modulus. In practice, however, the shear modulus relaxes faster than the bulk modulus. Therefore this assumption is valid for extreme time ranges only ($t \ll \tau$ or $t \gg \tau$). Finally a quasi-static and isothermal evolution neglects any local temperature rise at the crack tip. On the other hand, despite these limitations, we now have a model in hand, that can be used for calibration and validation, as shown in the next part of this thesis.

Part III

Calibration and Experimental Validation

Chapter 5

Scratch Probe Calibration

In Part II, analytical models were developed to express the forces in function of the probe geometry, the testing conditions- penetration depth, scratch speed, loading rate- and the material mechanical properties, assuming predominant brittle fracture processes during the scratch test. In particular, fracture properties can be measured by pulling an axisymmetric probe across the surface of a material as pictured in Figure 5-1. The fracture toughness, K_c, is calculated from:

$$\frac{F_T}{\sqrt{2pA_{LB}}} \leq K_c \tag{5.1}$$

where F_T is the horizontal force, p is the probe perimeter, A_{LB} the projected horizontal load bearing contact area and $2pA_{LB}$ is the scratch probe shape function.

The third part of this thesis is devoted to the calibration and validation of these analytical models. For any axisymmetric probe, it is imperative to calibrate the shape function with a material of known fracture toughness. Specifically, the goal of this chapter is to develop a calibration procedure suited for scratch tests with a 200 μm Rockwell diamond probe. Based on calibration, we then an develop inverse method in order to predict fracture properties using scratch tests. Chapter 6 validates the method for fracture determination on metals, polymers and ceramics. Finally, Chapter 7 builds a method

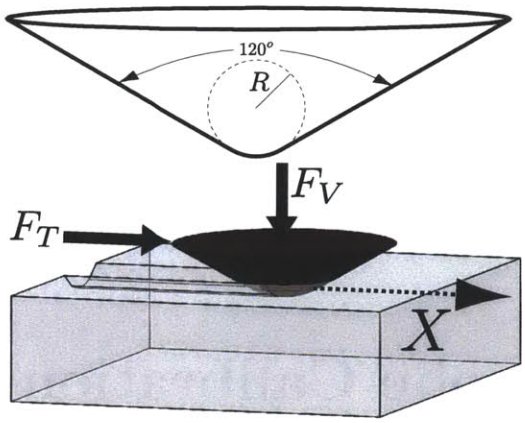

Figure 5-1: Schematic representation of a microscratch test.

to characterize the intrinsic fracture resistance for rate-dependent materials at both the microscopic and the macroscopic level.

In this chapter, we build a protocol to calibrate the shape function of a Rockwell C probe in the spherical range ($d \leq 10$ μm) and in the conical range ($d > 26$ μm). First we identify relevant reference material and develop a specimen preparation procedure. Finally we show that the measured shape function depends solely on the scratch probe geometry and not on extrinsic parameters such as surface cleanliness, probe tip wear, chosen reference material and scratched material.

5.1 Reference Material

The ideal reference material is homogeneous, isotropic, linear elastic, quasi-brittle, easily available and with a known fracture toughness. In this work, we choose two reference materials corresponding to the range of penetration depths. For the spherical range, ($d \leq 10$ μm), we choose 99.995 % silicon dioxide also known as fused silica. For the conical range, ($d > 26$ μm), we choose Lexan 9034. Lexan 9034 is an amorphous polycarbonate that has a known fracture toughness of 2.69 MPa$\sqrt{\text{m}}$ [49], and can be easily provided

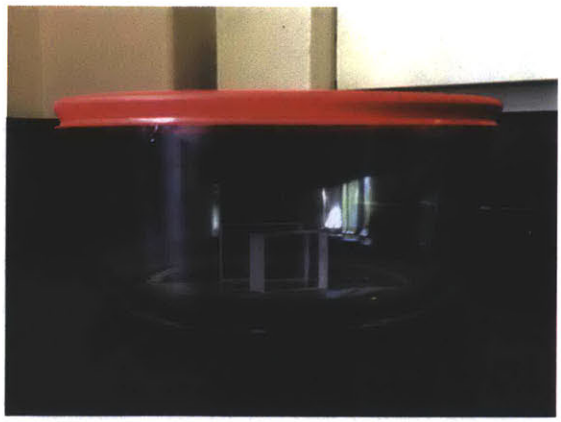

Figure 5-2: Storage of Lexan 9034 specimen in a glass jar with a tight lid.

for as 1/2-inch thick sheets by SABIC Innovative Plastics. As for fused silica, it can be purchased from Mcmaster Carr (Robbinsville, NJ) and has a fracture toughness of 0.58 MPa$\sqrt{\text{m}}$ [46]. It is important to cleanse and dry the calibration specimens prior to testing. For instance, surface impurities or moisture content are known to degrade the mechanical performance of polycarbonate [55, 69].

5.1.1 Material Preparation Procedure

The material preparation procedure described below applies to both Lexan 9034 and fused silica. 25 mm$\times$ 25 mm $\times$ 12 mm Lexan 9034 specimens are cut from 12-mm thick sheets using a saw stop table and the protective plastic film is removed, meanwhile fused silica specimens are cylindrical with a diameter of 25 mm and a height of 12 mm, and they are purchased from McMaster-Carr (Robbinsville, NJ). Forty-eight hours prior to scratch testing, the calibration specimens are washed by ultrasonication for five minutes consecutively in a 1% Alconox solution and then in distilled water. Next, the samples are rinsed by exposing the surfaces to be tested to a jet of running water. After cleansing, the samples are laid in open glass jars and dried in an oven at 250 F for twenty-four hours. Finally, the samples were allowed to cool in closed glass jars with tight lids at

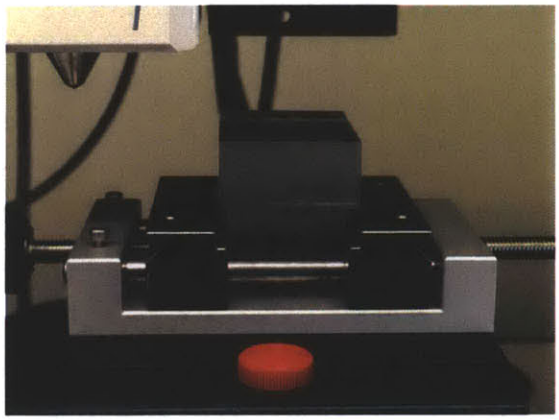

Figure 5-3: Block of Lexan 9034 mounted on a steel plate and held with a CSM Instruments rectangular sample holder prior to scratch testing.

Scratch length (mm)	Scratch speed (mm/min)	Loading rate (N/min)	Maximum vertical force (N)
3	6	60	30

Table 5.1: Testing parameters for the scratch probe calibration.

room temperature as depicted in Figure 5-2.

5.1.2 Rockwell Diamond C Probe

The scratch probe most commonly used is a Rockwell C diamond probe: a cone of half apex angle 60° that ends in a half-sphere of radius R=200 μm. Figure 5-4 a) shows an intact probe whereas Figure 5-4-b) shows a broken one; both optical images were taken with the Micro Scratch Tester optical microscope at the magnification level of 800X. A broken probe can alter the scaling of the scratch forces. Therefore, it is imperative to check the integrity of the probe prior to scratch testing. Furthermore, the probe must be cleansed by gently rubbing a cotton swab saturated in Isopropyl alcohol.

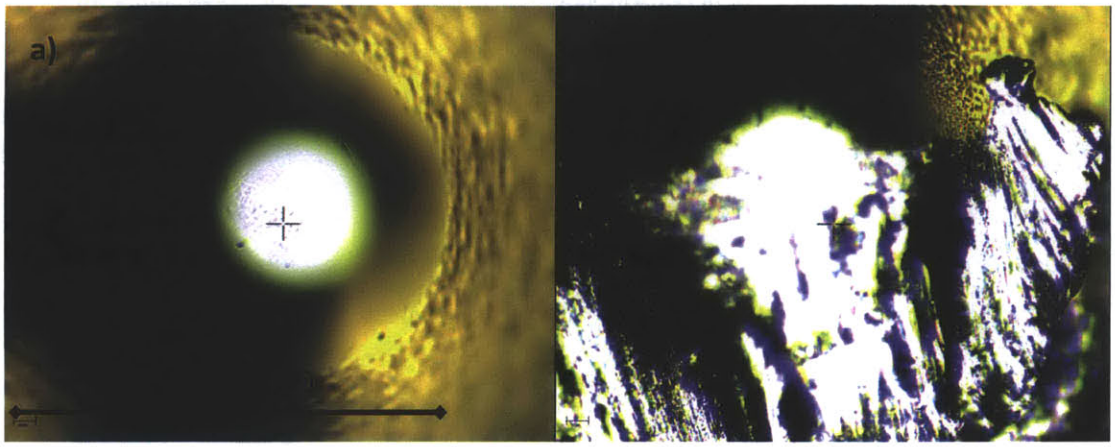

Figure 5-4: Optical images of intact and broken 200 μm Rockwell diamond probe. a) clean and intact probe. b) broken probe.

5.1.3 Calibration

After the specimen have been washed and dried, and after the scratch probe has been cleansed, the next step is to test the calibration specimens. Each specimen is glued to a square stainless steel plate, 25-mm wide and 12-mm thick, and then mounted on a scratch rectangular holder as shown in Figure 5-3. In particular, this way of gluing and mounting specimen was shown to yield the least amount of specimen compliance during scratch testing. A matrix of scratch tests are then performed with a clean and unbroken Rockwell C diamond probe, the parameters of each test being summarized in Table 5.1: twenty-four tests are performed on Lexan 9034 and two tests are performed on fused silica. After testing, the recorded horizontal force and penetration depth are extracted.

The analytical model predicts the following expression of the shape function $2pA_{LB}$, for a cone of half-apex angle θ and for a sphere of radius R, respectively:

$$2pA_{LB} = 4\frac{\tan\theta}{\cos\theta}d^3, \quad 2pA_{LB} = \frac{32}{3}d^2R \tag{5.2}$$

The maximum depth of penetration ranges within $7-10$ μm for fused silica and 120-160 μm for Lexan 9034. Below the sphere-to-cone transition depth, 26 μm, the probe is assumed to be a perfect sphere and the horizontal scratch force is expected to be a square function of the penetration depth. As for Lexan 9034, the maximum depth of penetration is four times above 26 μm. As a consequence, the scratch probe is assumed to behave as a perfect cone in that range, and the horizontal force F_T is expected to be a cubic function of d. Therefore, a nonlinear regression is then performed to fit the squared horizontal force-penetration depth curve, $F_T^2/(R_0^3 K_c^2)(d/R_0)$, to functions of the form, $y = \beta x^2$ for fused silica and $y = \alpha x^3$ for Lexan 9034; with $R_0 = 200$ μm. Figure 5-5 a) and b) show an example of shape function curves for both fused silica and Lexan 9034. In particular, the fitted functions matches well the experimental data with high coefficient of correlation, $R^2 = 0.9923$ for fused silica, and $R^2 = 0.9901$ for Lexan 9034. From the values of the fitted coefficients, α and β, 14.61 and 54.51 respectively, we can derive the effective cone half-apex angle, θ, and probe tip radius, R, using Eq. (5.2). The calculated effective half-apex angle is 60.74°, well within the manufacturer's specification range 60° $\pm$ 5°. The calculated effective tip radius is $R = 1.02$ mm. This value is five times greater than the theoretical value, 200 μm, which is indicative of high blunting at the tip of the probe ($d \leq 10$ μm). Having shown the scratch probe calibration method, we will focus on the conical range and show that the measured scratch probe function is a geometrical property that is independent on external factors such as the surface cleanliness, the probe wear or the choice of reference material.

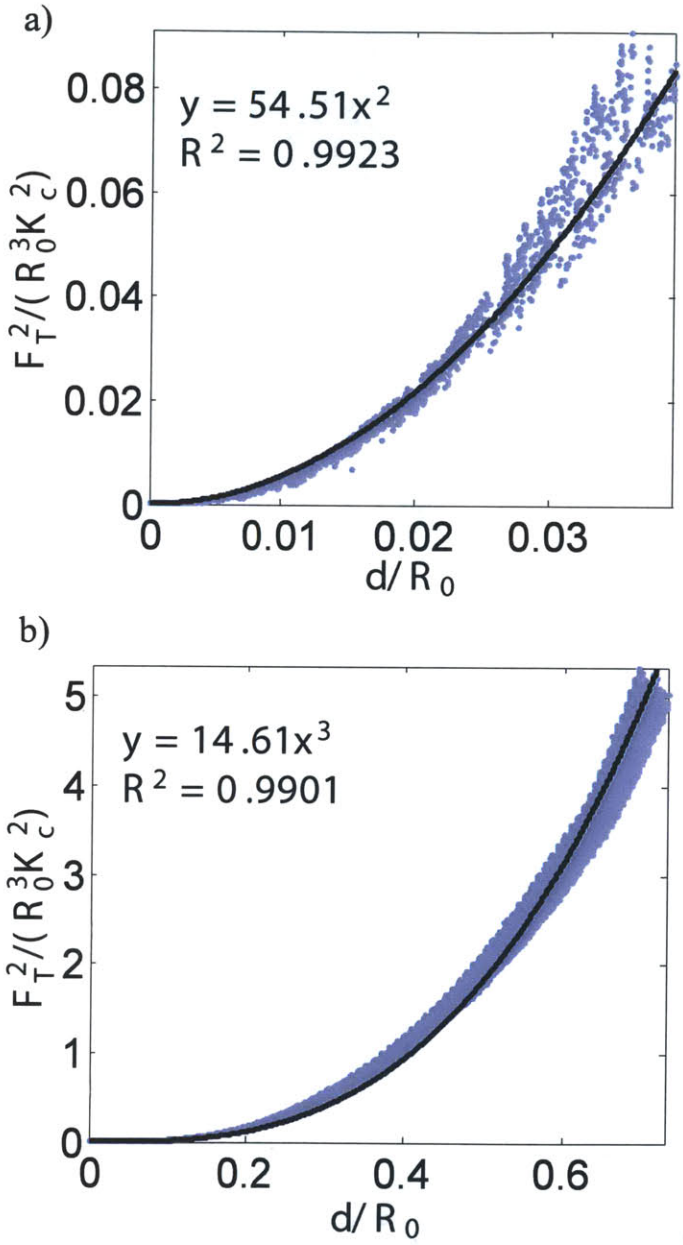

Figure 5-5: Example of calibrated shape function curves for scratch testing with a 200 μm Rockwell diamond probe. The shape function is $2pA_{LB} = F_T^2/(K_c^2 R_0^3)$ where $R_0 = 200$ μm. a) Tests on fused silica. b) Tests on Lexan 9034.

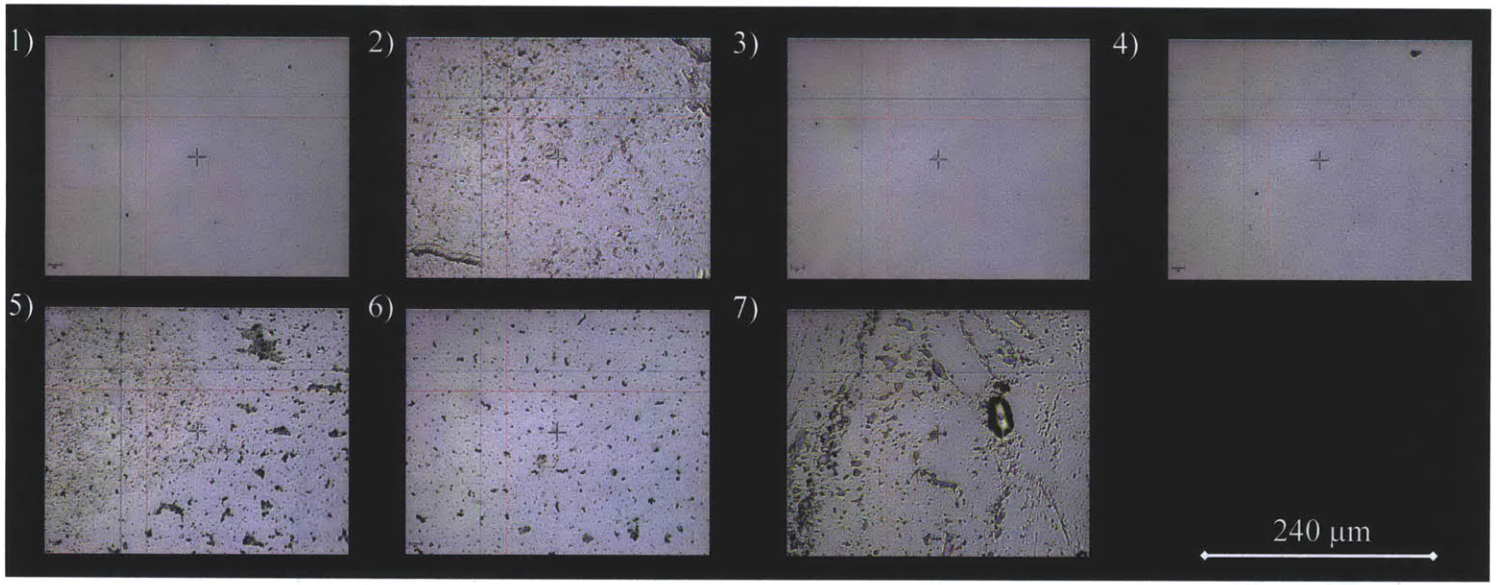

Figure 5-6: Optical image of Lexan 9034 specimens surface after cleansing and drying. 1) Specimen 1. 2) Specimen 2). 3) Specimen 3). 4) Specimen 4. 5) Specimen 5. 6) Specimen 6. 7) Specimen 7). 1) 3) and 4) are "clean" surfaces whereas 2), 5), 6) and 7) are "dirty" surfaces.

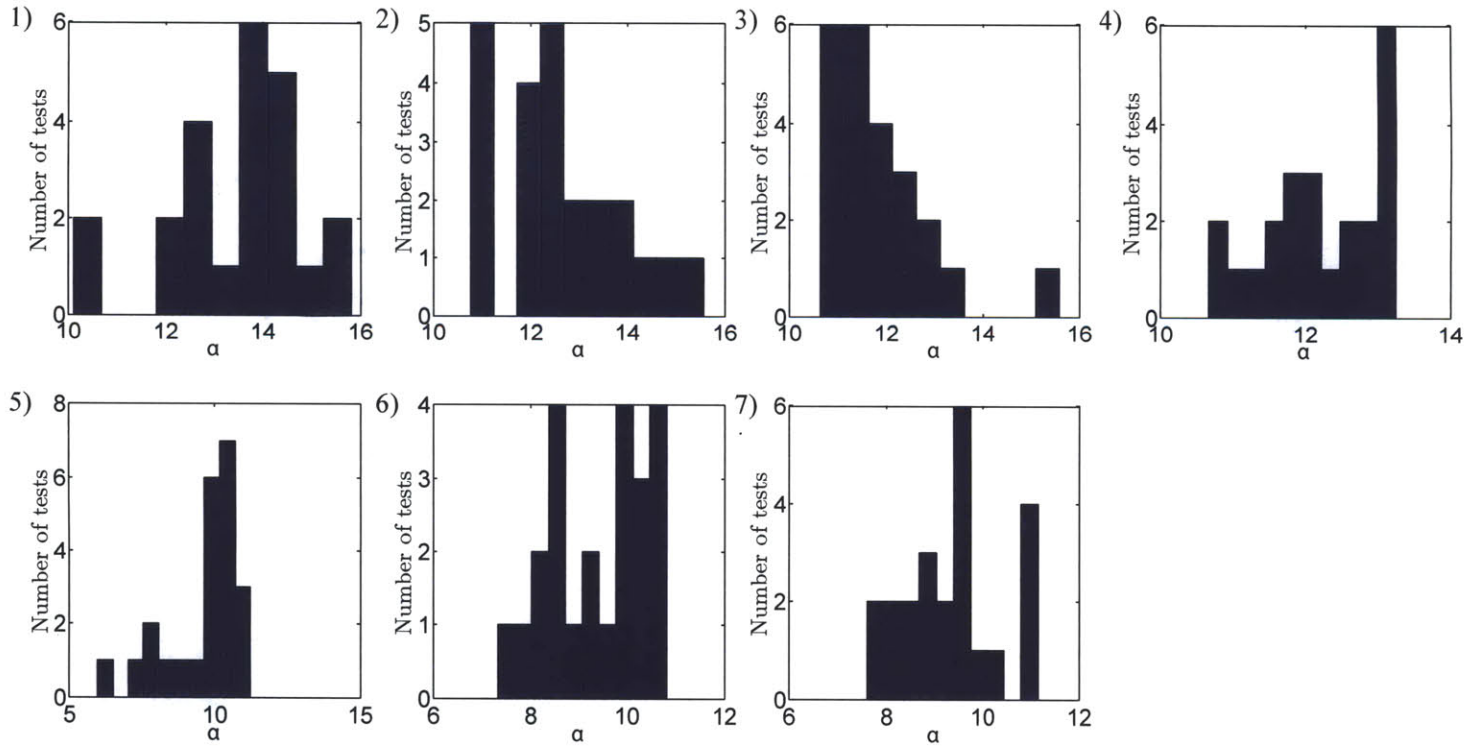

Figure 5-7: Histogram showing the values of the fitted coefficient α for Lexan 9034 specimen. 1) Specimen 1. 2) Specimen 2). 3) Specimen 3). 4) Specimen 4. 5) Specimen 5. 6) Specimen 6. 7) Specimen 7). 1) 3) and 4) are "clean" surfaces whereas 2), 5), 6) and 7) are "dirty" surfaces.

5.2 Influence of Surface Cleanliness and Scratch Probe Tip Wear

5.2.1 Influence of the Surface Cleanliness

Several factors can affect the depth and force measurement during a scratch test: room temperature, humidity, specimen moisture content, etc. The goal of this investigation is to assess the influence of surface impurities on the measured calibration function. To this end, 7 specimens were prepared following the procedure described in Section 5.1.1, with a major modification. In fact, after drying, the specimen were stored for four days, heated again in an oven for twenty-four hours to release any moisture and then cooled for twenty-four hours prior to testing. The storage allowed the deposition of impurities on the surface.

Figure 5-6 shows the optical images of the specimen surfaces, obtained with the Micro Scratch Tester optical microscope at a magnification level of 800X. Figs. 5-6-1), 5-6-3) and 5-6-4) are clear and clean. By contrast, Figs. 5-6-2), 5-6-5), 5-6-6) and 5-6-7) present stains, dots and scratches that can be attributed to contaminants, dust or dirt particles that accumulate on the surface. To ensure a clean surface as much as possible, we recommend to prepare the Lexan specimen exactly 48 hours prior to testing, wear hand gloves, and avoid any direct contact with the surfaces to be tested.

For each specimen, a set of 24 scratches were performed with the same scratch probe. The first test was discarded and only the remaining twenty-three were considered in the statistical analysis. Then for each individual scratch test, the squared horizontal force-penetration depth curve, $F_T^2/(R^3K_c^2)(d/R)$, was fit to a function of the form, $y = \alpha x^3$. Figure 5-7 displays the resulting histograms for the calibration coefficient α for all specimen meanwhile Table 5.2 lists the values of α as well as the equivalent effective half-apex cone angle. For "clean" surfaces, (specimen 1, 3 and 4), the range of coefficient α is between 10 and 16 and the average values vary from 11.87 to 13.47. For most "dirty" specimen, the range for α is lower, between 6 and 11 and the average values are

Specimen	Calibration coefficient α	Effective half-apex angle $\theta(°)$	Condition of the surface
1	13.47±1.41	59.60	Clean
2	12.61±1.29	58.64	Dirty
3	11.87±1.08	57.74	Clean
4	12.21± 0.80	58.16	Clean
5	9.58±1.33	54.37	Dirty
6	9.40± 1.02	54.06	Dirty
7	9.38±1.02	54.02	Dirty

Table 5.2: Testing parameters for the scratch probe calibration.

also lower, ranging from 9.38 to 9.58. For "clean" specimen the effective half-apex cone angle is within the manufacturer's specification range, 60° ± 5 °; which is not the case for "dirty" specimen, except for specimen 2. Moreover, knowing that all specimens were tested with the same 200 μm Rockwell diamond probe, we see that there is a variation of 7% in the fitted value of α for "clean" specimens. This means that the calibration procedure is extremely precise within a Lexan specimen (23 scratch tests) and from one Lexan block to another (here 23 scratch tests X 3 blocks). We can thus conclude that the cleanliness of the surface is of paramount importance in order to get an accurate and precise calibration of the scratch probe shape function.

5.2.2 Scratch Probe Tip Wear

The goal of this experiment was to investigate the presence of tool wear due to prolonged usage of the tip. For this purpose, seven scratch probes were examined, with an operating time ranging from 1 to 17 months, with an average daily use of five scratches per scratch probe. Seven different Lexan 9034 specimens corresponding to the seven probes were prepared and tested. For each probe and each Lexan block, a matrix of 8 × 3 scratch tests was carried out. After testing, the recorded horizontal force and penetration depth were extracted. A nonlinear regression was performed on each individual scratch test to fit the horizontal force-penetration depth curve, $F_T(d)$, to a function of the form, $y = \alpha x^3$. Table 5.3 lists the fitted calibrating coefficients, α, as well as the corresponding effective

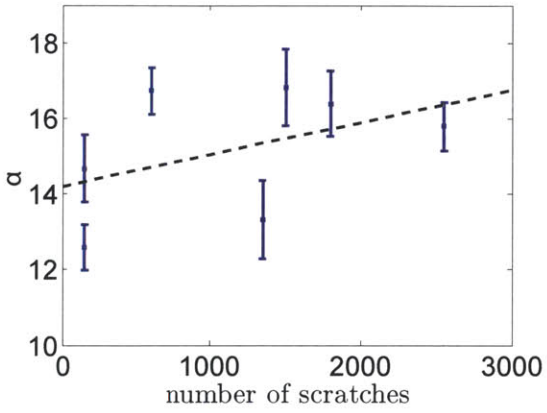

Figure 5-8: Calibration coefficient α as a function of the number of scratches performed.

cone half-apex angle. Figure 5-8 plots α versus the number of scratch tests performed with the probe. A linear regression is performed and yields $y = 8.4910^{-4}x + 14.21$: this means that prolonged use of the probe leads to a slight blunting of the probe. However the correlation is very weak: $R^2 = 0.2010$; and the slope- 8.4910^{-4}/scratch- is very small. Therefore, we can neglect the tool wear on the scratch probe. However, we recommend to keep the number of scratches less than 150, which ensures that the relative increase of α remains less than 1%.

5.3 Repeatability

In summary, the following conditions must be met for the scratch probe function to be a purely geometry factor: the scratch probe must be clean, unbroken and new (less than 150 scratch tests performed) and the Lexan 9034 specimens must be prepared as indicated in Section 5.1.1. In the next section we show that the scratch probe function does not depend on the choice of the calibrating material and that in the conditions specified, the fracture toughness determination method is highly reproducible.

Probe serial number	Operating time (months)	Number of scratch tests performed	Calibration coefficient α	Effective half-apex cone angle θ
D-214	1	150	12.59±0.60	58.61
H-298	1	150	14.67 ± 0.89	60.80
H-297	4	600	16.73±0.62	62.57
E-259	9	1350	13.33±1.04	59.45
G-209	10	1500	16.83±1.01	62.85
G-200	12	1800	16.4±0.85	62.31
E-266	17	2550	15.80 ± 0.64	61.80

Table 5.3: Influence of the use on the probe shape function. The number of scratch tests performed is calculated assuming a daily use of 5 scratches per day per probe.

5.3.1 Reference Calibration Material

Lexan 9034 was chosen as a calibrating material for scratch testing with a Rockwell C diamond probe in the conical range, because it can be easily provided by plastic manufacturers and because of its softness, which enables the calibration within the range of penetration depth commonly used for geologic materials. In this section we verify the claim that the calibrated shape function is independent on the reference material. For this purpose, a paraffin wax mixture was chosen as an alternative reference material.

The mixture consisted of paraffin wax (Exxon Mobil brand) with 2% additive Vybar 260. Both the wax and the additive were purchase from Polygon Corporation, Boston. In order to assess the fracture toughness, three-point bending tests were performed on 58mm X 180mm X 34 mm specimens with a single edge notch at a cross-head speed of 25.4 mm/min. The measured fracture toughness value was 0.082±0.017 MPa$\sqrt{\text{m}}$. Table 5.4 summarizes the mechanical properties of both Lexan and paraffin wax. Whereas the Young's moduli are of the same order of magnitude, Lexan has a uniaxial compressive strength and a fracture toughness more than an order of magnitude greater than those of paraffin wax.

Scratch tests were performed with the same scratch probe, G-209, on both Lexan 9034 and paraffin wax. The Lexan sample was prepared according to the procedure

Material	Young Modulus (GPa)	Uniaxial Compressive Strength (MPa)	Fracture Toughness (MPa$\sqrt{\text{m}}$)
Lexan 9034	2.5	86	2.69
Paraffin wax (Exxon Mobil)	1.2	2	0.082 $\pm$0.017

Table 5.4: Mechanical properties of Lexan 9034 and paraffin wax

Scratch length (mm)	Scratch speed (mm/min)	Loading rate (N/min)	Maximum vertical force (N)
3	6	60	30
3	6	4	2

Table 5.5: Testing parameters for Lexan 9034 and paraffin wax.

described in Section 5.1.1. As for the paraffin wax, the sample preparation procedure involved machining, coarse and fine grinding, cleansing by ultrasonication in Alconox solution and then distilled water and finally drying in a glass jar at room temperature. The testing parameters were different for paraffin wax. In particular, the prescribed maximum force was 2 N, an order of magnitude smaller than that of Lexan, to reflect the difference in strength between both materials and to achieve comparable ranges of penetration depths. On the other hand, the scratch length and the scratch speed were kept equal. Table 5.5 summarizes the testing parameters for both materials.

Figure 5-9 displays the shape function curves obtained for the scratch probe G-209 with Lexan 9034 and paraffin wax. Table 5.6 lists the resulting calibration coefficients and effective half-apex cone angles. The relative error between the calibration coefficient of Lexan and that of Paraffin wax is small, 13 %. Therefore the calibrated shape function is independent of the reference material, as long as it is homogeneous, linear elastic isotropic and soft enough to reach similar penetration depth ranges. Nevertheless we recommend the use of Lexan 9034, following the procedure detailed above in order to calibrate the scratch probe shape function.

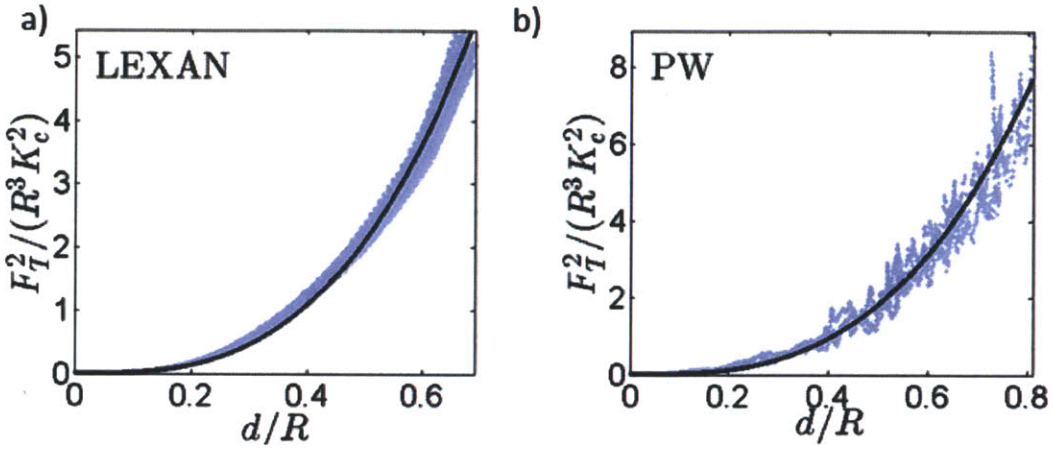

Figure 5-9: Calibrated shape function obtained on the same scratch probe G-209 with a) Lexan and b) Paraffin Wax

Material	Calibrating coefficient α	Coefficient of correlation R^2	Effective half-apex cone angle θ (°)
Lexan 9034	16.76	0.9896	62.59
Paraffin wax (Exxon Mobil)	14.53	0.9554	60.67

Table 5.6: Calibrating coefficient obtained with Lexan and Paraffin wax on the scratch probe G-209.

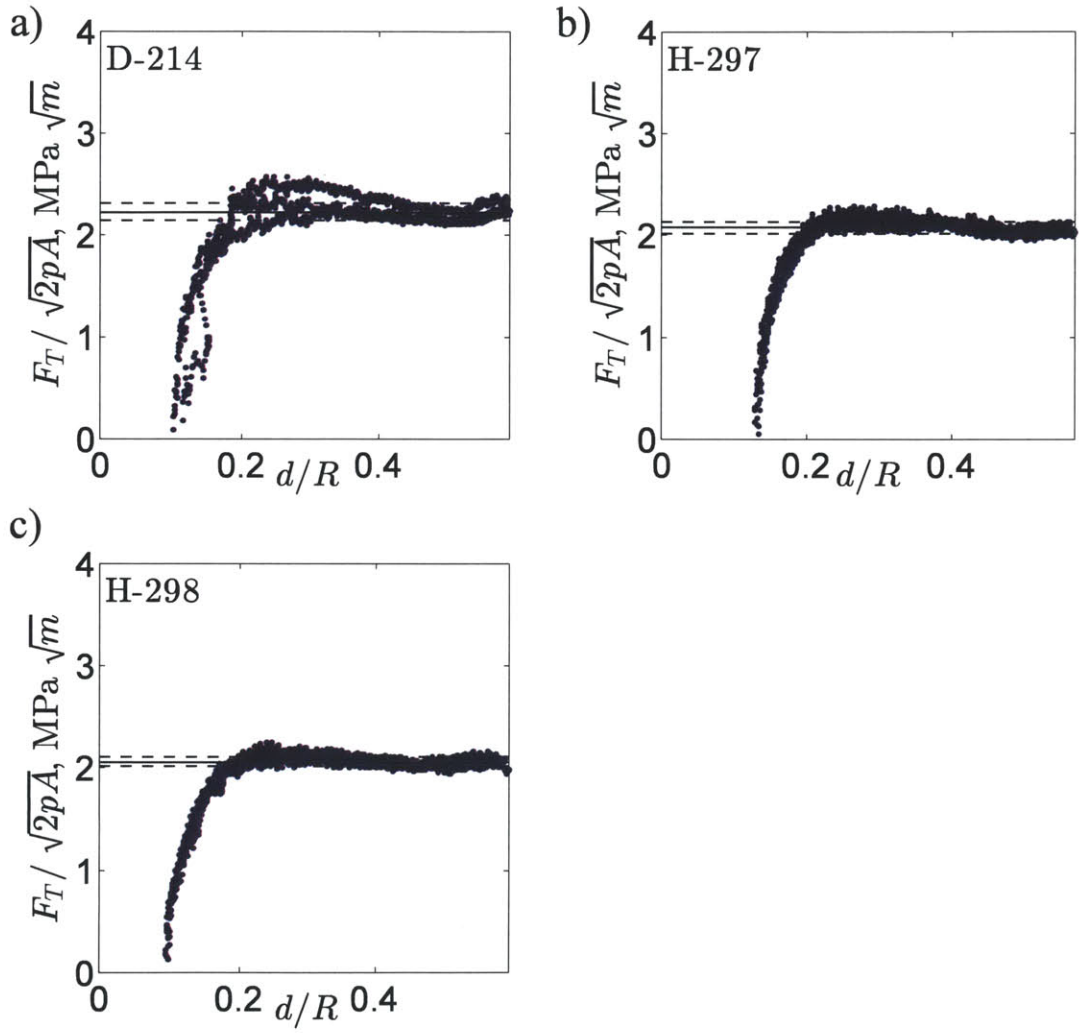

Figure 5-10: Assessment of the fracture toughness of Delrin using three different scratch probes: a) D-214, b) H-297 and c) H-298.

Probe serial number	Calibrating coefficient α	Effective half-apex cone angle θ (°)	Predicted fracture toughness K_c (MPa$\sqrt{\text{m}}$)
D-214	11.68	57.49	2.23±0.09
H-297	16.70	62.55	2.08±0.06
H-298	14.62	60.75	2.06±0.04

Table 5.7: Fracture toughness values predicted for Delrin using three different scratch probes.

5.3.2 Repeatability of the Fracture Toughness Determination Method

The goal of this paragraph is to verify the claim that Eq. (5.1) leads to measurements of the fracture toughness that are reliable, consistent and repeatable when the scratch probe is calibrated using the method described in Section 5.1.1. For this purpose micro scratch tests were performed on polyoxymethylene Delrin using three different scratch probes: D-214, H-297 and H-298. The material was provided by McMaster-Carr and was prepared using the procedure described for Lexan: cleansing with Alconox and distilled water, drying in an oven and at room temperature. Each scratch probe was calibrated prior to testing using Lexan as described in Section 5.1.3. Then a set of three micro-scratch tests was performed using the testing parameters given in Table 5.1. Table 5.7 shows the calibrating coefficients and the predicted fracture toughness. Figure 5-10 displays the variation of $F_T/\sqrt{2pA}$ versus d/R. For each scratch probe the predicted half-apex cone angle falls within the manufacturer specification range, 60° ±5°. Moreover, the curve $F_T/\sqrt{2pA}$ converges towards an asymptotic value, which reflects the shift from an initial state where fracture dissipation is negligible to a fracture-driven process where the fracture resistance can be assessed by Eq. (5.1). For a given probe the uncertainty on the predicted fracture toughness is less than 4%. From the individual fracture toughness values, 2.23±0.09 MPa$\sqrt{\text{m}}$, 2.08±0.06 MPa$\sqrt{\text{m}}$ and 2.06±0.04 MPa$\sqrt{\text{m}}$ we can estimate the overall fracture toughness: 2.18±0.04 MPa$\sqrt{\text{m}}$. Thus, the uncertainty on the measurement of the fracture toughness remains less than 4%.

5.4 Chapter Summary

A protocol has been established to calibrate the shape function of a 200 μm Rockwell diamond probe, using 99.995% silicon dioxide and Lexan 9034 as reference materials, for testing in the spherical ($d \leq 10$ μm) range and in the conical ($d > 26$ μm) range respectively. This protocol involves the adequate preparation of calibration specimens through washing, rinsing and drying. For the conical range, the prediction of the probe half-apex angle is in agreement with the specifications from the manufacturer. However, for the spherical range, there is considerable blunting of the probe tip. Moreover, the presence of impurities or debris at the surface of Lexan can degrade locally the fracture properties thus leading to an erroneous shape function. Therefore, the cleanliness of the surface to be tested is of paramount importance. Moreover, the wear of the probe tool due to prolonged usage is negligible as long as the number of scratch tests is less than 150. Moreover, the shape function is independent on the reference material as long as the reference material is homogeneous linear elastic isotropic and the penetration depth ranges are similar. Finally, for homogeneous materials, the predicted fracture toughness value is independent of the scratch probe within 10% of relative uncertainty. We thus have an operational probe calibration procedure in place that can be used for refined scratch test applications, such as the study of rate effects. This is shown next.

Chapter 6

Experimental Validation

In part II, an analytical model was developed to express the fracture toughness in function of the force and depth measurement during a scratch test with an axisymmetric probe. In particular, the horizontal scratch force F_T is related to the fracture toughness K_c via:

$$\frac{F_T}{\sqrt{2pA_{LB}}} = K_c \tag{6.1}$$

where p is the scratch probe perimeter, A_{LB} is the horizontal projected load-bearing contact are and $2pA_{LB}$ is the scratch probe shape function. Chapter 5 has shown that the probe shape function is independent of external factors such as the choice of reference material, the probe tip wear or the calibration material surface cleanliness. Moreover a protocol has been developed and validated in order to calibrate the scratch probe shape function. Given a clean unbroken and new (less than 150 scratch tests performed) scratch probe and by using Lexan 9034 as a reference material as specified in Chapter 5, the method for fracture determination was shown to be reproducible for homogeneous materials, with a relative uncertainty less than 13%.

The goal in this chapter is to validate the accuracy of the fracture determination method on homogeneous materials, by confronting the fracture toughness measured at the microscopic scale to macroscopic measurements, obtained via conventional fracture-

testing methods such as the three-point bend test on single-edge notched specimens. First we introduce the materials, then we take a closer look at the scaling of the horizontal scratch force. Finally, the predicted fracture toughness values are compared with data from the scientific literature.

6.1 Materials and Methods

6.1.1 Materials

The materials investigated in this chapter are summarized in Table 6.1. They were chosen to cover at least two orders of magnitude in fracture toughness. They include three ceramics (soda lime glass, Pyrex glass and fused silica), three polymers (paraffin wax Japanese Brand, Delrin® 150E, and Lexan), one soft metal (Aluminum 2024-T4/T351), and three hard metals (cold drawn steel AISI-1045, cold drawn steel AISI-1144 and annealed Titanium 6Al-4V). Metals and ceramics were supplied by McMaster-Carr (Robbinsville, NJ) as rods with a radius ranging from 1.3 cm to 1.9 cm. Delrin® 150 E was also supplied as a 1.3 cm-diameter rod, whereas a 1.3 cm thick Lexan plate was purchased from General Electric. Finally, slabs of paraffin wax (Japanese brand) were purchased from Polygon Wax.

6.1.2 Material Preparation Method

The main objectives of the surface sample preparation are: (1) to achieve as flat as possible a surface, (2) to increase the accuracy of the determination of the fracture toughness, and (3) to obtain repeatable results. The procedure described below is inspired from standard materials polishing methods used for nano-mechanics testing such as nano-indentation [77] .

The first step consists in cutting a specimen of appropriate size with a brand saw or with a water-jet cutting machine. The specimens were cylindrical with a diameter

Material	Description
Ceramics	
Fused silica	99.995% SiO2
Pyrex glass	Heat-resistant borosilicate glass
Soda lime glass	
Polymers	
Paraffin wax	Japanese brand
Delrin® 150E	Polyacetal homopolymer
Lexan	Bisphenol-A polycarbonate
Metals	
AA 2024-T4/T351	High strength aluminum
AISI-1045	High strength medium-carbon steel, cold drawn
AISI-1144	High strength carbon steel, cold drawn
Titanium 6Al-4V	Grade 5 titanium, annealed

Table 6.1: Materials description

ranging from 1.3 cm to 1.9 cm and with a height less than a centimeter.

The second step consists in flattening the faces of the specimen with a milling machine. The third step is a coarse grinding step. The aim of this step is to improve the parallelism of the top and bottom faces. This is done with a 240 grit Aluminum Oxide sanding paper (McMaste-Carr). Afterward, the sample is cleaned in an ultrasonic water bath for 5 minutes.

The last step is manual dry polishing. A Fibremet® (Buehler) abrasive disc of a given size is mounted on a flat glass surface and the surface of the specimen is gently brushed against the abrasive disc for 30 seconds to 1 minute. Four different sizes of abrasive are consecutively used: 9 μm, 3 μm, 1 μm and 0.3 μm.

The final arithmetic average roughness achieved, R_a, ranged from 0.01 μm to 1.55 μm with an average of 1.17 μm and a standard deviation of 1.21 μm. These values were more than an order of magnitude smaller than the maximal depth of penetration during the scratch test.

Material	Equipment	Prescribed maximal normal force (N)
Ceramics		
Fused Silica	Micro scratch tester	7
Pyrex glass	Micro scratch tester	7
Soda lime glass	Micro scratch tester	7
Polymers		
Paraffin wax (Japanese brand)	Micro scratch tester	30
Delrin® 150E	Revetest scratch tester	50
Lexan	Micro scratch tester	30
Metals		
AA2024-T4/T351	Revetest scratch tester	150
AISI-1045	Revetest scratch tester	150
AISI-1144	Revetest scratch tester	100
Titanium 6Al-4V	Revetest scratch tester	150

Table 6.2: Testing parameters. In all tests the scratch length was 3mm and each test lasted 30 s

6.1.3 Test Parameters

Because for a conical indenter the forces scale in a self-similar way, the maximal vertical load for testing was chosen so as to have, for each material, a maximal depth in the conical range of the indenter. For metals and polymers, the maximal load ranged from 50 N to 200 N for tests with the Revetest Scratch Tester and was equal to 30 N for tests with the Micro Scratch Tester. However, due to their high brittleness, ceramics exhibited a lot of chipping when tested at such high loads: this led to some fluctuations of both penetration depth and horizontal force. To reduce the amount of chipping, very low loads, 7 N, were used and, consequently, the tests occurred in the spherical region of the indenter. For all tests, the scratch length was 3 mm and the loading rate ranged from 14 N/min to 300 N/min so that each test lasted 30 s. The parameters of the testing procedure are summarized in Table 6.2.

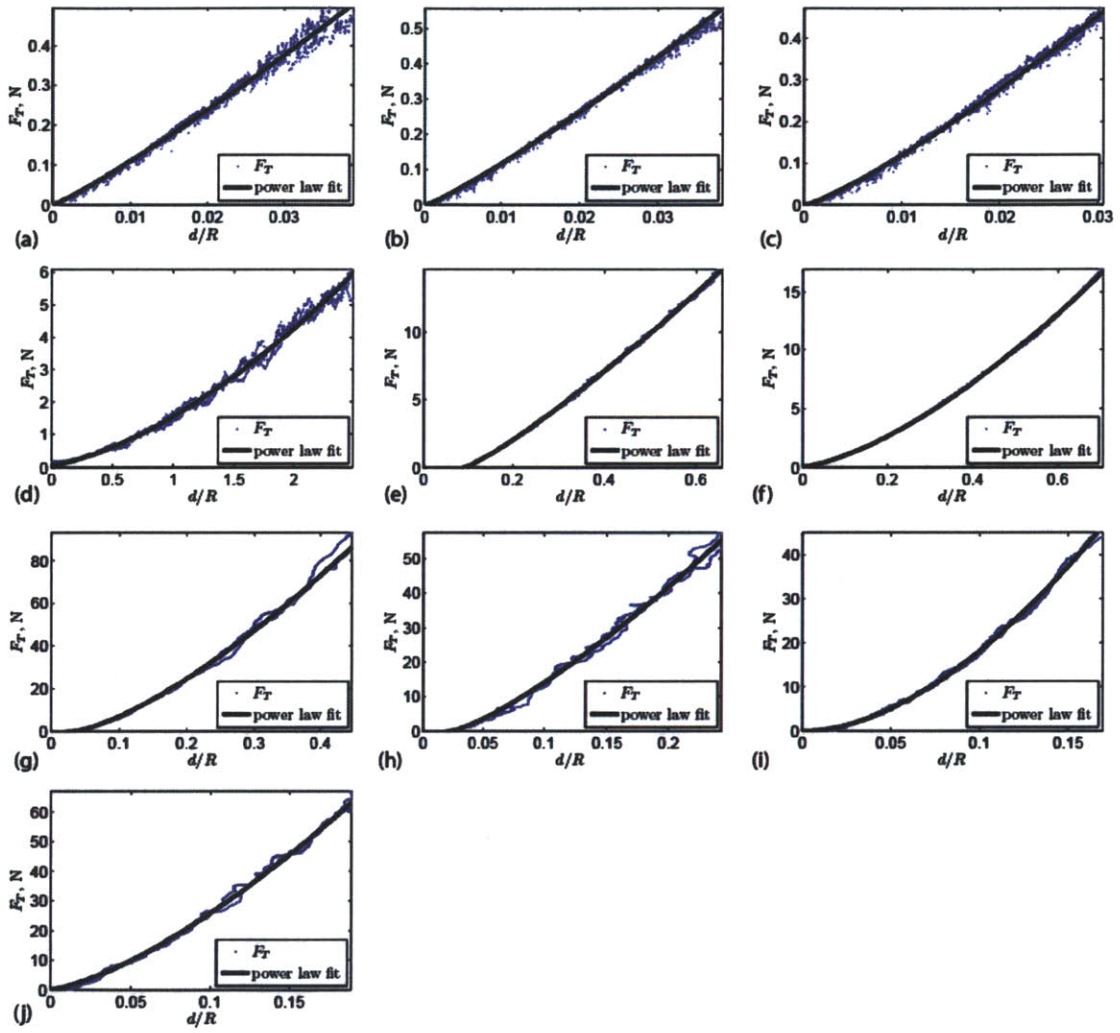

Figure 6-1: Horizontal force- penetration depth curves. (a) Fused silica. (b) Pyrex. (c) Soda lime glass. (d) Paraffin wax (Japanese brand). (e) Delrin® 150E. (f) Lexan. (g) AA2024-T4/T351. (h) AISI-1045. (i) AISI-1144. (j) 6Al-4V titanium.

6.2 Scratch Test Results

6.2.1 General Characteristics of the Load-Penetration Depth Curves

Figure 6-1 displays the horizontal load-penetration depth curves obtained for the materials used in this study. The horizontal force F_T in these different tests spans two orders of magnitudes: $F_T < 1$N for ceramics, $F_T < 10$ N for polymers and $F_T < 100$ N for metals. The ratio of penetration depth-to-indenter radius, d/R, is in the range 0-0.04 ($0 \leq d \leq 8\mu m$) for ceramics and in the range 0-2.5 ($0 \leq d \leq 500\mu m$) for polymers and metals.

The theoretical horizontal force- penetration depth relationships obtained in Chapter 3 for a cone of half-apex angle θ and for a sphere of radius r are recalled below:

$$F_T = 2\frac{\sqrt{\sin\theta}}{\cos\theta}K_c d^{3/2}; \quad F_T = \frac{4\sqrt{2}}{3}K_c d\sqrt{R} \tag{6.2}$$

In particular, for the horizontal scratch force scales as d for a sphere and as $d^{3/2}$ for a cone. The curve F_T vs d/R was fitted, using a nonlinear least squares procedure, to the model function $y = a(x - c)^b$. The fitting parameters for all materials are summarized in Table 6.3. For ceramics, the penetration depth lie within the spherical range of the Rockwell indenter. As predicted by the theory, the exponent, b, is very close to 1. This agreement between theory and experiments persists in the conical range. As for polymers with maximum penetration depths well in the conical range, $d_{max}/R > 0.6$ ($d > 120$ μm) , the exponent b is close to 1.5, except for Delrin® 150E. Finally, for metals, except for AISI-1144, the exponent b is between 1 and 1.5. This indicates that both the spherical and the conical part of the indenter are influencing the test.

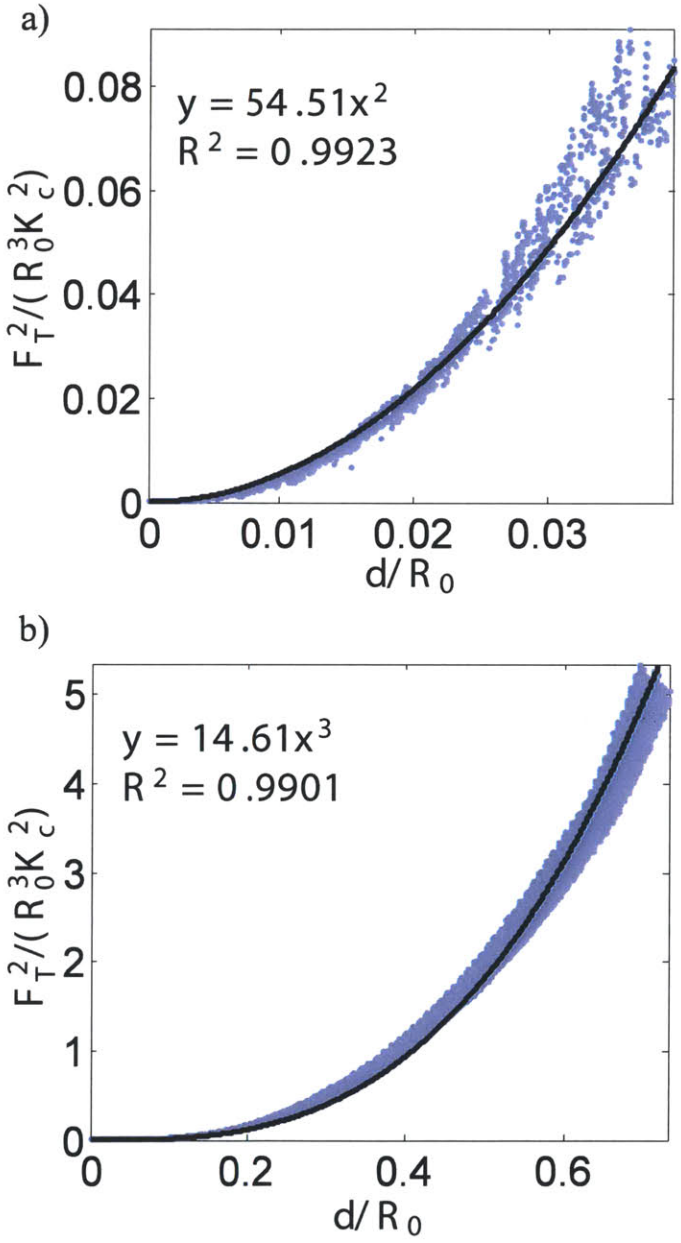

Figure 6-2: Calibrated shape function curves for scratch testing with a 200 μm Rockwell diamond probe. The shape function is $2pA_{LB} = F_T^2/(K_c^2 R_0^3)$ where $R_0 = 200$ μm. a) Tests on fused silica. b) Tests on Lexan.

Material	$a(N)$	b	c	R^2
Ceramics				
Fused Silica	18.50	1.11	0.00	0.9901
Pyrex glass	24.33	1.16	0.00	0.9977
Soda lime glass	31.27	1.20	0.00	0.9947
Polymers				
Paraffin wax (Japanese brand)	1.56	1.5	0.00	0.9907
Delrin® 150E	29.02	1.19	0.09	0.9992
Lexan	27.85	1.47	0.00	0.9995
Metals				
AA2024-T4/T351	291.10	1.38	0.03	0.9973
AISI-1045	401.82	1.30	0.02	0.9917
AISI-1144	1048.8	1.74	0.00	0.9972
Titanium 6Al-4V	634.85	1.39	0.00	0.9958

Table 6.3: Fitting parameters for the horizontal load-penetration depth curves, the model function being $y = a(x - c)^b$.

6.2.2 Calibration of the Indenter Shape Function

The scratch probe, a 200-μm diamond probe, was calibrated following the method described in Chapter 5 and the resulting calibrated shape functions is plotted in Figure 6-2. In particular, fused silica was used to calibrate the spherical range, $d \leq 10$ μm, whereas Lexan is used to calibrate the conical range, $d > 26$ μm. In particular, from the coefficient of the cubic function, $\alpha = 14.61$, we calculate the effective cone half-apex angle using Eq. (6.3), $\theta = 60.74°$, which is within the range of manufacturer's specifications, $\theta = 60° \pm 5°$. The evaluation of the effective tip radius, $R = 1.02$ mm, reveals a severe blunting of the tip for shallow penetration depths, $d \leq 10$ μm.

6.2.3 Fracture Toughness Predictions

In Figures 6-3 and 6-4, the quantity $F_T/\sqrt{2pA_{LB}}$, reminiscent of a stress intensity factor, is plotted versus d/R_0, where $R_0 = 200$ μ. Herein, we correct the quantity $(F_T^2)/R_0^3$ by

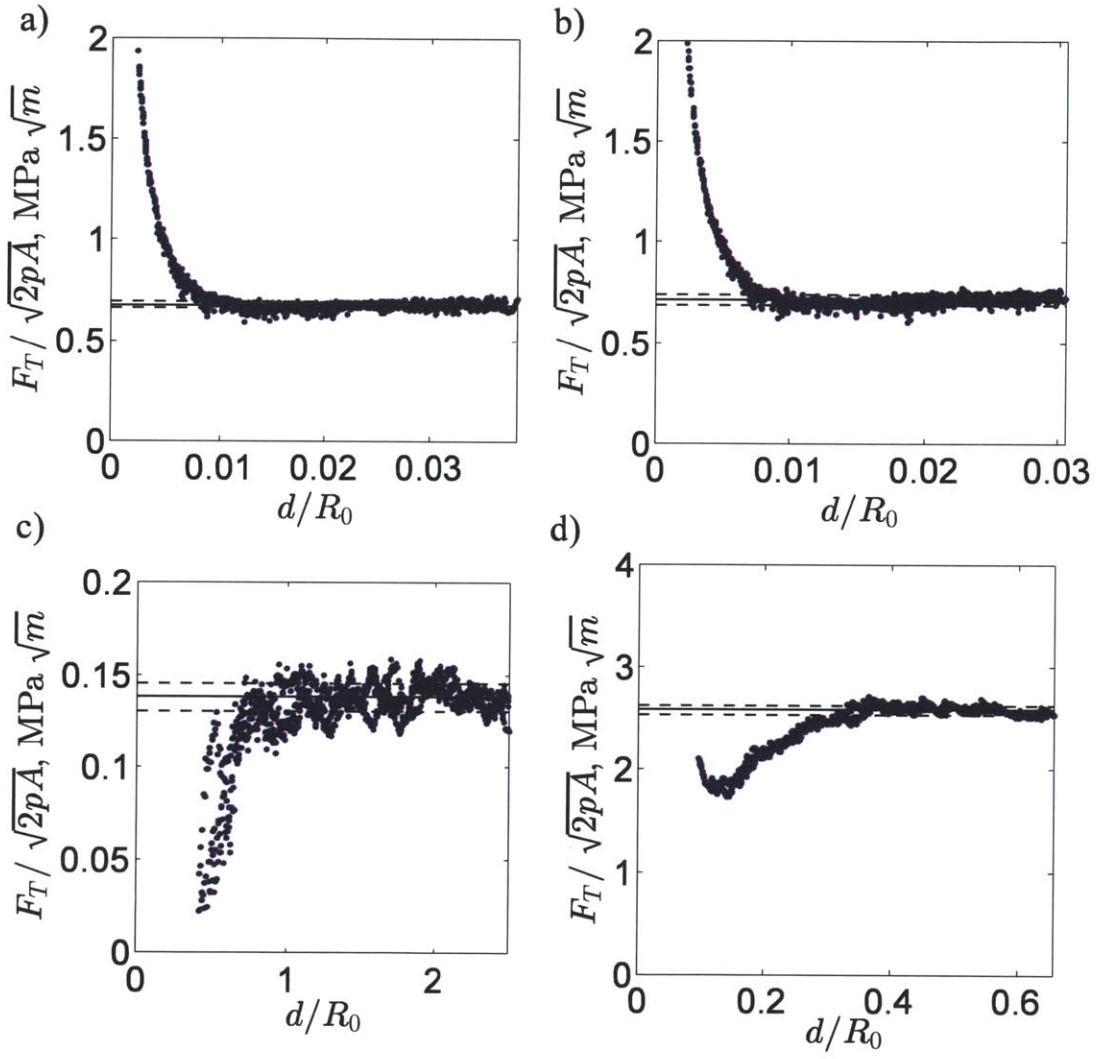

Figure 6-3: Fracture scaling of scratch tests: ceramics and polymers. F_T is the horizontal scratch force, $2pA_{LB}$ the scratch probe function, d the penetration depth and $R_0 = 200$ μ. a) pyrex. b) soda lime glass. c) Paraffin wax (Japanese brand). d) Delrin® 150E.

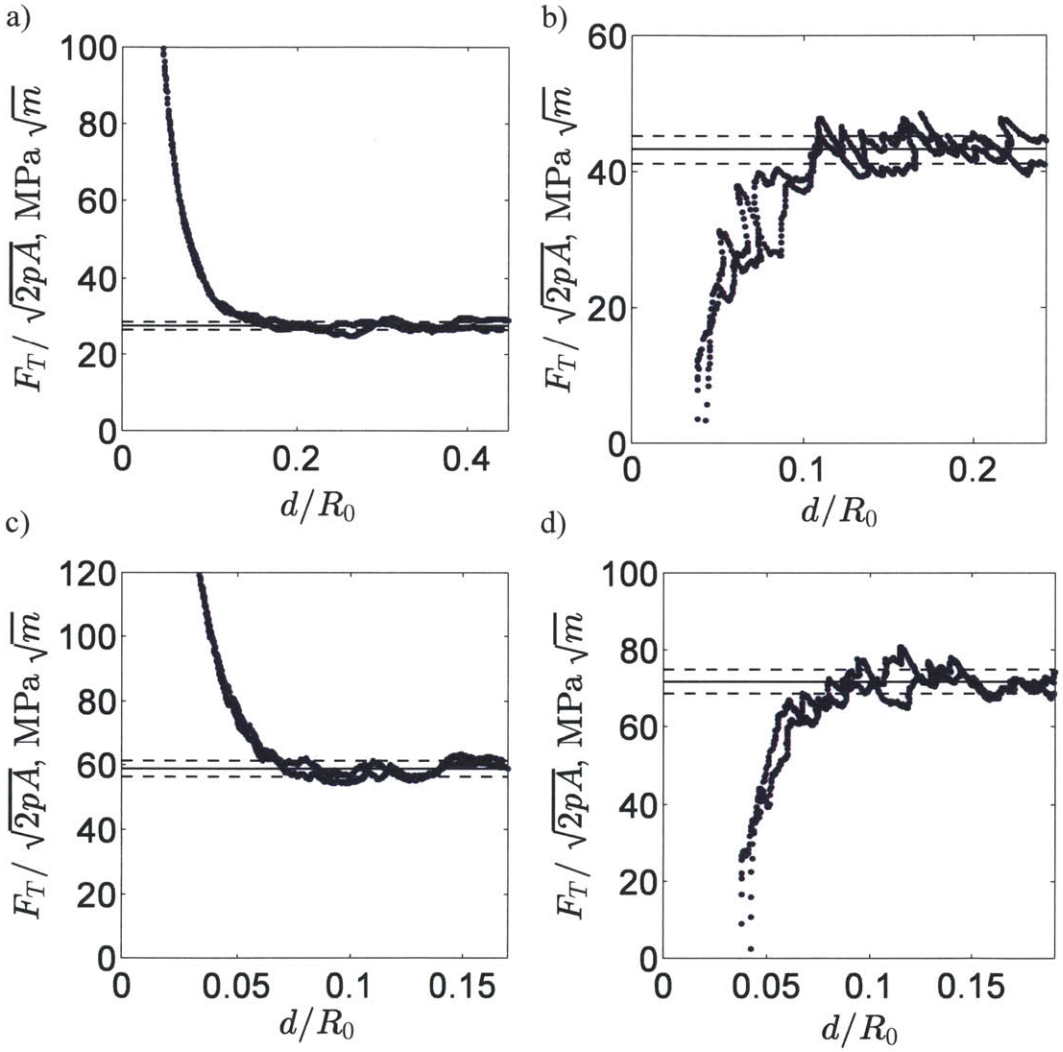

Figure 6-4: Fracture scaling of scratch tests: metals. F_T is the horizontal scratch force, $2pA_{LB}$ the scratch probe function, d the penetration depth and $R_0 = 200\ \mu$. a) Aluminum 2024. b) Steel AISI-1045. c) steel AISI-1144. d) Titanium 6Al-4V.

Material	Predicted K_c ($MPa\sqrt{m}$)	Macroscopic K_c ($MPa\sqrt{m}$)	Reference
Ceramics			
Pyrex glass	0.68±0.016	0.63	[46]
Fused Silica	0.71±0.03	0.7	[46]
Polymers			
Paraffin wax (Japanese brand)	0.14±0.01	0.15±0.01	Three-point bending tests
Delrin® 150E	2.59±0.05	2.8	[48]
Metals			
AA2024-T4/T351	27.5±1.15	26 (S-L direction) 32 (T-L direction) 37(L-T direction)	[5]
AISI-1045	43.25±2.12	50	[73]
AISI-1144	58.9±2.43	57 (T-L direction) 67 (L-T direction)	[73]
Titanium 6Al-4V	71.77±3.06	75	[5]

Table 6.4: Predicted scratch fracture toughness values versus macroscopic fracture toughness values.

substracting the off-set value of the linear fitting relation, $(F_T^2)/R_0^3$ vs. $2pA_{LB}/R_0^3$. For all materials, the dimensionless force converges toward a constant value as predicted by Eq. (6.1). At small depths of penetration, there is some deviation that can be attributed to localized plastic deformation. This convergence of $F_T\sqrt{2pA_{LB}}$ towards a straight line supports the hypothesis of the predominance of fracture processes at large penetration depths, which was postulated based on experimental evidence (cf Section 2.4).

Table 6.4 compares the fracture toughness values predicted from scratch tests with macroscopic values. The macroscopic fracture toughness values were obtained suing conventional fracture toughness testing such as the three-point bending test on single-edge notched specimens or compact tension tests [6]. For ceramics (pyrex and soda lime glass) and polymers (paraffin wax and Delrin® 150E), there is an excellent agreement between the predicted fracture toughness and the literature value, with a relative error ranging from 2% to 8%. Given the homogeneous, isotropic and elastic nature of these materials, the good agreement between experimental and literature fracture toughness

values validates the proposed fracture approach for scratch test interpretation. A similar agreement is generally found for the tested metals where the relative error is less than 10% for steel AISI-1045 and Titanium. As for Aluminum AA2024 and steel AISI-1144, the method proposed here does not account for anisotropic fracture behavior, which is the focus of Part IV of this thesis. However, the predicted K_c values are within the range of literature values. Finally, the method for fracture determination is very precise with a relative uncertainty less than 7%, which is in agreement with the conclusions of Chapter 5.

6.3 Chapter Summary

Throughout this thesis our method has been to closely combine experiments and theory in order to elucidate the physics behind microscopic scratch tests. In Chapter 2, we considered the scaling of the horizontal force and compared the theoretical predictions from Dimensional Analysis and Finite Element simulations with scratch test measurements. This in turn allowed us to conclude as the predominance of fracture processes in scratch tests. Furthermore, advanced imaging of the residual groove after scratch tests (Figure **??**) indicated that this predominance is valid at large depths of penetration and the generated cracks were found to be horizontal, curved and perpendicular to the direction of scratch testing. Based on the experimental observations, a rigorous Linear Elastic Fracture Mechanics was developed, that employed an energy-based approach in order to relate the scratch force to the scratch probe geometry and to the fracture toughness of the scratched material. The following relationship was obtained:

$$\frac{F_T}{\sqrt{2pA_{LB}}} = K_c \tag{6.3}$$

Chapter 5 developed an experimental protocol in order to calibrate the scratch probe function, $2pA_{LB}$, for scratch tests with a 200 μm Rockwell diamond probe . In particular,

it was demonstrated that $2pA_{LB}$ depends solely on the scratch probe geometry and is independent of external factors such as the scratch probe wear or the choice of reference material.

In this chapter, a method for fracture toughness using scratch tests was introduced and applied to ten materials including ceramics, metals and polymers. The following experimental observations were made:

- The scaling of the horizontal scratch force was in agreement with the predictions of the LEFM model (Chapter 3) as well as with the prediction of Dimensional Analysis (Chapter 2) for a fracture-driven process.

- The quantity, $F_T/\sqrt{2pA_{LB}}$ converged towards a straight line, which confirms the predominance of fracture processes at large depths of penetrations as postulated in Chapter 2.

- Using the scratch probe calibration method described in Chapter 5, the microscopic fracture toughness were calculated from Eq. (6.3). The predicted K_c values were in agreement with macroscopic values obtained with conventional fracture testing methods, with a relative error of less than 10%, and a relative uncertainty less than 7%.

Therefore, we have validated our method for fracture toughness determination for a wide range of materials, ceramics, polymers and metals and over a range of fracture toughness values spanning almost three orders of magnitude, from 0.15 MPa$\sqrt{\text{m}}$ for paraffin wax Japanese, to 75 MPa$\sqrt{\text{m}}$ for Titanium 6Al-4V. This method is reliable, accurate, precise and reproducible. In the rest of this thesis, we extend the fracture toughness determination method to more complex material behavior such as rate-dependence, anisotropy and heterogeneity.

Chapter 7

Coupling Indentation and Scratching For The Assessment of The Intrinsic Fracture Toughness

With a well calibrated and validated method in hand, the goal of this chapter is to apply the technique for the study of rate-dependent fracture behavior of visco-elastic materials. In fact, despite the wealth of analytical models [76, 11, 79] and experimental studies [14, 71, 37, 20, 63] of rate-dependent fracture processes, a handshake between theory and experiments remains still to be achieved, in order to distinguish intrinsic from rate-dependent fracture properties of rate-dependent materials. This is in short the focus of this chapter: to implement the analytical model developed in Chapter 4 to decouple creep from fracture via scratch tests performed on polymers. This chapter is composed of three sections. In the first section, the experimental program is presented. In the second section an inverse method based on the linear visco-elastic fracture model is developed, assuming either a Maxwell or a Generalized Maxwell visco-elastic behavior. The last section deals with the multi scale characterization of rate-dependence in the fracture behavior via a combination of macro and micro-scratch tests performed on paraffin wax.

7.1 Material and Methods

7.1.1 Materials

Polymers consist of chains of structural units created through the polymerization of different monomers. At temperatures much below the glass transition temperature, T_g, the mechanical behavior is glassy, whereas it is rubbery at temperatures above. In the range near T_g, the behavior is visco-elastic. Four polymers relevant for several modern engineering applications ranging from sound walls and sewage pipes to mechanical heart valves [86, 62, 45] are considered. These are amorphous polymers, namely paraffin wax Exxon Mobil, polycarbonate and polyvinyl chloride, and a semi-crystalline polymer, polyoxymethylene. Paraffin wax Exxon Mobil was provided by Polygon Corporation and mixed with an additive, Vybar 260 at a 2% concentration to reduce shrinkage. As for polycarbonate (PC), polyoxymethylene (Delrin®) and polyvinyl chloride (PVC), 1/4-inch thick sheets were purchased from McMaster-Carr under the trademarks respectively Makrolon, Delrin® and type I PVC. The glass transition temperatures are [86] 333 K for paraffin wax, 423 K for polycarbonate, 448 K for Delrin® and 344 K for polyvinylchloride; whereas the ambient temperature for all tests was 298 K.

The material preparation procedure for PC, POM and PVC was performed following the guidelines given in Section 5.1.1. The first step was to machine, with a saw stop table saw, specimens that are squares with a width of 25 mm and a height of 12 mm. Afterward, these specimens of PC, Delrin® and PVC were washed with a 1% solution of Alconox, rinsed under running water and annealed for 24 hours at 373 K to ensure a stress-free and moisture-free state. All specimens were then stored at room temperature in glass jars with tight lids and tested 24 hours later to prevent surface contamination.

7.1.2 Methods

Two sets of scratch tests were performed. For tests performed under a linearly increasing vertical force, the scratching speed values ranged from $V = 0.2$ mm/min to $V = 20$

mm/min and three loading rates were considered: $\dot{F}_V = 45$, 60 and 90 N/min for Delrin® and PVC and $\dot{F}_V = 3$, 4 and 6 N/min for paraffin wax. The prescribed maximum vertical force was $F_{V_{max}} = 30$ N for Delrin®, PC and PVC and $F_{V_{max}} = 2$ N for paraffin wax. For each combination of scratching speed and of loading rate, three scratch tests were performed. The resulting apparent fracture toughness, K_c^a, was derived using:

$$K_c^a = \frac{F_T}{\sqrt{2pA_{LB}}} \tag{7.1}$$

Additional tests were performed under a constant vertical force ($\dot{F}_V = 0$) and with scratching speed values ranging from $V = 0.4$ mm/min to $V = 20$ mm/min. For those tests, given a value of the speed, ten values of the vertical force ranging from $F_V = 0$ to $F_V = 30$ N (for Delrin®, PC and PVC) and $F_V = 2$ N (for paraffin wax Exxon Mobil) were considered. The apparent fracture toughness was then evaluated from the resulting depth of penetration and horizontal force following Eq. (7.1). For all tests, Lexan 9034 was used as the reference material to calibrate the scratch probe area function, $2pA$, according to the method developed in Chapter 5.

7.1.3 Scratch Test Results

We use Dimensional Analysis to rationalize the dependence of the apparent fracture toughness K_c^{a} upon relevant parameters such as the loading rate, $\dot{F}_V$, the scratching speed, V, the intrinsic rate-independent fracture toughness, K_c, and the visco-elastic parameters, represented here by an initial stiffness M and a discrete distribution of relaxation times τ_i, $i = 1 \ldots n$. That is,

$$\frac{K_c^{\mathrm{a}}}{K_c} = \mathcal{F}\left(\frac{V\tau_1 M^2}{K_c^2}, \frac{VM}{\dot{F}_V K_c^2}, \frac{\tau_2}{\tau_1}, \ldots, \frac{\tau_n}{\tau_1}\right) \tag{7.2}$$

Figures 7-1 and 7-2 plots the dimensionless quantity $K_c^{\mathrm{a}}/K_c^{ref}$ versus respectively

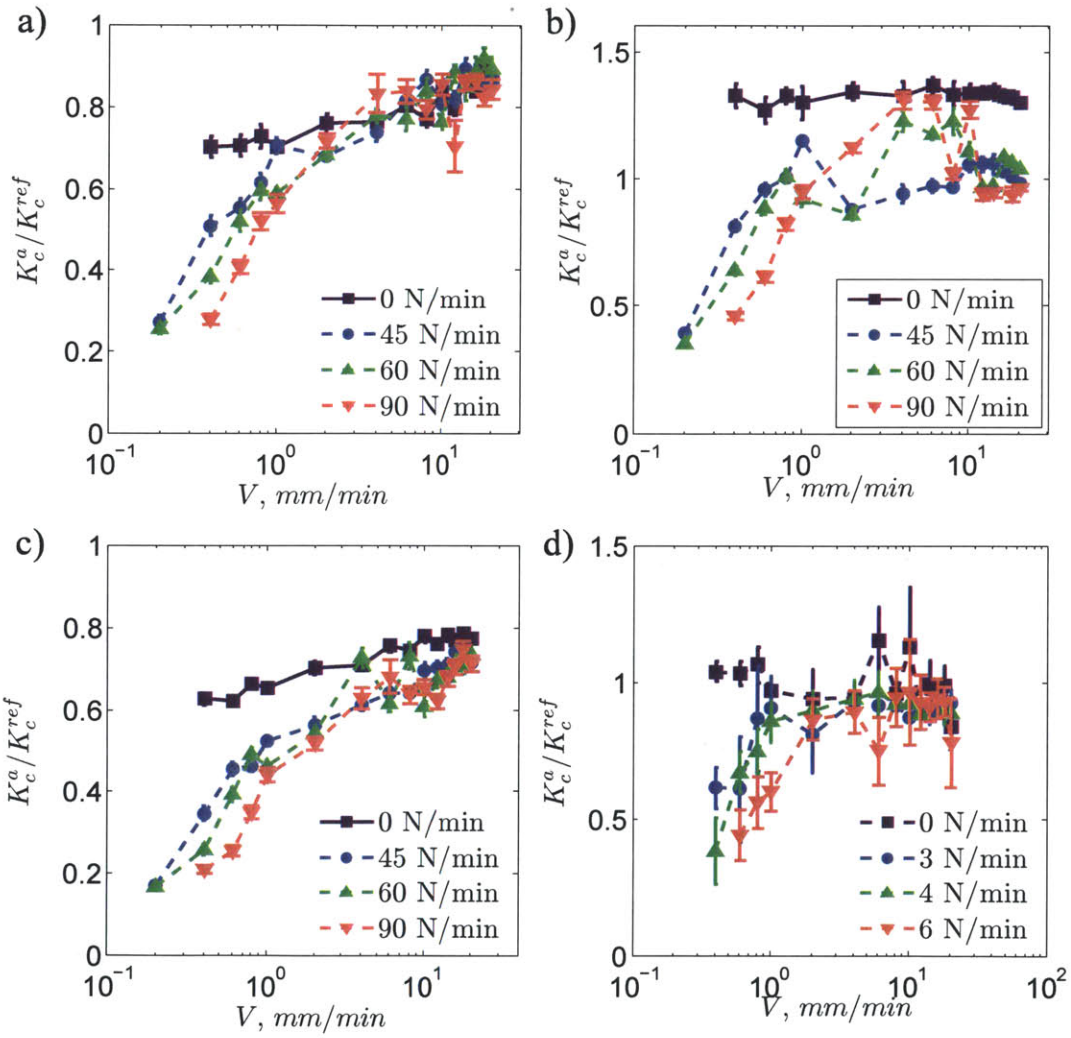

Figure 7-1: Apparent fracture toughness K_c^a versus scratching speed V. a) Delrin®. b) Polycarbonate (PC). c) PolyVinylChloride (PVC). d) Paraffin Wax Exxon Mobil.

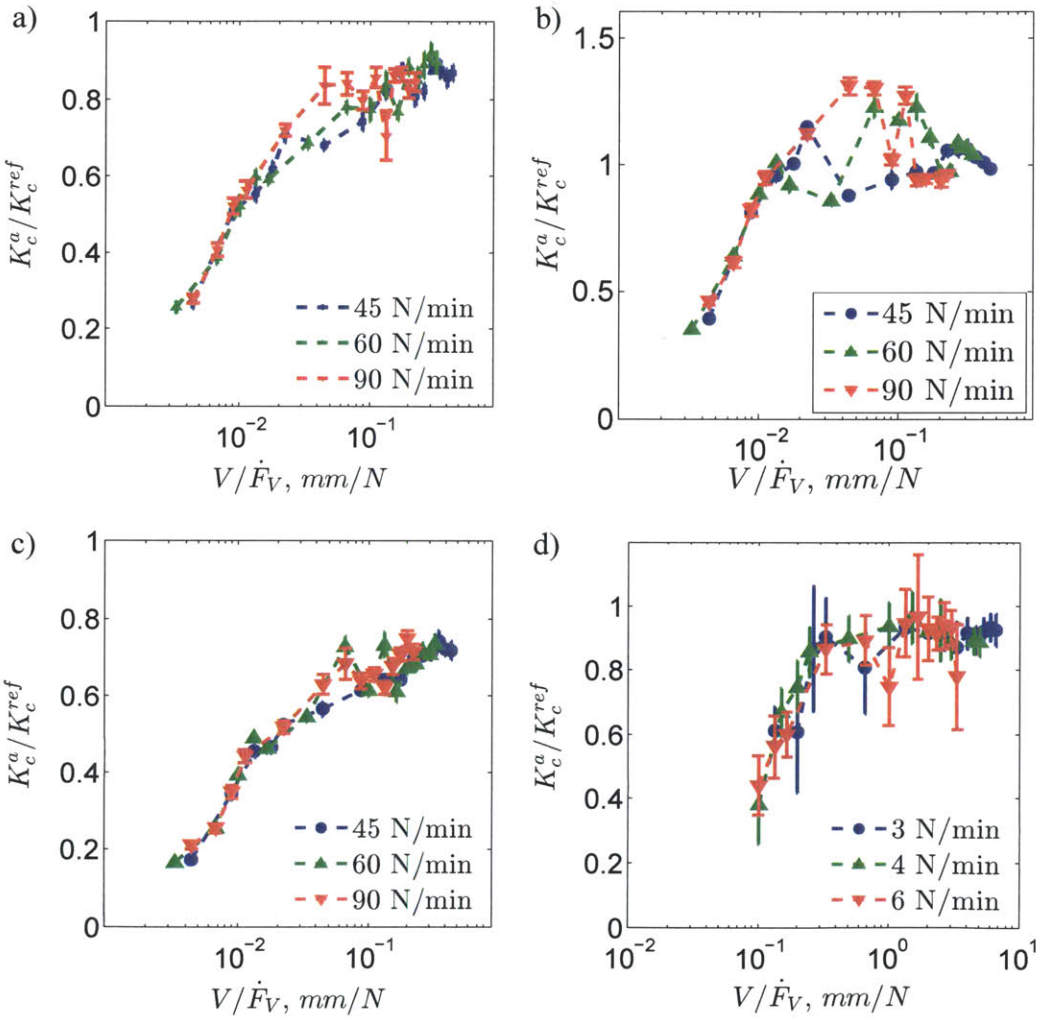

Figure 7-2: Apparent fracture toughness K_c^{a} versus scratching-speed-to-loading-rate ratio $V/\dot{F}_V$. a) Delrin®. b) Polycarbonate (PC). c) PolyVinylChloride (PVC). d) Paraffin Wax Exxon Mobil.

the scratching speed V, and the scratching-speed-to-loading-rate ratio, $V/\dot{F}_V$. Herein, K_c^{ref} is a reference fracture toughness value. For Delrin®, PC and PVC, the following literature values of K_c^{ref} were considered: 2.8 MPa$\sqrt{\text{m}}$ [48], 2.2 MPa$\sqrt{\text{m}}$ [84] and 3.0 MPa$\sqrt{\text{m}}$ [72]. As for paraffin wax, three-point bending tests performed on 180×56×34 mm notched specimen at a cross-head speed of 25.4 mm/min yielded a reference fracture toughness value of 0.08±0.017 MPa$\sqrt{\text{m}}$. For tests with a constant vertical force ($\dot{F}_V$ = 0 N/min) the apparent fracture toughness slowly increases with the velocity (Figure 7-1): for Delrin®, PC and PVC there is an increase of 25% over almost two decades and it is quasi-constant for paraffin wax. For tests with a linearly increasing vertical force ($\dot{F}_V > 0$), the apparent fracture toughness initially rises with the speed, followed by a decline in the rate of growth. Moreover, for small scratch speeds, $V < 1$ mm/min, the apparent fracture toughness decreases with the loading rate. Interestingly, when plotting K_c^{a}/K_c^{ref} as a function of the scratching-speed-to-loading-rate ratio, $\dot{F}_V/V$, for each material, all test results ($\dot{F}_V \neq 0$) collapse into a single curve that presents three phases: a sharp rise, a steady growth and a convergence towards an asymptotic value. This observation confirms the dimensionless relation (7.2). In the next section Linear Visco-elastic Fracture Mechanics is used to quantify and determine the intrinsic fracture toughness.

7.2 Decoupling Creep and Fracture

We here recall the result from Chapter ?? for rate-dependent scratch fracture processes:

$$\frac{F_T}{\sqrt{2pA_{LB}}} \leq K_c\mathcal{H}(t) \tag{7.3}$$

where $\mathcal{H}(t)$ is a viscoelastic correction factor that depends on the material's visco-elastic behavior. As a consequence, the determination of the visco-elastic behavior is required in order to assess the intrinsic fracture toughness. In the particular case of polymers, creep occurs as a result of micro-mechanisms such as molecular entanglements, polymer chains

stretching and relative slippage or chain-segment rotation. Generally, the different micro-mechanisms involved present different characteristic times; this is why a Generalized Maxwell model is used to attempt a more accurate representation of the plane strain visco-elastic relaxation modulus.

7.2.1 Plane Strain Relaxation Modulus

In order to measure the visco-elastic properties, micro-indentation tests were performed on Delrin®, polycarbonate, polyvinylchloride and paraffin wax Exxon Mobil. The prescribed load history was trapezoidal with a loading/unloading phase lasting 30s and a holding phase lasting 480 s. The prescribed maximum force was 100 mN for Delrin®, polycarbonate and polyvinylchloride and 10 mN for paraffin wax Exxon Mobil, resulting in a maximum penetration depth of 10μm. The contact creep compliance was evaluated from the depth variation during the holding phase according to the method developed by Vandamme *et. al.* [113, 114]. In this model, the indentation creep compliance $L(t)$ is related to the applied maximal force P_{max}, to the indentation stiffness S_0, and the change in depth $\Delta h(t)$ during the holding phase by:

$$L(t) = \frac{1}{M_0}\left(1 + \frac{S_0 \Delta h(t)}{P_{max}}\right) \tag{7.4}$$

In particular, Vandamme *et al.* [114] showed that the measured viscoelastic behavior is intrinsic to the material and independent of loading parameters such as the maximal force or the loading and unloading rate. For the tested polymers, the creep behavior, which is displayed in Figure 7-3 was found to be time-logarithmic. That is, the indentation creep compliance is related to the indentation modulus M_0, the contact creep modulus, C, and the characteristic relaxation time, τ according to:

$$L(t) = \frac{1}{M_0} + \frac{1}{4C}\ln\left(\frac{t}{\tau} + 1\right) \tag{7.5}$$

In order to estimate the visco-elastic constants, the average change in depth $\Delta h(t)$

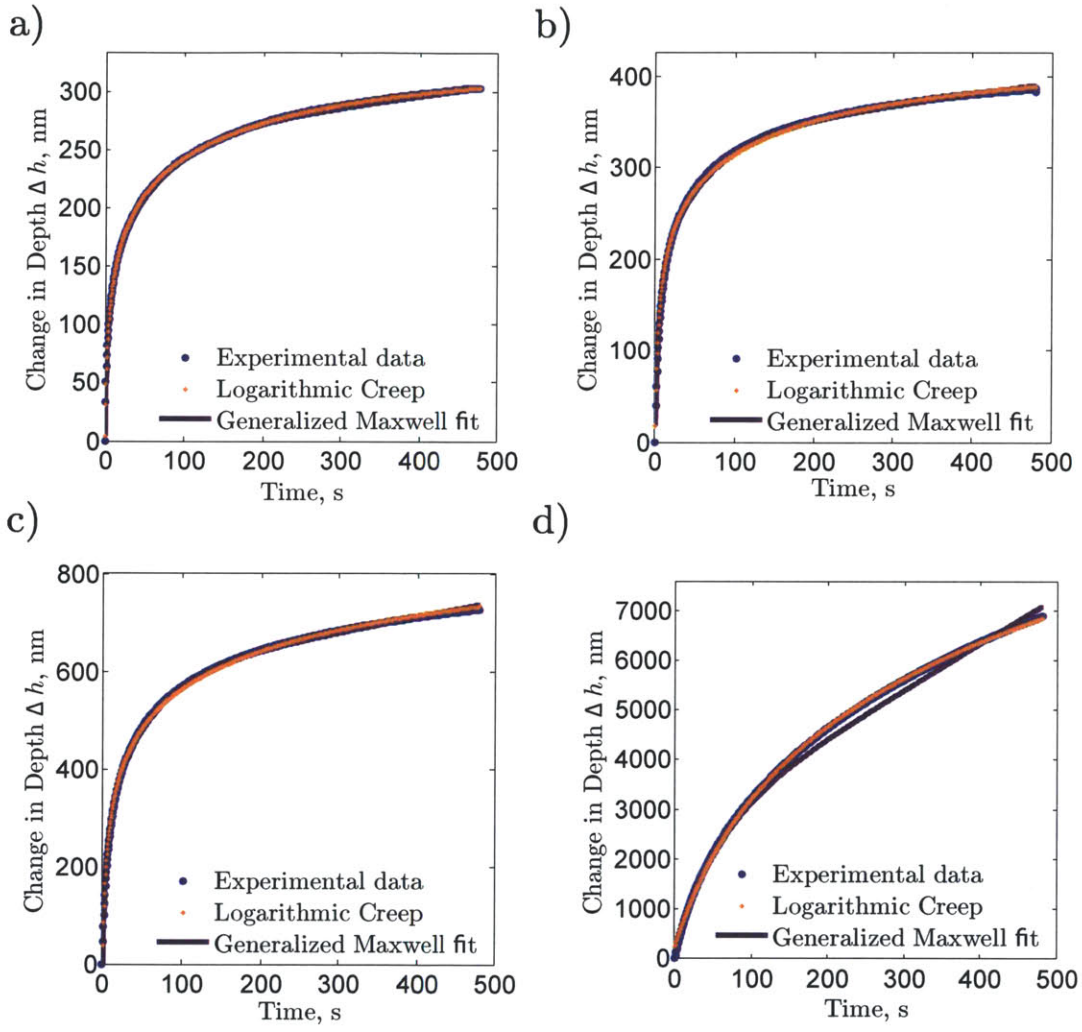

Figure 7-3: Indentation creep compliance: experimental measurement (from micro-indentation) and prediction from the Generalized Maxwell model fit. a) Delrin®. b) Polycarbonate (PC). c) PolyVinylChloride (PVC). d) Paraffin Wax Exxon Mobil.

during the holding phase was fit to a logarithmic function of the form: $\Delta h(t) = x_1 \ln(x_2 t + 1) + x_3 t + x_4$. The coefficient $x3$ represents the thermal drift of the equipment, and was found to be equal to -0.04768 nm/s. The coefficient x_4 captures the inaccuracy in determining the beginning of the creep phase; the ratio $|x_4|/\Delta h_{max}$ was equal to 1.4% for Delrin®, 4.5% for polycarbonate, 5.3% for polyvinylchloride and 3.4% for paraffin wax Exxon Mobil. Therefore x_4 is negligible and only $x1$ and x_2 relate to material properties. Finally, the characteristic time τ and the contact creep modulus C were estimated from: $\tau = 1/x_2$ and $C = P_{max}/(4S_0 x_1)M_0$. Table 7.1 displays the value of the visco-elastic constants for all four materials together with the coefficient of correlation. In particular there is a high correlation between the fit and the experimental measurement. Moreover paraffin wax Exxon Mobil presents a contact creep modulus which is two order of magnitude smaller, and a characteristic time which is two orders of magnitude greater than that of the other materials- Delrin®, polycarbonate and polyvinylchloride.

Once the indentation creep compliance is extracted, the next step is to calculate the plane strain relaxation modulus which is given in the Laplace domain by:

$$s\widehat{M}(s) = \frac{1}{s\widehat{L}(s)} \tag{7.6}$$

To this end, a numerical Laplace inversion algorithm [111] - implemented via the MATLAB function INVLAP- is used. The resulting relaxation modulus $M(t)$ is then fitted assuming a Generalized Maxwell visco-elastic behavior with a constant Poisson's ratio: $M(t) = M_0 \sum_n p_i \exp(-t/\tau_i)$. The last step is to confirm the accuracy of our prediction of the visco-elastic behavior. To this end, the method of partial fraction decomposition is used in MAPLE in order to estimate the plane strain creep function $L^1(t)$ yielded by the Generalized Maxwell model fit: $s^2\widehat{L^1(s)} = [M_0 \sum_n p_i/(s + 1/\tau_i)]^{-1}$. Figure 7-3 plots both $L(t)$ and $L^1(t)$ for all four materials, showing a good agreement between experimental data and predictions provided by the Generalized Maxwell model.

In summary, the plane strain relaxation modulus can be calculated using the following

Material	Indentation modulus $M_0(GPa)$	Contact creep modulus $C(GPa)$	Characteristic relaxation time $\tau(s)$	Correlation coefficient R^2
Delrin®	4.29	21.22	0.78	0.9999
Polycarbonate	2.95	15.16	0.59	0.9971
Polyvinylchloride	4.29	6.94	0.61	0.998
Paraffin wax Exxon Mobil	2.63	0.0158	57.21	0.9995

Table 7.1: Visco-elastic constants from micro-indentation

Material	K_c (MPa$\sqrt{\text{m}}$)	c (mm s/N)	l (mm)
Delrin®	2.72±0.06	95.27±22.74	45.80±16.87
Polycarbonate	2.85±0.11	78.56±26.10	0
Polyvinylchloride	2.96±0.07	73.30±10.48	10.31±5.04
Paraffin wax Exxon Mobil	0.078±0.0027	0.22±0.08	0

Table 7.2: Predicted intrinsic fracture toughness

two steps: the first step consists in performing micro-indentation test. The indentation creep compliance is calculated from Eq. (7.4) and fitted to a logarithmic function according to Eq. (7.6). The second step uses a numerical Laplace inversion scheme to calculate the plane strain relaxation modulus $M(t)$ for the time period considered and fits the obtained plane strain relaxation modulus to a series of decaying exponential functions.

7.2.2 Intrinsic Fracture Toughness

The visco-elastic correction factor for a generalized Maxwell model with a constant Poisson's ratio reads:

$$\mathcal{H}(t) = \left[\frac{2}{\sum_{i=0}^{n} p_i \lambda_i(t)} - \sum_{i=0}^{n} p_i \left(\frac{\lambda_i(t)}{\sum_{i=0}^{n} p_i \lambda_i(t)} \right)^2 \right]^{-\frac{1}{2}}; \quad \lambda_i = \frac{1 - e^{-\frac{t}{\tau_i}}}{\frac{t}{\tau_i}} \tag{7.7}$$

where t is the time-to-fracture that needs to be linked to rate parameters such as the loading rate $\dot{F}_V$ or the velocity V. To this end, we relate the prediction of the analytical model to the experimental observations. In particular, the analysis of the particular case

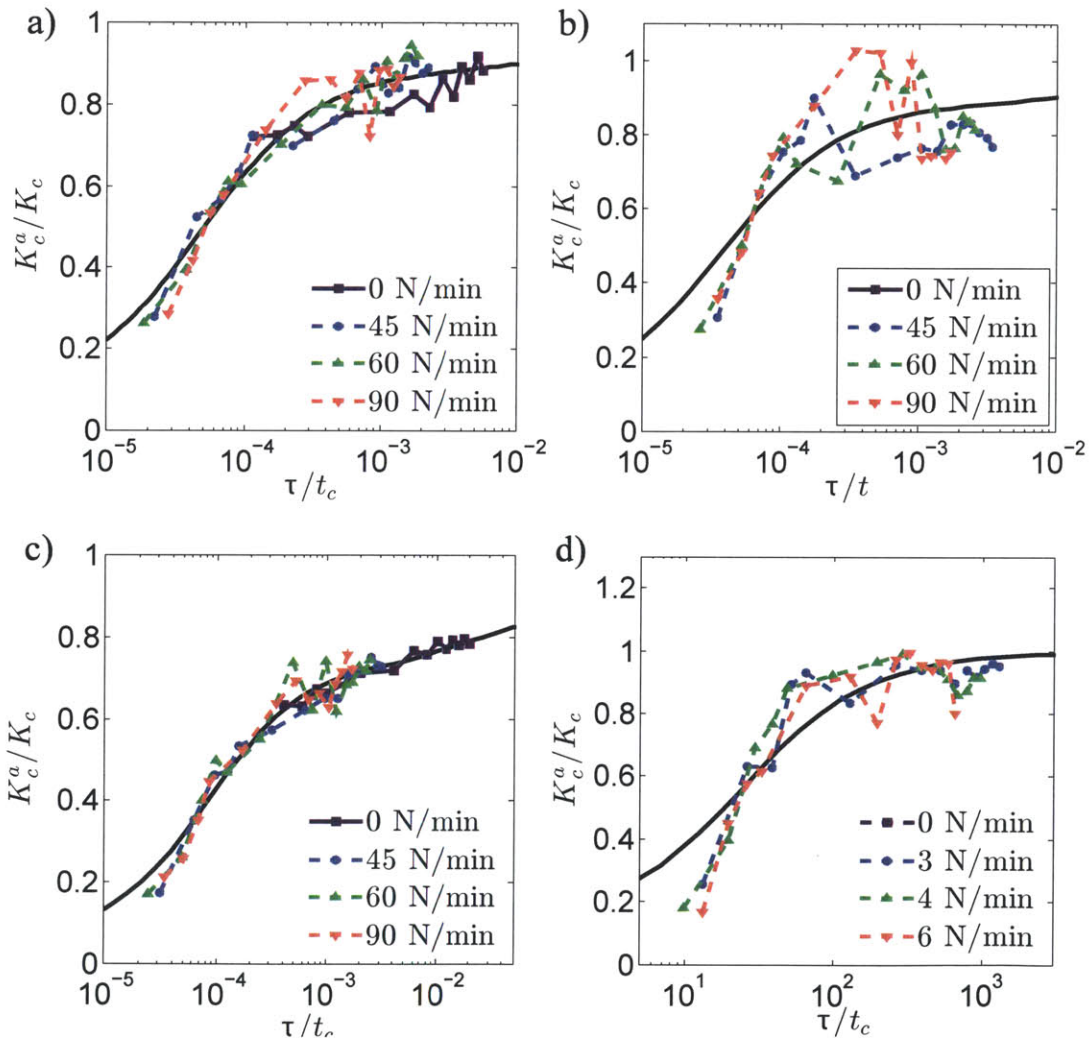

Figure 7-4: Intrinsic fracture toughness assessment: analytical model vs. experimental data. a) Delrin®. b) Polycarbonate (PC). c) PolyVinylChloride (PVC). d) Paraffin Wax Exxon Mobil.

of a Maxwell model with a constant Poisson's ratio (Section 4.5.1) has shown that the apparent fracture toughness increases with $1/t$ and then converges towards the intrinsic fracture toughness K_c for infinite values of $1/t$. On the other hand, micro-scratch test have revealed that K_c^{app} decreases with the loading rate, and increases with the scratch speed. Therefore, we postulate the existence of two material constants, c and l, that link the time-to-fracture to the scratching speed and the loading-rate-to-scratching speed ratio: $t_c = c\dot{F}_V/V + l/V$. $1/c$ has units of a surface power density, and represents the rate of surface energy dissipation that depends on the visco-elastic properties of the material; whereas l is a length-parameter introduced by the fracture process that enables us to capture the influence of the scratching speed for tests performed with a constant vertical force. Knowing the visco-elastic properties, a constrained optimization was performed using MATLAB to calculate the parameters (K_c, c, l) that minimize the sum of the squared error between the left and the right hand side of Eq. 7.2.

Table 7.2 summarizes the predicted values of K_c, c and λ for all four polymers, and Figure 7-4 confronts the prediction of the analytical with the experimental data. The overall trend is that the analytical model represents of the experimental fracture behavior fairly well. Moreover, the predicted intrinsic fracture toughness values were 2.72±0.06 MPa$\sqrt{\text{m}}$ for Delrin®, 2.85±0.11 MPa$\sqrt{\text{m}}$ for polycarbonate, 2.96±0.07 MPa$\sqrt{\text{m}}$ for polyvinylchloride, and 0.078±0.0027 MPa$\sqrt{\text{m}}$ for paraffin wax Exxon Mobil. The predicted intrinsic fracture toughness values are in the range of the literature reference fracture toughness values indicated previously: 2.8 MPa$\sqrt{\text{m}}$ [48] for Delrin®, 2.2 MPa$\sqrt{\text{m}}$ [84] for polycarbonate, 3.0 MPa$\sqrt{\text{m}}$ [72] for polyvinylchloride and 0.08±0.017 MPa$\sqrt{\text{m}}$ for paraffin wax Exxon Mobil. In other words the inverse method developed here, which combines micro-scratch and indentation tests yields predictions of the intrinsic fracture toughness at the microscopic scale that matches macroscopic measurements for homogeneous linear visco-elastic materials.

Figure 7-5 deals with the physical meaning of the parameters in our model, both c

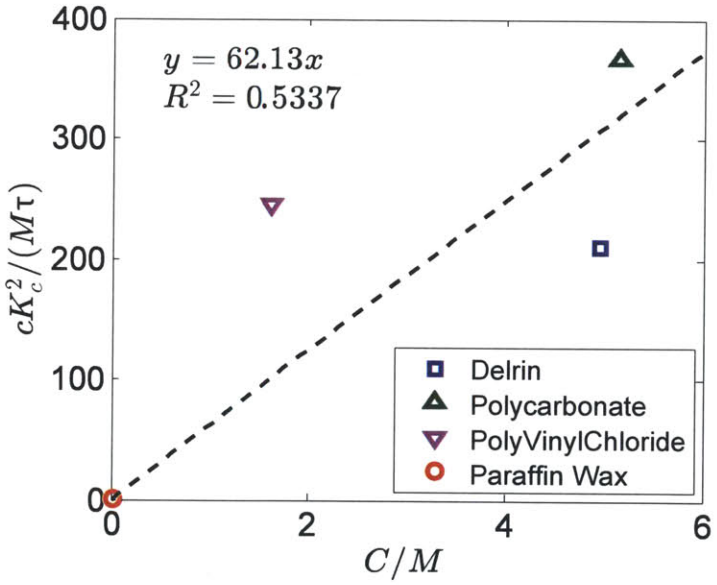

Figure 7-5: Physical meaning of the coefficient c.

and l. From dimensional analysis, we find:

$$\frac{cK_c^2}{M_0\tau} = \mathcal{F}\left(\frac{C}{M_0}\right) \tag{7.8}$$

where K_c is the intrinsic fracture toughness, M_0 is the initial plane strain relaxation modulus, τ is characteristic time of the logarithmic creep, and C is the logarithmic creep modulus. Figure 7-5 shows is a linear correlation between $cK_c^2/M_0\tau$ and C/M_0. As for the parameter l, it represents a length parameter which is activated during scratch test with a constant force. Thus we have built a comprehensive scratch model that captures the rate-dependence of fracture properties in microscopic scratch testing, over a wide range of scratch speeds, loading rates and penetration depths. In the next section, we investigate the presence of rate effects at the macroscopic scale and establish a handshake between the macroscopic and the microscopic scratch tests on homogeneous materials.

7.3 Rate Effects in Macro Scratch Tests

The goal of this section is to investigate the rate-dependence of fracture properties during macroscopic scratch tests and compare the macroscopic scratch tests results to results from microscopic scratch tests. As illustrated on Figure 7-6, in our experiments, a paraffin block (dimensions $3.4 \times 5.7 \times 22$ cm) was clamped at its lateral sides, set on a linear stage and moved at constant velocity against a vertical steel cutter-blade at depth d (measured from the block's top surface). This blade of rectangular cross section (6.35 mm thick and w wide) was held by a rigid frame that ensured a constant depth and a zero back-rake angle during the test. The values of w and d were varied such that their aspect ratio was in the range $1 \leq w/d \leq 10$, spanning an order of magnitude. For each test, the horizontal and vertical forces generated, F_T and F_V, respectively, were recorded using load cells.

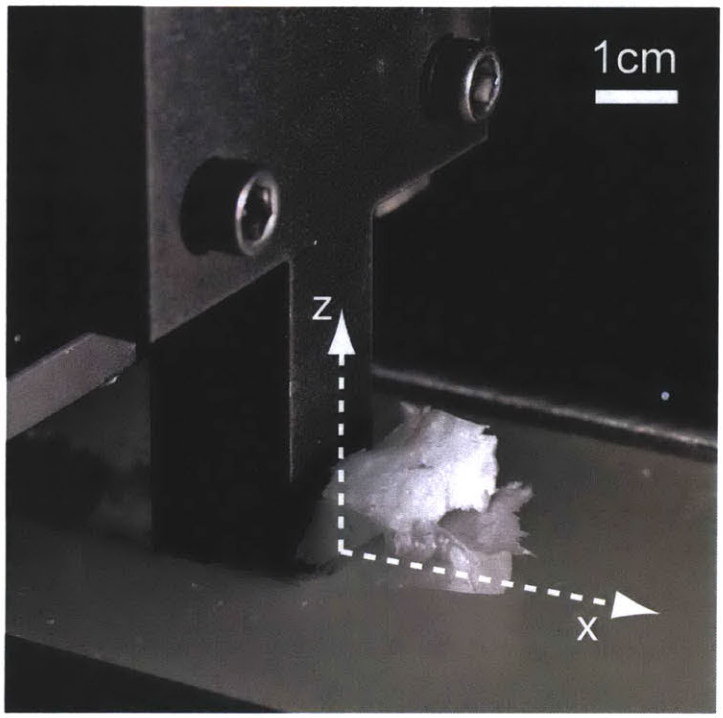

Figure 7-6: Chip formation during macro scratch tests on paraffin wax. Source [2]

7.3.1 Macro Scratch Tests Results

Previous investigation [3, 2] have shown that macro scratch tests can be used to assess the fracture toughness of materials with a blade of width w and depth d. In contrast to micro-scratch tests, where the probe is axisymmetric, for macro scratch test, it suffices, indeed, to consider $2pA_{LB} = 2wd(w + 2d)$; hence:

$$\frac{F_T}{\sqrt{2pA_{LB}}} = \frac{F_T}{w\sqrt{2d}\sqrt{1 + 2\frac{d}{w}}} \leq K_c \tag{7.9}$$

A series of macro scratch tests was performed on paraffin wax Exxon Mobil at five velocities, 0.34, 0.68, 1.7, 3.4 and 6.8 mm/s, spanning an order of magnitude. All tests were performed at a constant room temperature of 298 K. For each velocity, tests were conducted with several widths of blade ranging from 2.5 mm to 20 mm and for several depths of penetration ranging from 2.5 to 6.25 mm. Each test consisted in pushing a parallelepiped block of paraffin wax against a rigid firmly-held steel blade of given width at a given constant depth of penetration and at a given constant velocity, as depicted in Figure 7-6.

For a given velocity, the corresponding fracture toughness was calculated as the asymptotic value of the curve $F_T/(w\sqrt{2d})$ for large width-to-depth, w/d, ratios. From Eq. (7.9), for large width-to-depth ratios, the function y=f(x), where $y = F_T/(w\sqrt{2d})$ and $x = w/d$ admits a Taylor series expansion in 1/x. K_c was then estimated by fitting $F_T/(w\sqrt{2d})$ to a function of the form $y = a+b/x+c/x^2$. Figure7-7 displays the curves as well as the fitted functions for all scratch speeds. The calculated asymptotic values of the fracture toughness were 0.0837±0.0179 MPa$\sqrt{\text{m}}$, 0.0699±0.0120 MPa$\sqrt{\text{m}}$, 0.0869±0.0164 MPa$\sqrt{\text{m}}$, 0.1067±0.0169 MPa$\sqrt{\text{m}}$, and 0.114±0.0236 MPa$\sqrt{\text{m}}$, corresponding respectively to the velocities of 0.34 mm/min, 0.68 mm/min, 1.7 mm/min, 3.4 mm/min and 6.8 mm/min.

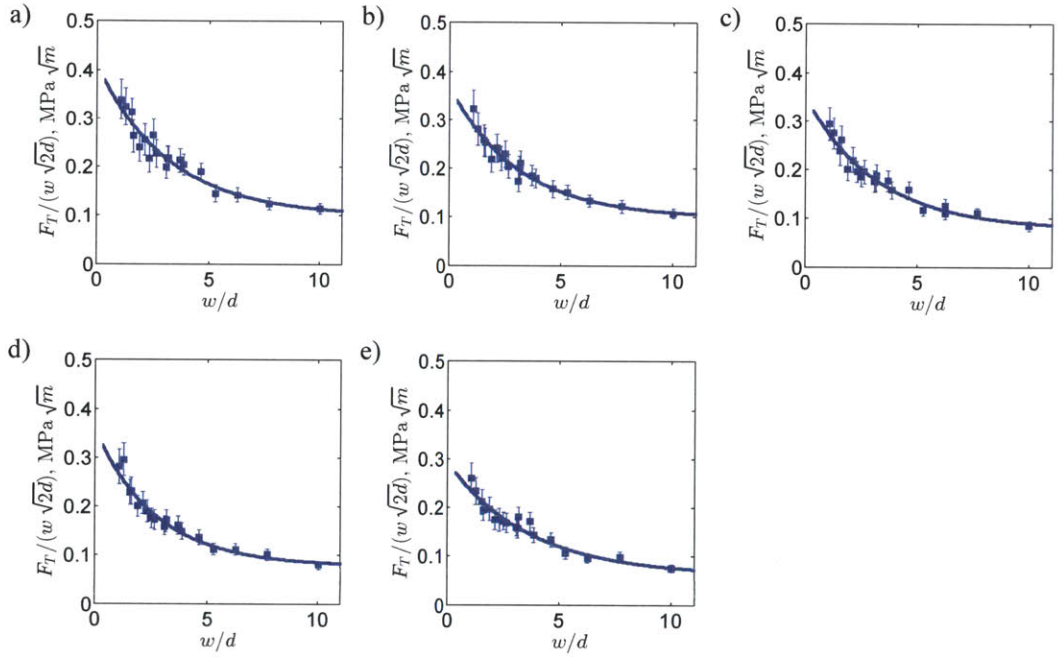

Figure 7-7: fracture scaling of macro scratch tests. Tests on paraffin wax Exxon Mobil. a) 6.8 mm/s. b) 3.4 mm/s. c) 1.7 mm/s. d) 0.68 mm/s. e) 0.34 mm/s

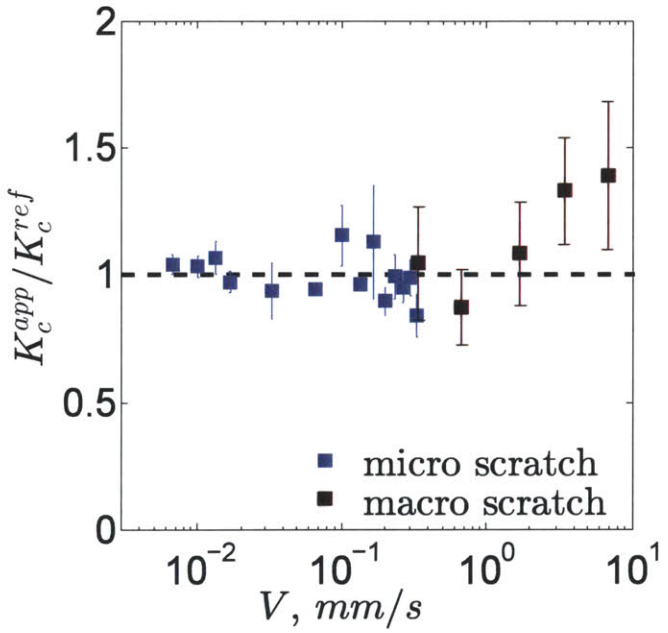

Figure 7-8: Comparison of macro scratch tests and micro scratch tests on paraffin wax Exxon Mobil.

7.3.2 Upscaling Fracture Properties: From the Microscopic to the Macroscopic scale

Our goal here is to compare the predictions from macro and micro scratch tests. Figure 7-8 displays the ratio of the apparent fracture toughness to the reference 3-point bending test fracture toughness of paraffin wax Exxon Mobil for micro scratch tests performed at constant vertical force and for macro scratch tests. In the stationary state, both micro scratch tests with constant vertical force and macro scratch tests operate under the same principle: a hard probe is scratching a soft material under a constant penetration depth, yielding a constant vertical and horizontal forces. However, there is a difference in the length-scale at which the test is performed, macroscopic for macro-scratch test and microscopic for micro-scratch tests; and from the geometry of the probe used: axisymmetric predominantly conical for micro-scratch tests, and parallelepiped for macro-scratch tests. Yet, from Figure 7-8, both configurations of testing predict that the apparent fracture toughness is independent of the scratching speed and yield close predictions for the intrinsic fracture toughness: 0.0917 ± 0.017 MPa$\sqrt{\text{m}}$ for macro scratch tests and 0.078 ± 0.0027 MPa$\sqrt{\text{m}}$ for micro scratch tests. Moreover, both values are in excellent agreement with the reference value, determined via macroscopic three-point bending tests: 0.082 ± 0.017 MPa$\sqrt{\text{m}}$. This handshake between macro-scratch tests, micro-scratch tests and conventional fracture-testing methods comprehensively validates the inverse method presented in this chapter as a way to characterize the intrinsic fracture toughness of homogeneous isotropic linear visco-elastic material. Intrinsic means that the predicted fracture toughness depends only on the material and is independent of rate-parameters, loading configurations, probe geometry, and so on.

7.4 Chapter Summary

This chapter implemented a novel experimental technique that allows separating creep from fracture, and the determination of an intrinsic, i.e. rate-independent, fracture

toughness. To this end, micro scratch tests were performed on both amorphous and semi-crystalline polymers at different loading rates and for velocities spanning two orders of magnitude. For a given loading rate, the apparent fracture toughness increased with the velocity and for strictly positive loading rates a convergence was observed towards an asymptotic value. Moreover, when the chosen x-variable is $\dot{F}_V/V$, all data points from all loading rates and velocity collapse into a master curve: the apparent fracture toughness initially rises as $\dot{F}_V/V$ increases and then converges towards an asymptotic rate-independent value.

The Linear Visco-Elastic scratch model was turned into an inverse method to predict the rate-independent fracture toughness, K_c. The visco-elastic behavior is measured via micro-indentation. The time-to-fracture is evaluated from $t = c\dot{F}_V/V + l/V$, and K_c is evaluated from:

$$\frac{F_T}{\sqrt{2pA_{LB}}} \leq K_c \mathcal{H}(t) \tag{7.10}$$

where $\mathcal{H}(t)$ is the visco-elastic correction factor that depends on the visco-elastic constants. The analytical model matches the experimental apparent fracture toughness values. Moreover, the predicted K_c agrees with measurements from conventional macroscopic fracture tests. The coefficient c which represents a rate of dissipation of surface energy, is proportional to the logarithmic creep compliance C, whereas the coefficient l captures the dependence of the scratch speed for scratch tests performed at constant penetration depth.

Macro scratch tests were also performed on paraffin wax for several velocities. The predicted apparent fracture toughness was quasi-insensitive to the scratch speeds. Moreover, the predicted K_c values were close to the prediction from micro scratch tests. Therefore, for homogeneous materials, the intrinsic fracture toughness does not depend on the loading conditions, the prescribed rate parameters, the scale of measurement or the geometry of the test.

With the method now in place, we can attempt an application to more complex ma-

terials, as encountered in many geomechanical engineering applications. Such materials exhibit a high degree of heterogeneity. An application to gas shale is developed in the next part of this thesis.

Part IV

Application to Gas Shale

Chapter 8

Fracture Characterization of Gas Shale Using Micro-Scratch Tests

In this part we attempt to characterize the fundamental fracture properties of gas shale using microscopic scratch tests. In contrast to the homogeneous isotropic elastic materials investigated in the development of the technique, gas shale is highly heterogeneous and exhibits anisotropic elastic behavior [65, 82]. Knowing the fracture properties of gas shale is of some importance, specifically in the context of hydraulic fracturing and other stimulation methods [100, 68] . Although several methods have been suggested in the scientific literature, characterizing the fracture toughness of rocks remains a challenge. For instance, the three-point bending test on single edge notched specimen [6, 93] or the semi-circular bend specimen [8, 60] require extensive machining and fatigue pre-cracking of the specimen, which makes them inappropriate for brittle materials such as gas shale. The short rod specimen and the chevron bend test, two standard methods suggested by the International Society of Rock Mechanics [97, 54, 83, 74] are often too expensive for routine applications to a large number of specimens. Moreover, the measured apparent fracture toughness depends on geometrical parameters such as the specimen diameter of the crack extension. To overcome these limitations, some criteria were introduced as well as fracture resistance curves where the fracture toughness rises with the crack extension

and then converges towards an asymptotic value [83]. Finally, other methods include the fracturing of pre-notched thick walled hollow cylinder test [120] or the punch-through shear test [9], which require laborious specimen preparation (machining, notch creation etc.), and which rely on numerical procedures instead of closed-form LEFM expressions to determine fracture properties. In contrast, the specimen preparation procedure for microscopic scratch tests is much simpler given that no pre-notch or pre-cracking is needed, and the fracture determination method relies on a closed-form Fracture Mechanics model presented in Chapters 3 and 4. Moreover, the amount of material needed is much smaller, which makes it suitable for applications where the material supply is limited. This chapter thus aims at defining a standard protocol for the fracture characterization of gas shale whereas Chapter 9 explores the relevance of scratch tests, both macro and micro, to apprehend the fracture behavior of gas shale at both the microscopic and the macroscopic scale.

In this chapter we will show that micro scratch test yields a fracture measurement which is size-independent and rate-independent. We will also show that the test is useful to gain a quantitative understanding of the fracture behavior of gas shale; and it is amendable to multi-scale characterization of the fracture resistance of gas shale. In particular, we aim at answering the following points of inquiry:

- Is the scratch test repeatable when applied to gas shale and how do we quantify the uncertainty related to the fracture toughness determination?

- What is the influence of shale anisotropy on the fracture behavior?

We will answer these questions in three steps. First, we present the materials considered in this application: EagleFord, EagleFord-SLB and Haynesville. Then, we expand on the material preparation procedure and the post-processing of scratch test results. Finally, we examine the fracture behavior of these gas shale materials.

Material	Total Organic Content (TOC)
EagleFord	2.85
EagleFord-SLB	4.31
Haynesville	3.83

Table 8.1: Material TOC data in percentage. Source [117]

8.1 Materials and Methods

8.1.1 Materials

In this study, specimens from two unconventional gas reservoirs, Eagle Ford and Haynesville, were characterized. Eagle Ford is a sedimentary formation that lies below much of South Texas in the United States. It consists of organic-rich fossiliferous marine shale. Currently Eagle Ford is the most active drilled target for shale gas in the United States. The Haynesville formation is located below large part of south western Arkansas, northwestern Louisiana and East Texas. It consists of marine and coastal plain limestone, shale, mudstone and sandstone; and it is estimated to be the largest natural gas field in the United States. All three material, EagleFord, EagleFord-SLB and Haynesville, were provided by Shell and Schlumberger. Table 8.1 lists the total organic content (TOC) of all three materials. Whereas, Table 8.2 shows their mineralogical composition, based on X-Ray diffraction tests performed by H&M Analytical Services Laboratory (35 Hutchinson Road Allentown, NJ 08501). In particular, all three materials are rich in quartz. However, both EagleFord and EagleFord-SLB have a higher content of calcite whereas Haynesville is richer in pyrite.

8.1.2 Material Preparation Procedure

The material preparation procedure developed in [77] involved three major steps: machining, grinding and polishing. During the machining step, specimens are cut along two directions, parallel and perpendicular to the bedding plane, with a diamond table saw. Afterward, a coarse grinding step is applied in order to improve the parallelism of

Mineral	EagleFord	EagleFord-SLB	Haynesville
Calcite	77.8 (3)	67.0 (3)	32.5 (2)
Illite (4.0 (2)	4.2 (1)	26.3 (4)	
Quartz	16.2 (1)	26.9 (1)	29.9 (2)
Dolomite			0.6 (1)
Pyrite	1.0 (2)	0.7 (2)	4.8 (1)
Albite	1.3 (2)		5.9 (2)
CHlorite		0.9 (2)	

Table 8.2: Mineralogy information in mass percent of the shale samples. The mineralogy data was obtained by X-ray diffraction (XRD) mineralogy test. The number in parentheses is the estimated standard deviation. Test performed by H&M Analytical Services Laboratory (35 Hutchinson Road Allentown, NJ 08501).

the top and bottom faces. This is achieved with a 240 grit Aluminum Oxide sanding paper (McMaster-Carr). The sample is then cleaned by ultrasonication in N-decane for 5 minutes. The last step involves coarse and fine polishing. The coarse polishing is carried out on 400 grit hard perforated pads (TexMet P, Buehler) with an oil-based diamond suspension in order to avoid any chemical reaction. Finally, for the fine polishing, a Fibremet®(Buehler) abrasive disc of a given size is mounted on a flat glass surface, and the surface of the specimen is gently brushed against the abrasive disc for 30 seconds to 1 minute. Four different sizes of abrasive are consecutively used: 9 μm, 3 μm, 1μm and 0.3 μm. The sample is cleansed by ultrasonication in N-decane before the fine polishing step and during the fine polishing step, between each abrasive size.

8.2 Scratch Testing of Gas Shale: Post-processing

In this section we propose a systematic way to extend the use of micro scratch test to gas shale, taking into account the high degree of heterogeneity, anisotropy and the very brittle nature of the material. First, we show evidence of fracture processes at work during the tests. Then we highlight possible sources of errors during testing. Finally, we focus on the determination of the fracture toughness addressing crucial issues such as the repeatability of the measurement or the quantification of uncertainty in the measurement.

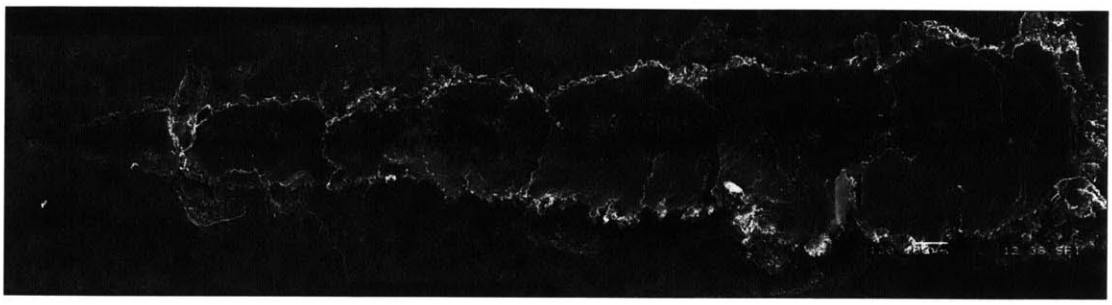

Figure 8-1: Scanning electron imaging of a residual groove after a scratch test on Eagle-Ford. (Image courtesy of Amer Deirieh.)

Scratch length (mm)	Scratch speed (mm/min)	Loading rate (N/min)	Maximum vertical force (N)
3	6	60	30

Table 8.3: Testing parameters for the scratch probe calibration.

8.2.1 Scratch Testing of Gas Shale as a Fracture-Driven Process

Figure 8-1 shows a scanning electron image performed after a scratch test on EagleFord gas shale. The testing parameters of the scratch test are described in Table 8.3 and the scratch direction is from left to right. At the beginning, the scratch groove is smooth; but as the probe advances deeper into the material, there is an increase of small and large curved cracks perpendicular to the direction of scratching. These cracks are characteristic of micro cutting and macro chipping processes occurring during the tests. Moreover, there is a pile-up of debris ahead of the plow of the scratch and along the edges of the groove. This experimental evidence points towards the prevalence of fracture dissipation during the scratch testing of gas shale: scratch tests thus appear as an appropriate technique to evaluate the fracture resistance of gas shale. However, due to the complexity of the material, additional inelastic events can occur that could invalidate the test. This will be the focus of the next section.

8.2.2 Sources of Error in the Scratch Testing of Gas Shale

Figure 8-2 shows some examples of tests that cannot be used for fracture property determination. A common cause is specimen compliance which is manifested by a sudden change in the penetration depth signal, either downwards or upwards, as illustrated in Figs. 8-2 a), b), d) and e). Another frequent cause is the saturation of the vertical force signal: the vertical force starts to decrease instead of increasing; as can be seen in Figure 8-2 c) and e). Furthermore, the presence of macro cracking can increase the relative error during the fracture toughness determination. This is usually accompanied by simultaneous sudden variations of both the penetration depth (which increases) and the horizontal force (which decreases) as evidenced in Figure8-2 f). The horizontal slope can become zero if the signal is too low as shown in Figure 8-2 g). Finally, given that the material is somewhat soft, the contact between the probe and the material can be hard to detect, which can lead to a negative initial depth of penetration, as seen in Figure 8-2 h). Thus, the first step in the post-processing of scratch test data is to examine each individual scratch test, and to discard any faulty test for further fracture property analysis. Following this inspection, we shall concentrate only on 'flawless' tests to characterize the fracture resistance.

8.2.3 Fracture Toughness Characterization of Gas Shale

As explained in Part II, a micro scratch test consists in pulling a diamond stylus across the surface of a material under a linearly increasing vertical force. The fracture toughness, K_c, is then measured from the horizontal force and penetration depth measurements according to:

$$K_c^a = \frac{F_T}{\sqrt{2pA_{LB}}} \leq K_c \tag{8.1}$$

where F_T is the horizontal force and $2pA_{LB}$ is the scratch probe area function that depends on the penetration depth, with p the perimeter of the probe and A the projected

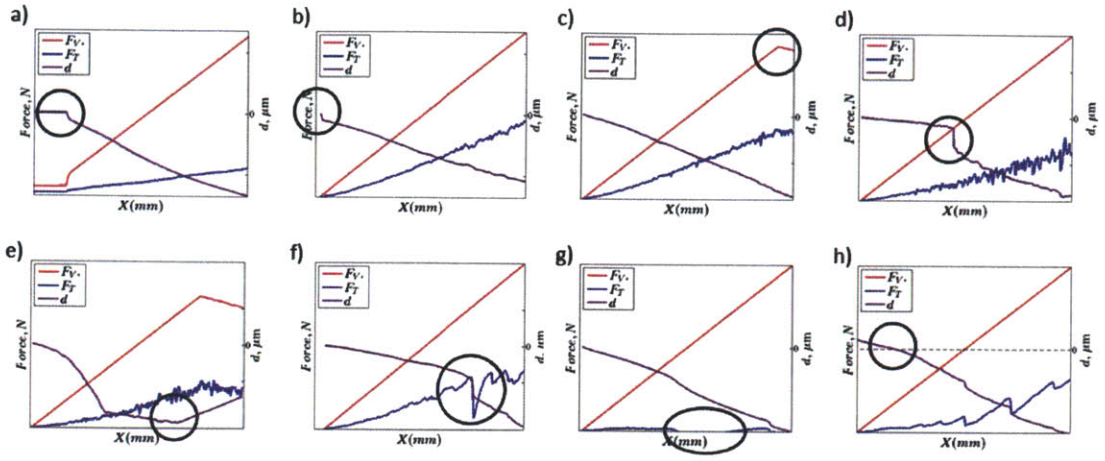

Figure 8-2: Scratch tests unsuitable for fracture property determination. A) , b), d) and e) Specimen compliance. C) vertical signal saturation. F) macro chipping. G) zero horizontal force. H) initial negative penetration depth.

contact area. This area function is calibrated prior to testing using a reference material (See Chapter 5).

Once the invalid tests are discarded, Eq. (8.1) is used to calculate the apparent fracture toughness from the remaining batch of valid scratch test. Figure 8-3 a) displays the typical horizontal force and penetration depth curve as recorded in the test: the horizontal force signal presents some saw-tooth oscillations characteristic of micro-cutting. Furthermore, as can be depicted from Figure 8-3 b), the curve $F_T/\sqrt{2pA_{LB}}$ converges, for large penetration depths, towards a constant value, which is the apparent fracture toughness of the material, as predicted by theory. For each test, the average fracture toughness and its standard deviation are calculated from:

$$\mu_{K_c} = \frac{1}{N}\sum_n \left[\frac{F_T}{\sqrt{2pA_{LB}}}\right]; \quad \sigma_{K_c} = \sqrt{\frac{1}{N}\sum_n \left[\left(\frac{F_T}{\sqrt{2pA_{LB}}} - \mu_{K_c}\right)^2\right]} \tag{8.2}$$

where the sum is performed on data points above half the maximum penetration depths.

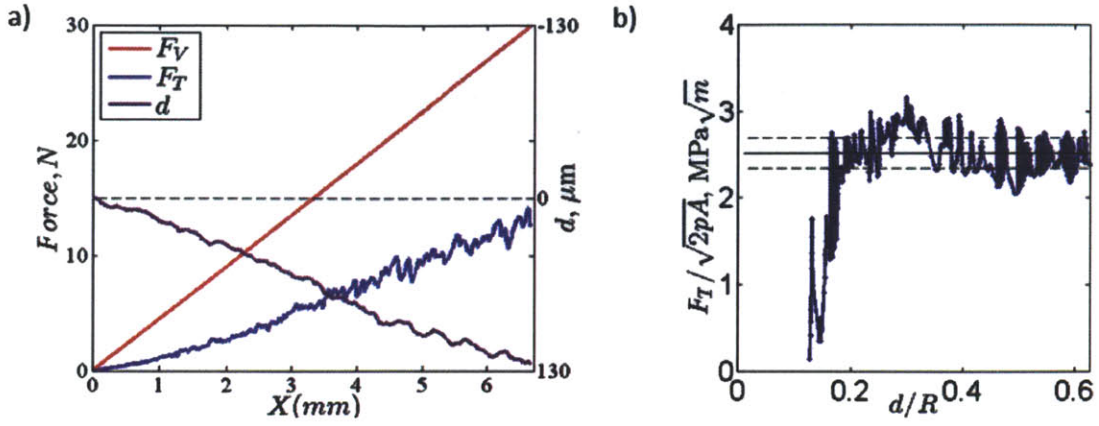

Figure 8-3: post processing of a good scratch test in shale. A) Force and penetration depth record. B) Apparent fracture toughness determination.

Usually, two or three individual scratch tests are performed.

8.2.4 Fracture Toughness Characterization of Gas Shale: Scratch Directions

Unlike polycarbonate and polyoxymethylene, gas shale is anisotropic [65]. At the sub-millimeter scale considered, the behavior can be assumed to be transversely isotropic [82]. To capture this orthotropic behavior, three scratch directions are defined as illustrated in Figure 8-4: $K_c(x31)$ is the fracture toughness when a fracture propagates perpendicular to the beddings direction. $K_c(x13)$ is the fracture toughness when a fracture crosses the bedding plane, and $K_c(x12)$ is the fracture toughness when a fracture propagates along the bedding plane. In the next sections, we will apply the micro-scratch method to study the fracture behavior of specific gas shale samples: EagleFord, EagleFord-SLB, Haynesville.

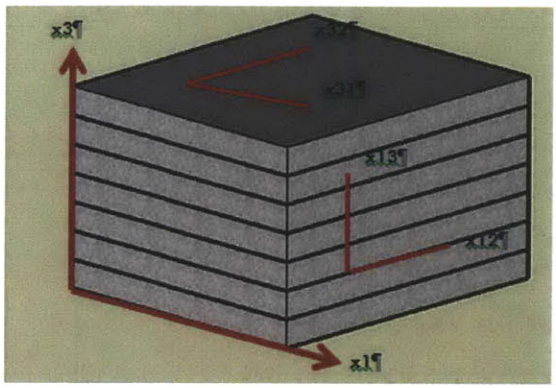

Figure 8-4: Scratch directions defined on an orthotropic material

8.3 Scratch Testing of Gas Shale: Analysis of Eagle-Ford and Haynesville Gas Shale Fracture Properties

8.3.1 Rate Dependent Fracture Response

The method presented above was applied to three gas shale materials: EagleFord, EagleFord-SLB and Haynesville provided by both Schlumberger and Shell. In order to analyze the scratch test data we here made use of the evidence shown in Chapter 6 that the probes exhibit shape functions close to a perfect cone of half-apex angle 60°. If the environmental exposure is properly handled through a proper cleansing and drying procedure as described in Chapter 5 (Section 5.1.1), there should be no statistically significant difference in the shape functions. The fact that (1) there is no significant tool wear during scratch testing and that (2) the apparent fracture toughness is independent of the scratch probe, support our assumption on the probe shape function. We also applied the filtering procedure presented above to discard abnormal scratch responses.

For the considered gas shale samples, scratch tests were performed with scratch speeds

ranging from 0.2 mm/min to 20 mm/min and with three loading rates: 45, 60 and 90 N/min; that allow us to assess the influence of rate effects on the fracture properties of gas shale[1]. For given values of the loading rate and scratch speed, a minimum of two tests was performed. Figures 8-5, 8-6, and 8-7 display the evolution of the apparent fracture toughness for all materials and for all values of scratch speed and loading rates. The measured apparent fracture toughness values range from 0.23 to 3.98 MPa$\sqrt{\text{m}}$. This upper bound is greater than twice the average fracture toughness measured on normal shale, 1.46 MPa$\sqrt{\text{m}}$, by Senseny and Pfeifle [97] using macroscopic short-rod bend specimen. The relative uncertainty of the measured apparent fracture toughness ranges from 1% to 45% with an average of 15%. In particular for EagleFord-SLB and Haynesville, high values of the relative uncertainty are associated with the directions $x13$ and $x31$; whereas the lowest values occur for the direction $x12$. These values of relative uncertainty are high compared to values obtained for homogeneous materials, (for instance 4% for polymers, see Chapter 5 Section 5.3.2); and are attributable to the heterogeneity and anisotropy of gas shale.

For a given shale, a given direction and a given loading rate, the fracture toughness increases and then reaches a plateau. In the case of EagleFord, direction $x12$, a decrease of the fracture toughness (plotted in light pink) was found for high scratch rates. This decrease of the apparent fracture toughness has not been observed in other gas shale samples. In return, the general trend of the apparent fracture toughness, rise and convergence towards an asymptotic value, has been consistently observed for all gas shale samples and scratch directions, as well as for polymers. It is a clear result of a competition between viscous bulk dissipation and crack propagation.

[1]The scratch tests were carried out by Amer Deirieh in 2012 as part of MIT's engagement in the X-Shale project enabled through MITEI/

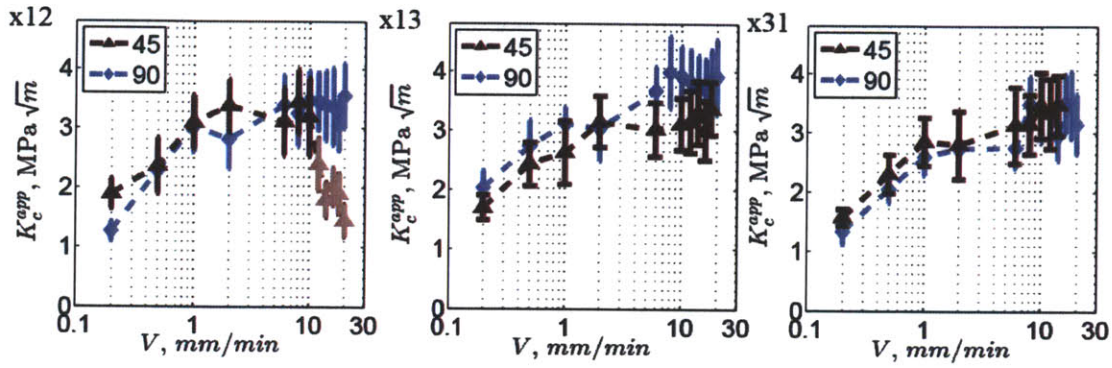

Figure 8-5: Scratch test data on EagleFord. Two loading rates: 45 N/min and 90 N/min were considered. Tests carried out by Amer Deirieh, 2012.

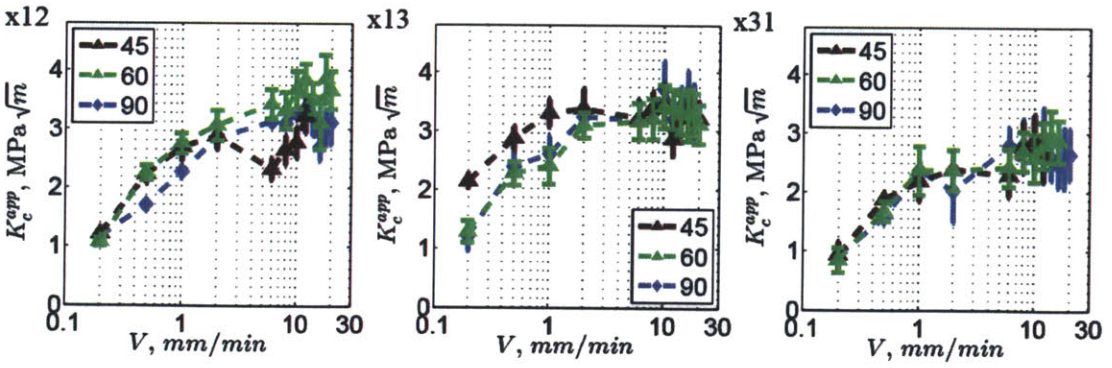

Figure 8-6: Scratch test data on EagleFord-SLB. Three loading rates: 45 N/min, 60 N/min and 90 N/min were considered. Tests carried out by Amer Deirieh, 2012.

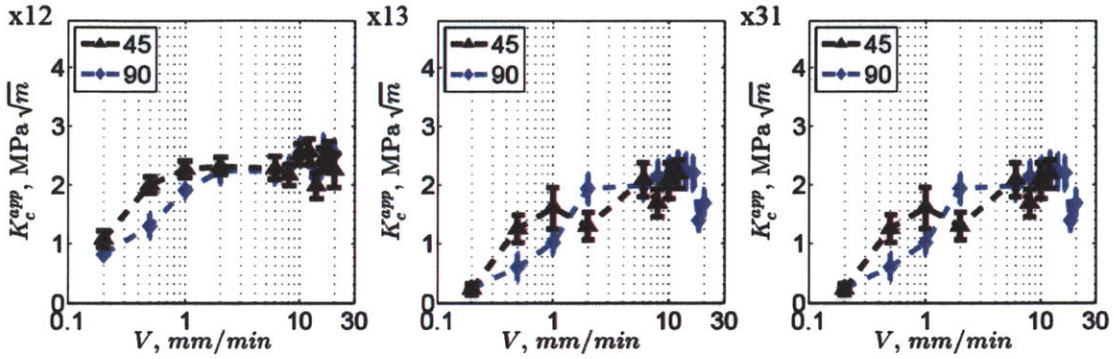

Figure 8-7: Scratch test data on Haynesville. Two loading rates: 45 N/min and 90 N/min were considered. Tests carried out by Amer Deirieh, 2012.

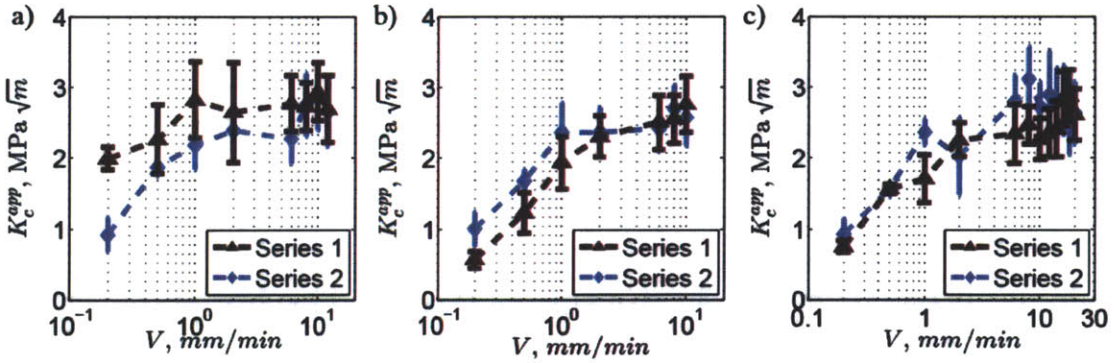

Figure 8-8: Repeatability of scratch test. EagleFord-SLB direction x31. A) 45 N/min: relative error of 10%. B) 60 N/min: relative error of 6%. C) 90 N/min: relative error of 15%. Tests carried out by Amer Deirieh, 2012.

8.3.2 Repeatability

We want to estimate the relative error introduced when testing two different specimen of the same material in the same direction and with identical scratch parameters. To this end, two specimens of EagleFord-SLB were prepared and tested in the x31 direction for scratch speeds ranging from 0.2 mm/min to 20 mm/min and for three loading rates: 45, 60 and 90 N/min. The resulting apparent fracture toughness is displayed in Figure 8-8. The two series of tests yield similar order of magnitude of the apparent fracture toughness, from 0 to 4 $\mathrm{Ma}\sqrt{\mathrm{m}}$. Moreover, from one series of tests to another, the overall trend is preserved: for a given loading rate, the apparent fracture toughness increases with the scratch speed to reach a plateau.

For a given loading rate, the relative error is calculated as the ratio of the area between the two curves and the area under the curve representing Series 2. In mathematical terms, the relative error e is given by:

$$e = \frac{\int_0^{20} |K_c^{a,1} - K_c^{a,2}|^2 dV}{\int_0^{20} K_c^{a,2} dV} \tag{8.3}$$

e was found equal to 10%, 6% and 15% for the three loading rates: 45, 60 and 90 N/min. This signifies that the scratch test results on gas shale presented here are accurate within 15%.

8.3.3 Intrinsic Fracture Toughness Determination: Maxwell Model

As shown in Chapter **??**, in the case of rate-dependent materials such as gas shale, the viscous bulk dissipation needs to be taken into account in the energy balance. As a result, the fracture propagation criterion becomes:

$$K_c^a = \frac{F_T}{\sqrt{2pA_{LB}}} \leq K_c \mathcal{H}(t) \tag{8.4}$$

where $\mathcal{H}(t)$ is a visco-elastic correction factor that depends on the material's visco-elastic behavior. For instance, for a Maxwell material with a constant Poisson's ratio, an instantaneous shear modulus G, a shear viscosity η_G and a characteristic relaxation time $\tau_G = \eta_G/G$, the visco-elastic correction factor is given by (See Chapter ?? Section 4.5.1):

$$\mathcal{H}(t) = \left[\frac{2}{\lambda(t)} - 1\right]^{-\frac{1}{2}} \tag{8.5}$$

where the plane strain visco-elastic coefficient $\lambda(t)$ is defined by:

$$\lambda(t) = \frac{\tau_G}{t}\left[1 - \exp\left(-\frac{t}{\tau_G}\right)\right] \tag{8.6}$$

As seen in Chapter 7 Section 7.2.2, the time-to-fracture t is related to the loading rate, $\dot{F}_V$, and to the scratch speed, V, via:

$$\frac{t}{\tau_G} = c\frac{\dot{F}_V}{V} + l\frac{1}{V} \tag{8.7}$$

where the coefficient c is a measure the rate of dissipation of the fracture energy, and it is proportional to the creep modulus of the scratched material. l is a length parameter activated by scratch tests performed with a constant vertical force. In particular, for scratch tests with a positive loading rate, neglecting l, Eq. (8.7) can be rewritten as: $t = \alpha\dot{F}_V/V$. Given the anisotropy nature of gas shale, the coefficient $\alpha = c\ \tau_G$ is assumed to depend on both the material and the scratch direction. A nonlinear constraint optimization procedure was thus performed in MATLAB to determine the constants K_c and α that minimize the sum of the squared error between the left hand side and the right hand side of Eq. (8.4) for all loading rates and scratch speeds relevant to the direction and the material specified.

Figures 8-9, 8-10 and 8-11 plot the apparent fracture toughness as a function of $V/\dot{F}_V$, and in black is the prediction from the analytical model. In the case of EagleFord and for the scratch direction $x12$, the tests that are in light pink and that correspond to

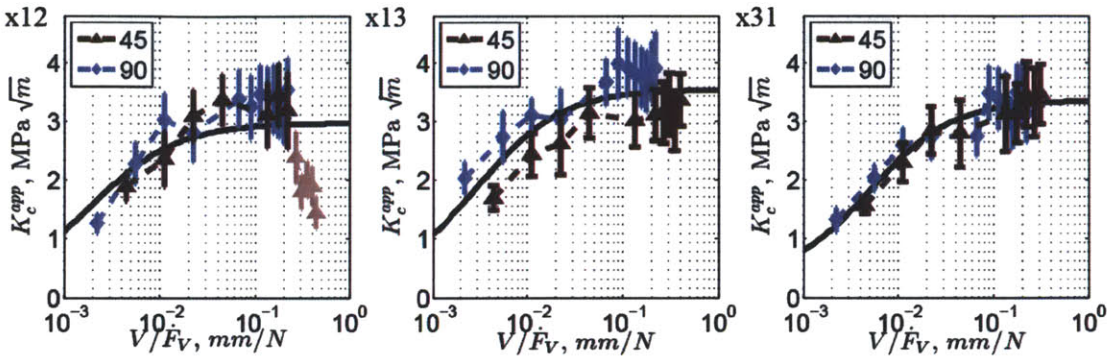

Figure 8-9: Intrinsic fracture toughness: Maxwell model. EagleFord. Tests carried out by Amer Deireih, 2012.

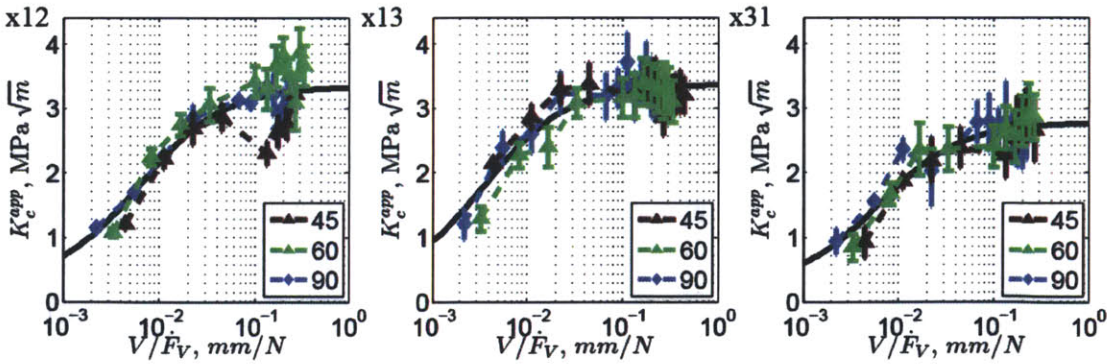

Figure 8-10: Intrinsic fracture toughness: Maxwell model. EagleFord-SLB. Tests carried out by Amer Deireih, 2012.

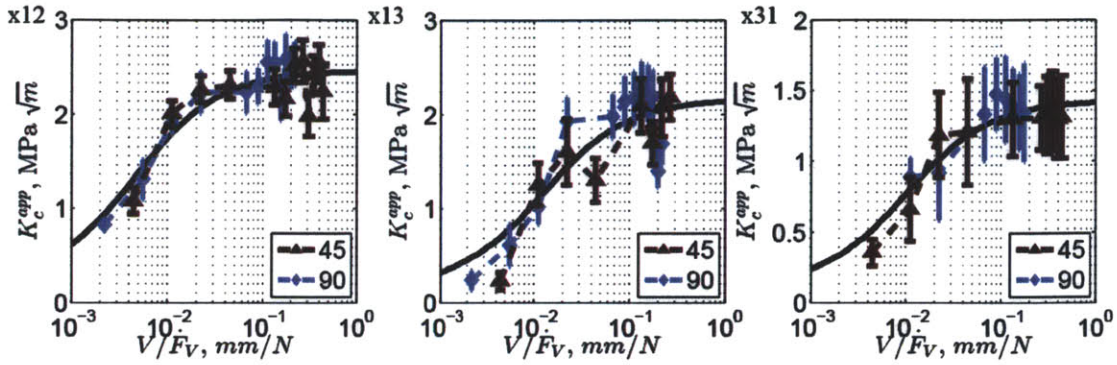

Figure 8-11: Intrinsic fracture toughness: Maxwell model. Haynesville. Tests carried out by Amer Deireih, 2012.

the unexplained decrease of the fracture toughness, were discarded from the analysis. There is an excellent agreement between the experimental data and the prediction from the analytical model. In other words, with only two constants, K_c and α, our model is able to accurately correct for rate effects. The predicted values of the intrinsic fracture toughness K_c are listed in Table 8.4 for all materials and all directions. The given standard deviations for K_c correspond to 95% confidence intervals. K_c ranges from 1.43 MPa$\sqrt{\text{m}}$ to 3.55 MPa$\sqrt{\text{m}}$, values that are much higher than the fracture toughness typically measured on shale using standard macroscopic fracture toughness testing methods. EagleFord shows no preferred scratch direction; whereas for EagleFord-SLB and Haynesville, we have: $K_c(x12) \geq K_c(x13) > K_c(x31)$. In other words, the crack is more likely to propagate when it is in the bedding plane.

EagleFord and EagleFord-SLB have close values of intrinsic fracture toughness whereas Haynesville has lower intrinsic fracture toughness values. Finally, the uncertainty on the prediction of K_c ranges from 9% to 18% with an average value of 10%. Given the high complexity of the considered materials, this low uncertainty confirms that micro scratch tests are a reliable, consistent and repeatable tool for the characterization of fracture properties of gas shale.

Material	$K_c(x12)$ MPa$\sqrt{\text{m}}$	$K_c(x13)$ MPa$\sqrt{\text{m}}$	$K_c(x31)$ MPa$\sqrt{\text{m}}$
EagleFord	2.97±0.47	3.55±0.32	3.36±18
EagleFord-SLB	3.35±0.25	3.37±0.14	2.79±0.16
Haynesville	2.47±0.15	2.17±0.38	1.43±0.12

Table 8.4: Intrinsic fracture toughness: Maxwell model. The standard deviations given correspond to 95% confidence intervals.

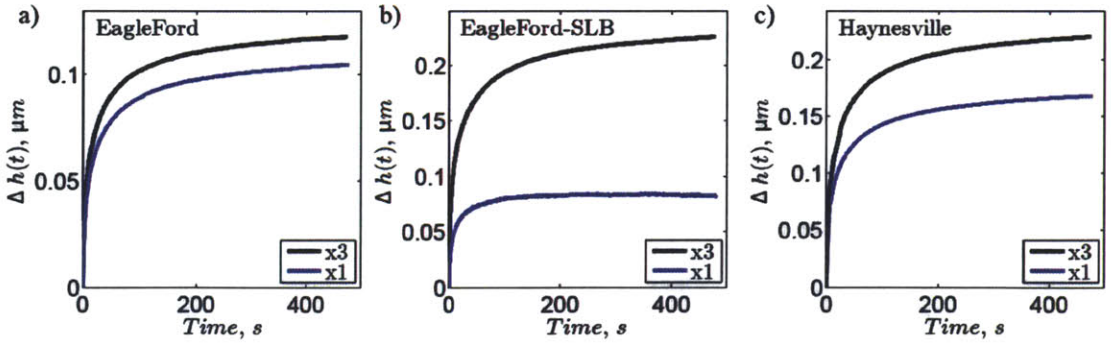

Figure 8-12: Visco-elastic behavior of gas shale: indentation compliance obtained from micro-indentation tests performed with a trapezoidal force history; the maximal force being 100 mN and the holding phase duration being 480 s and the loading/unloading step duration being 30 s. A) EagleFord. B) EagleFord-SLB. C) Haynesville.

8.3.4 Intrinsic Fracture Toughness Determination: Generalized Maxwell Model

In the previous paragraph, the intrinsic fracture toughness was determined assuming a generic Maxwell model. The inconvenient of the Maxwell model is that its simplicity may lead to overestimating the viscous dissipation since it neglects the possibility of a frozen energy inside the material. For this reason we recall the fracture criterion developed in Chapter ??, Section 4.5.4 for a generalized Maxwell model. We consider a constant Poisson's ratio constant and the following expression for the relaxation shear modulus in Laplace domain:

$$\widehat{G}(s) = \frac{G_0}{s} + \sum_{i=1}^{N} \frac{1}{\frac{s}{G_i} + \frac{1}{\eta_i}} \tag{8.8}$$

We define the functions λ_i:

$$\lambda_0 = 1; \quad \lambda_i(t) = \frac{\eta_i}{G_i t}\left[1 - \exp\left(-\frac{G_i t}{\eta_i}\right)\right] \tag{8.9}$$

Then the plane strain visco-elastic coefficient is a weighted average of the functions λ_i:

$$\lambda(t) = \sum_{i=0}^{N} \frac{G_i}{\sum_{k=0^N} G_k} \lambda_i(t) \tag{8.10}$$

Moreover, the contribution of the frozen energy to the fracture process gives rise to a frozen energy correction factor $\gamma(t)$:

$$\lambda(t) = \sum_{i=0}^{N} \frac{G_i}{\sum_{k=0^N} G_k} \frac{\lambda_i^2(t)}{\lambda^2(t)} \tag{8.11}$$

The final expression of the correction factor depends on both the plane strain visco-elastic coefficient and the energy correction factor according to:

$$\mathcal{H}(t) = \left[\frac{2}{\lambda(t)} - \gamma(t)\right]^{-\frac{1}{2}} \tag{8.12}$$

Here, we accurately measure the visco-elastic response via micro indentation tests and then use it as an input to decouple creep and fracture following the method developed in Chapter 7. Two 10x10 grids of indentations were performed on each gas shale in the transverse ($X1$) and in the longitudinal ($X3$) directions. The maximal force was 100 mN, the loading and unloading phase lasted 30 s whereas the holding phase lasted 720 s. The visco-elastic behavior was assessed from the variation in depth during the holding phase according to the model developed by [112, 113, 114]. Figure 8-12 displays the average depth variation during the holding phase for both directions, X1 and X3, and for all three materials. As can be seen, the visco-elastic behavior is anisotropic and direction X3, perpendicular to the bedding plane, is the most compliant, leading to higher values of the penetration depth. For all materials and all directions, the creep was found to be logarithmic. Table 8.5 lists the visco-elastic constants: the indentation modulus M_0, the contact creep modulus, C, and the characteristic relaxation time, τ. The visco-elastic coefficients for both directions $X1$ and $X3$ are very close for EagleFord, whereas the anisotropy is more pronounced for EagleFord-SLB and Haynesville.

Knowing the time evolution of the plane strain creep modulus, a numerical Laplace inversion scheme [111] was used to derive the plane strain relaxation modulus according to Eq. (8.8), assuming a constant Poisson's ratio. Again, neglecting the parameter l in Eq.

The comparison of the analytical model with experimental data shown in Figures 8-13, 8-14 and 8-15 show a fair amount of consistency, and foremost the high predictive capabilities of the approach to separate creep from fracture. Table 8.6 summarizes the calculated values of the intrinsic fracture toughness using the Generalized Maxwell model

Material	Indentation modulus $M_0(GPa)$	Contact creep modulus $C(GPa)$	Characteristic relaxation time $\tau(s)$	Correlation coefficient R^2
EagleFord				
$X1$	66.71±14.24	178.79±31.95	0.55	0.9992
$X3$	63.55±16.56	152.69±26.04	0.45	0.9984
EagleFord-SLB				
$X1$	73.05±1.47	212.38±4.26	0.16	0.9904
$X3$	19.71±4.41	36.80±7.31	0.50	0.9991
Haynesville				
$X1$	34.03±5.95	71.40±18.83	0.43	0.9995
$X3$	20.93±8.68	41.90±31.11	0.64	0.9986

Table 8.5: Viscoelastic constants of gas shale samples from micro indentation

Material	$K_c(x12)$ MPa$\sqrt{\text{m}}$	$K_c(x13)$ MPa$\sqrt{\text{m}}$	$K_c(x31)$ MPa$\sqrt{\text{m}}$
EagleFord	2.98±0.48	3.57±0.33	3.39±19
EagleFord-SLB	3.43±0.27	3.39±0.14	2.86±0.18
Haynesville	2.48±0.15	2.17±0.40	1.44±0.13

Table 8.6: Intrinsic fracture toughness: Maxwell Generalized model. The standard deviations given correspond to 95% confidence intervals.

by combining scratching and indentation. These values are essentially identical with the values presented in Table 8.4 determined with a simple Maxwell model for the visco-elastic behavior. Therefore the previous observations hold.

It is interesting to note the agreement between micro-indentation and micro-scratching. In particular, for EagleFord, micro-scratch tests show that there is no preferred direction and the fracture resistance is basically the same in all directions, $x12$, $x13$ and $x13$. In the same line, indentation show that the visco-elastic constants in both directions, $X1$ and $X3$ are very close, meaning that the visco-elastic behavior is almost independent of the direction. In the same way, micro-scratch tests reveal that the weakest cracks are those lying in the bedding plane for EagleFord-SLB and Haynesville; and micro-indentation exhibits the highest compliance for tests performed perpendicular to the bedding plane.

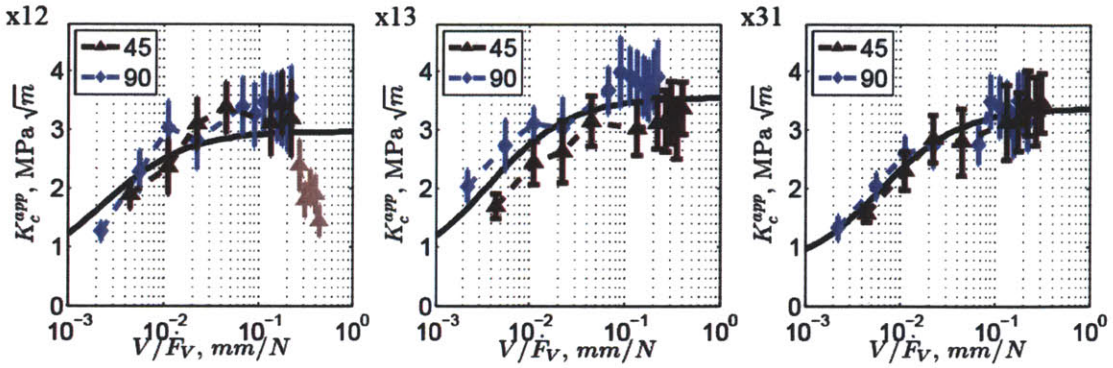

Figure 8-13: Intrinsic fracture toughness: Generalized Maxwell model. EagleFord shale. Tests carried out by Amer Deirieh, 2012.

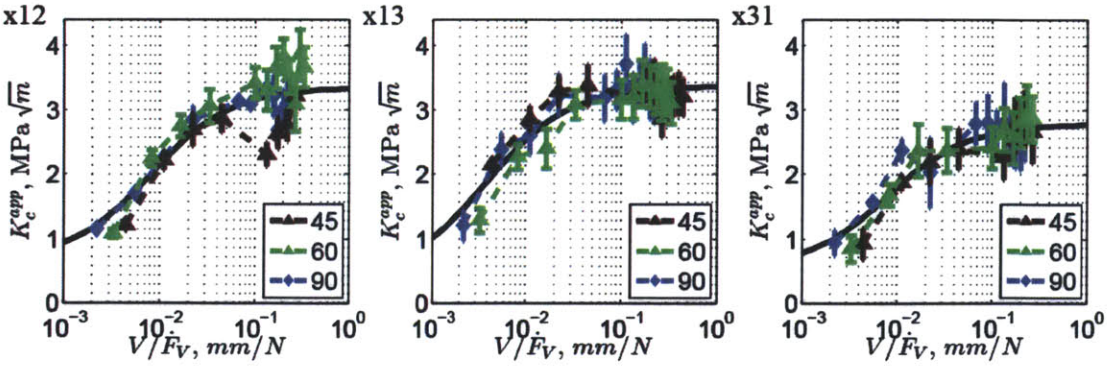

Figure 8-14: Intrinsic fracture toughness: Generalized Maxwell model: EagleFord-SLB shale. Tests carried out by Amer Deirieh, 2012.

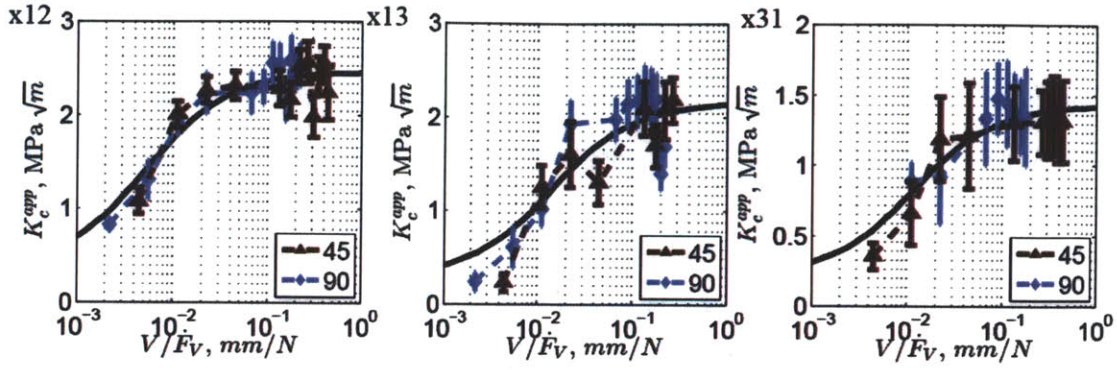

Figure 8-15: Intrinsic fracture toughness: Generalized Maxwell model: Haynesville shale. Tests carried out by Amer Deirieh, 2012.

8.4 Chapter Summary

The goal of this chapter was to implement a systematic, rigorous, accurate, precise and robust way to characterize the fracture resistance of gas shale using micro-scratch tests with a Rockwell diamond probe based on the method developed in Part II for homogeneous materials.

After reviewing evidence of fracture processes at work during the scratch testing of gas shale, a clear recipe was given to process scratch test results on gas shale. This recipe involves discarding flawed tests, analyzing the forces and penetration depths record of the remaining valid tests and quantifying the uncertainty of the measured apparent fracture toughness. In particular, scratch tests have been proven to be repeatable with an average relative uncertainty of less than 15%.

Scratch tests on three gas shale samples, EagleFord, EagleFord-Shale and Haynesville, were carried out with scratch speeds ranging from 0.2 to 20 mm/min, covering two orders of magnitudes, and for three loading rates: 45, 60 and 90 N/min. Three scratch directions were considered to account for the anisotropy of the material. $K_c(x31)$ is the fracture toughness when a fracture propagates perpendicular to the beddings direction; $Kc(x13)$ is the fracture toughness when a fracture crosses the bedding planes, and $K_c(x12)$ is the

fracture toughness when a fracture propagates along the bedding planes. For a given material, a given direction and loading rate, the apparent fracture toughness increases until a plateau is reached. The two methods described in Chapter 7 were applied to calculate the rate-independent fracture toughness values. In particular one method assumes a generic Maxwell visco-elastic behavior whereas the other measures the visco-elastic response via independent micro-indentation tests. For the gas shale materials considered in this study, the agreement between both methods was excellent, as well as the fit between the experimental data and the predictions of the experimental model. Except for EagleFord exhibiting an isotropic fracture behavior, reminiscent of its isotropic viscoelastic behavior assessed by micro indentation testing, the fracture behavior of EagleFord-SLB and Haynesville was anisotropic with $K_c(x12) \geq K_c(x13) > K_c(x31)$.

While the micro-scratch technique has thus be shown to be applicable for such highly heterogeneous materials as gas shale, it should be noted that further development are required to include the anisotropy in both the visco-elastic and fracture modeling. Nevertheless, the results presented here are encouraging to determine intrinsic fracture properties of heterogeneous materials.

Chapter 9

Multi-Scale Characterization of Shale Using Scratch Tests

The objective of this chapter is to assess the fracture resistance of shale at different length scales, using both micro scratch tests and macro scratch tests. In fact, shale can be viewed as a multi-scale composite material as shown in Figure 9-1. At nanometer length-scale, there is the elementary clay particle (level 0), that are packed at sub-micrometer length-zcale to form a porous solid (level I). At larger scales, this porous clay is mixed up with randomly distributed silt and sand inclusions (level II). With this multi-scale thought-model in mind, micro-scratching is able to test the fracture resistance of the heterogeneous composite at level II, while macro-scratching assesses the fracture behavior of the "homogeneous continuum", at a scale above.

The material for this study is a specimen from the Niobrara formation - Niobrara is a geological formation that underlies much of the Great Plains of the United States and Canada- that was provided by Shell. Herein, we analyze consecutively micro scratch tests and macro scratch tests to gather information about the fracture behavior.

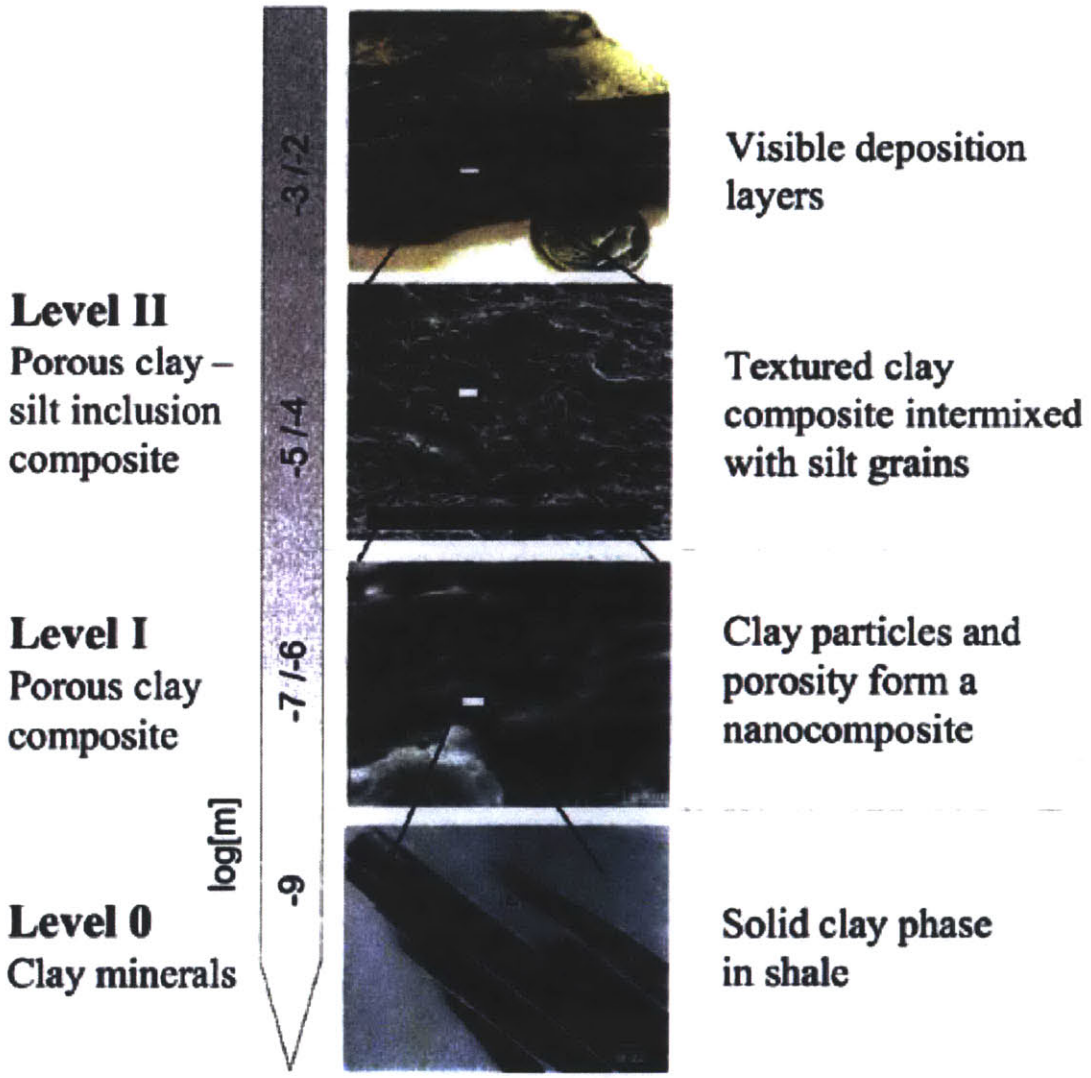

Figure 9-1: Multi-scale structure thought-model of shale. The level II and level I images come from scanning electron microscopy (SEM) imaging. The level 0 image comes from transmission electron microscopy (TEM) imaging, reprinted with the kind permission of Springer Science and Business Media. Source [81, 107, 108, 109, 82]

9.1 Micro-scratch Testing

9.1.1 Materials and Methods

From a sample of Niobrara shale, 150-mm long and 25-mm wide, two sets of two specimens, 25-mm wide and 6-mm thick, were machined using a diamond saw. The two sets correspond to the directions $X1$ and $X3$ (thickness) directions. All specimens were then prepared in several steps comprising a coarse grinding step on a 400 grit alumina oxide pad, a wet coarse polishing step with a 15 μm diamond suspension oil-based solution, a fine dry polishing step with a 9 μm alumina oxide pad, a fine dry polishing step with a 6 μm alumina oxide pad and a fine dry polishing step with a 6 μm alumina oxide pad. Between each step, the specimen were cleansed by ultrasonication for 5 minutes in N-decane.

On these four specimens, two series of micro-scratch tests were performed along the scratch direction $x31$, $x32$, $x12$ and $x13$, see Figure 9-2, for a scratch speed ranging from 0.2 mm/min to 20 mm/min and for two loading rates: 60 and 90 mm/min. Prior to testing, the scratch probe was calibrated using Lexan as described in Chapter 5 and the scratch tests were processed according to the procedure described in Section 8.2. Figure 9-2 displays the variation of the apparent fracture toughness as a function of the scratch speed for all loading rates, directions and series considered.

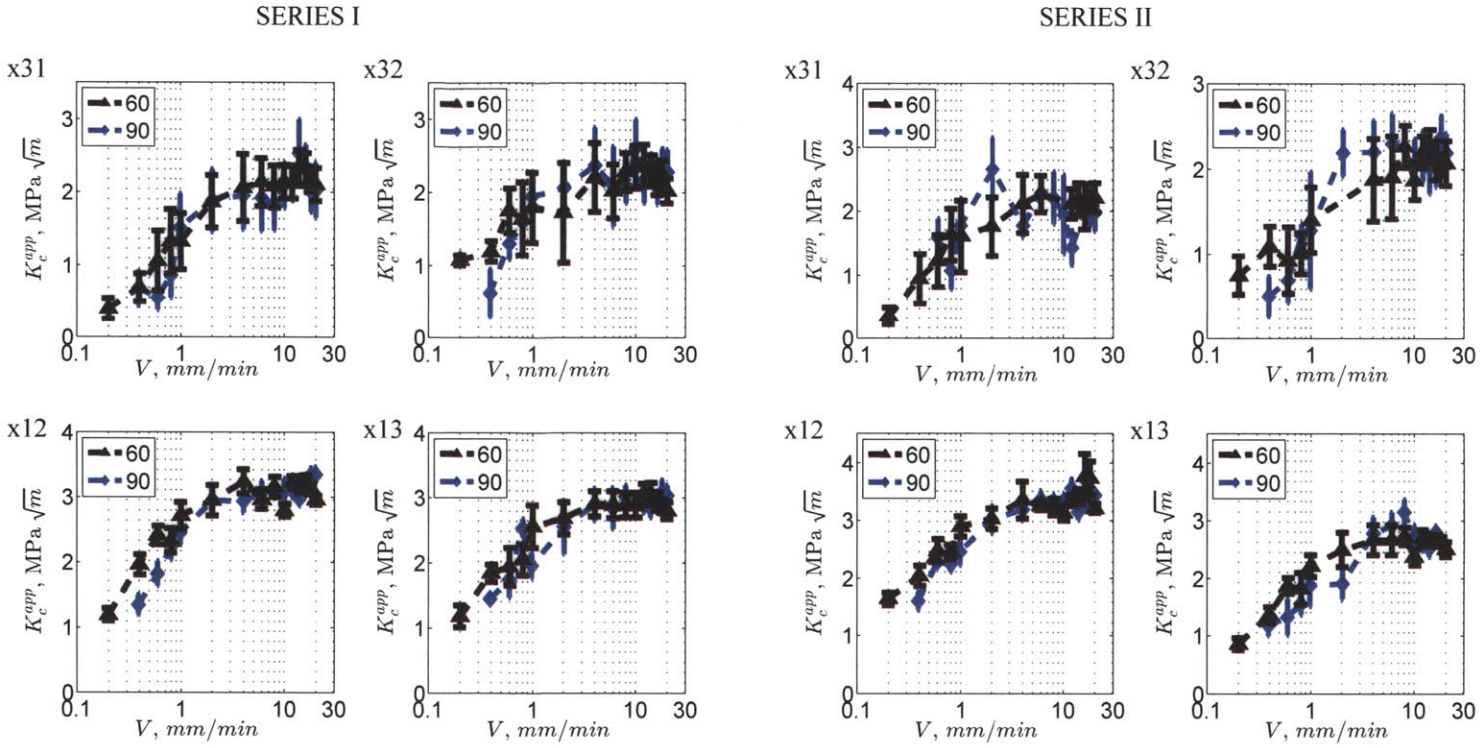

Figure 9-2: Micro-scratch tests performed on Niobrara samples with two loading rates, 60 N/min and 90 N/min, and for scratch speeds, V, ranging from 2 mm/min to 20 mm/min.

9.1.2 Results

Each data point in Figure 9-2 represents a minimum of two scratch tests performed at the same scratch speed and loading rate in the same scratch direction. The general trend found for other gas shale materials in Chapter 8 is confirmed here: for a given direction and a given loading rate, the apparent fracture toughness increases and converges towards an asymptotic value. The average relative uncertainty on the apparent fracture toughness is 20% for the scratch direction $x31$ and $x32$, and 8% for direction $x12$ and $x31$.

The analytical model developed in Section Chapter **??** is then applied to correct for rate effects and to predict the intrinsic fracture toughness values. For the sake of simplicity, the visco-elastic behavior assumed was a Maxwell model with a constant Poisson's ratio. This means that for a given scratch direction the determination of only two material constants are required in order to predict the intrinsic fracture toughness. In Chapter 7, we have shown that assuming a simple Maxwell model is as accurate as combining scratch and indentation tests. Figure 9-3 confronts the prediction of the analytical model with the experimental data, showing that the analytical model accurately reproduces the observed fracture behavior. Table 9.1 lists the values of the predicted intrinsic fracture toughness for all scratch directions and for both series. There is less than 8% of relative error between series I and series II. This is another confirmation that micro scratch tests constitute a precise tool for the measurement of the fracture resistance. Some observations made in Chapter 8 remain relevant. In particular, $K_c(x13) > K_c(x31)$: this has been observed also for EagleFord-SLB and Haynesville. Moreover, $K_c(x12) > K_c(x13)$, which has also been observed in Haynesville. These results need to be confirmed by macro scratch tests.

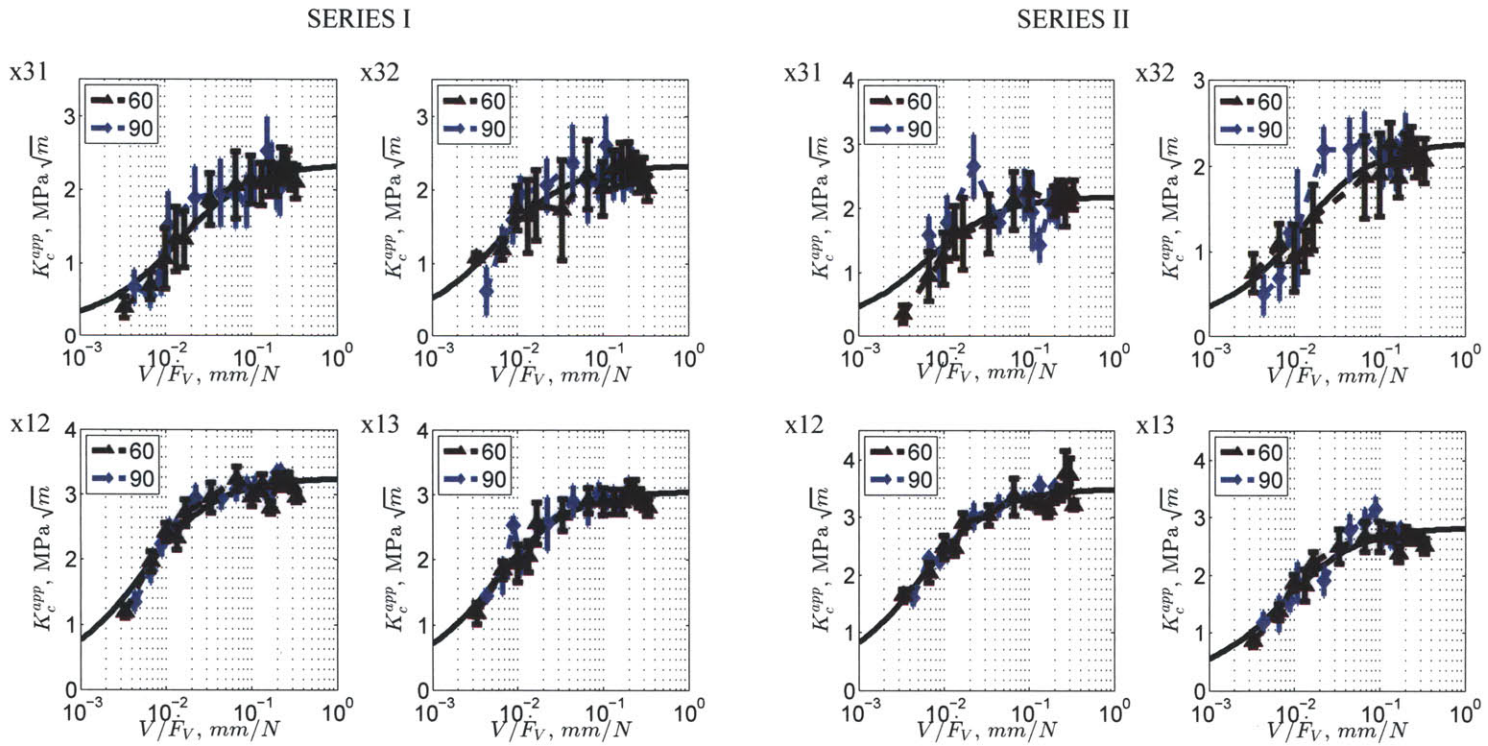

Figure 9-3: Intrinsic fracture toughness determination using a Maxwell model. Tests on Niobrara samples. Each data point represents at least two scratch tests performed at the same scratch speed and loading rate and along the same scratch direction. Two loading rates were considered: 60 N/min and 90 N/min.

Series I		Series II	
$K_c(x31)$	$K_c(x32)$	$K_c(x31)$	$K_c(x32)$
2.35±0.18	2.34±0.16	2.19±0.29	2.28±0.21
$K_c(x31)$	$K_c(x32)$	$K_c(x31)$	$K_c(x32)$
3.26±0.13	3.06±0.12	3.49±0.12	2.83±0.18

Table 9.1: Intrinsic fracture toughness in MPa$\sqrt{\text{m}}$ for Niobrara samples. The standard deviation correspond to 95% confidence intervals.

9.2 Macro-Scratch Tests

9.2.1 Macro Scratch Tests Description

Macro scratch tests were performed by TERRATEK with an inclined parallelepiped blade at a back-rake angle of $\theta = 15°$ for two scratch speeds: 6 and 180 mm/min. Figure 9-4 is a schematic representation of the test; two blade widths were considered, 5mm and 10 mm, and the penetration depth, d, varied from 0.1 mm to 0.5 mm. For a given triplet (scratch speed, blade width and penetration depth), the vertical and horizontal force, F_V and F_T were recorded. As can be seen on Figure 9-5, both the vertical and horizontal forces rise sharply as the blade comes in contact with the material, and oscillates around mean values to drop as the blade moves past the specimen. The mean vertical and horizontal forces are summarized in Tables 9.2 and 9.3 for scratching in the $X13$ and $X31$ - directions. When comparing the average force values, the values for shallow depths, ($d < 0.4$ mm) are higher in direction $X13$ than in direction $X31$. Furthermore, for a given scratch direction, blade width and penetration depth, there is a slight increase of the average horizontal and vertical forces as the scratch speed increases from 0.1 mm/s to 3 mm/s.

9.2.2 Macro Scratch Tests Analysis

A Linear Elastic Fracture Mechanics model was developed to to relate the forces and geometry of macro scratch tests to the fracture properties [3, 2]. The thought-process is similar to the approach adapted in Section 3.3.2. Assuming an horizontal crack in front

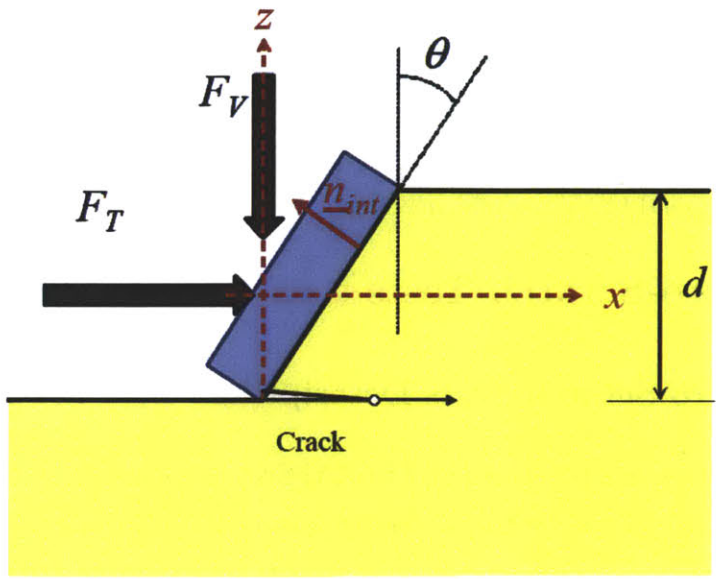

Figure 9-4: Schematic representation of a macro-scratch test.

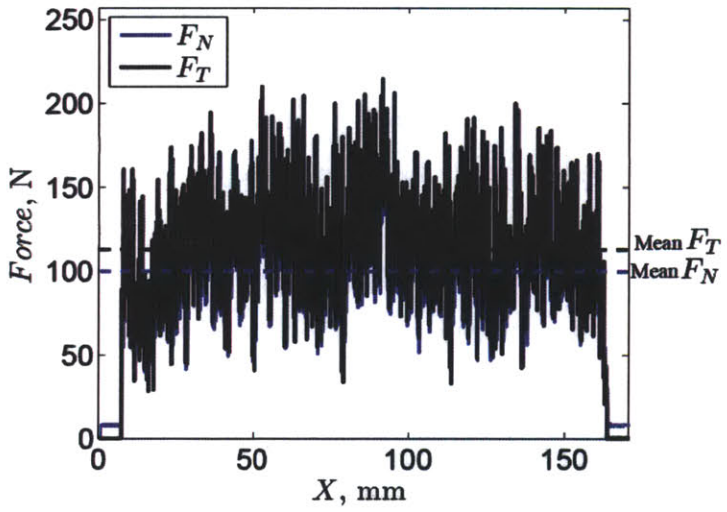

Figure 9-5: Example of scratch test result on Niobrara sample: measured vertical and normal forces along the scratch path. Width= 5 mm; depth = 0.2 mm; scratch direction=$x13$

$V(mm/s)$	$w(mm)$	$d(mm)$	$F_T(N)$	$F_V(N)$
0.1	5	0.60	445.29 ± 173.14	341.98 ± 147.80
0.1	5	0.50	306.47 ± 100.26	244.27 ± 83.18
0.1	5	0.40	211.80 ± 69.41	177.84 ± 56.25
0.1	5	0.30	152.36 ± 45.86	134.51 ± 37.73
0.1	5	0.20	110.78 ± 26.72	107.66 ± 23.80
0.1	5	0.10	64.79 ± 11.51	78.99 ± 13.52
0.1	10	0.60	549.87 ± 270.76	460.68 ± 232.11
0.1	10	0.50	430.80 ± 165.26	365.80 ± 143.41
0.1	10	0.40	315.11 ± 107.50	277.80 ± 90.43
0.1	10	0.30	233.91 ± 68.80	215.29 ± 58.74
0.1	10	0.30	223.54 ± 73.31	203.75 ± 61.19
0.1	10	0.20	175.89 ± 43.10	170.17 ± 38.24
0.1	10	0.10	120.99 ± 24.76	129.12 ± 25.22
3	5	0.20	120.27 ± 32.54	115.71 ± 28.66
3	5	0.10	72.21 ± 15.37	85.95 ± 17.14
3	10	0.20	238.38 ± 55.06	227.18 ± 50.69

Table 9.2: Macro-scratch test results on Niobrara sample. Direction $x13$.

$V(mm/s)$	$w(mm)$	$d(mm)$	$F_T(N)$	$F_V(N)$
0.1	5	0.60	168.97 ± 81.10	127.40 ± 64.59
0.1	5	0.50	161.77 ± 116.48	136.41 ± 105.88
0.1	5	0.40	101.31 ± 27.52	88.85 ± 20.14
0.1	5	0.30	79.45 ± 19.35	76.69 ± 14.86
0.1	5	0.20	57.86 ± 11.51	65.72 ± 10.26
0.1	5	0.10	34.00 ± 4.68	53.42 ± 6.76
0.1	10	0.50	187.44 ± 66.59	163.35 ± 55.67
0.1	10	0.40	165.84 ± 40.95	149.55 ± 34.84
0.1	10	0.32	152.34 ± 35.47	143.18 ± 31.27
0.1	10	0.25	127.90 ± 24.02	126.26 ± 21.49
0.1	10	0.18	104.02 ± 16.76	110.42 ± 16.50
0.1	10	0.10	79.16 ± 10.42	91.77 ± 12.20
3	5	0.20	54.03 ± 12.32	65.56 ± 12.15
3	5	0.10	38.44 ± 6.05	56.27 ± 8.45
3	10	0.20	130.74 ± 21.80	132.54 ± 20.71
3	10	0.10	90.15 ± 11.53	101.53 ± 13.20

Table 9.3: Macro-scratch test results on Niobrara sample. Direction $x31$.

of the probe as picture in Figure 9-4, the model uses an Airy function to solve for the stress and strain fields. A contour integral is then used to evaluate the energy release rate, which upon crack propagation is equal to the fracture energy of the material. The final fracture criterion reads:

$$\frac{F_{eq}}{w\sqrt{2d}} \leq K_c \tag{9.1}$$

Herein the equivalent scratch force $F_{eq} = \sqrt{F_T^2 + 3/5F_V^2}$ comprises the contribution of both the horizontal an the vertical force to the fracture process. This time the contribution of the vertical force F_V to the fracture process cannot be neglected, because the blade is inclined, with a back-rake angle of $\theta = 15°$, with respect to the vertical axis. Figures9-6 and 9-7 display the variation of the quantity $F_{eq}/(w\sqrt{2d})$ as a function of the width-to-depth ratio, w/d, for the $x13$ and $x31$ directions, respectively; and for the two scratch speeds, 0.1 mm/s and 3 mm/s. For the scratch speed 0.1 mm/s and for each direction, $F_{eq}/(w\sqrt{2d})$ decreases to converge towards an asymptotic value as the with-to-depth ratio becomes large. This convergence is characteristic of a shift from a strength-driven to a fracture-driven process.

Herein, the fracture toughness was calculated by fitting the curve F_{eq} vs. w/d to a decreasing power function of the form: $y = K_c + bx^{-n}$. The fit was performed using a nonlinear optimization algorithm in MATLAB; the fitted function is represented with dotted lines on Figures 9-6 and 9-7 and the predicted fracture toughness values at the scratch speed $V = 0.1$ mm/s are listed in Table 9.4. No prediction of the fracture toughness was performed at the scratch speed for $V = 3$ mm/s due to insufficient scratch test data.

The fracture toughness was equal to 1.10 $\pm$ 0.22 MPa$\sqrt{\text{m}}$ for direction $x13$, and 0.71 $\pm$ 0.10 for direction $x31$. These values are within the range of fracture toughness values, 0.66-1.98 MPa$\sqrt{\mu}$m, obtained by Senseny and Pfeifle (Senseny and Pfeifle, 1984) on shale with macroscopic short-rod specimen. Moreover, additional This is an additional

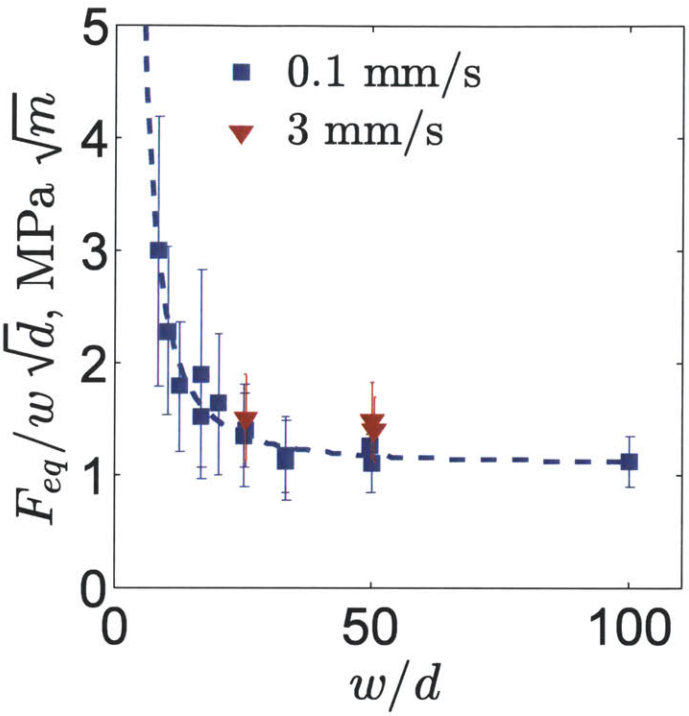

Figure 9-6: Macro-scratch test data on Niobrara sample direction x13.

confirmation of the reliability of macro-scratch tests for fracture property assessment.

The "macro" fracture behavior is anisotropic: $K_c(x13)$ is greater than $K_c(x31)$. This fact has also been observed with micro-scratch tests on the Niobrara sample but also for other gas shale materials in Chapter 8.

9.3 Chapter Summary

We postulated [2] that scratch test is a fracture-dominated process and a powerful tool that lends itself to the multi-scale characterization of fracture properties. The current

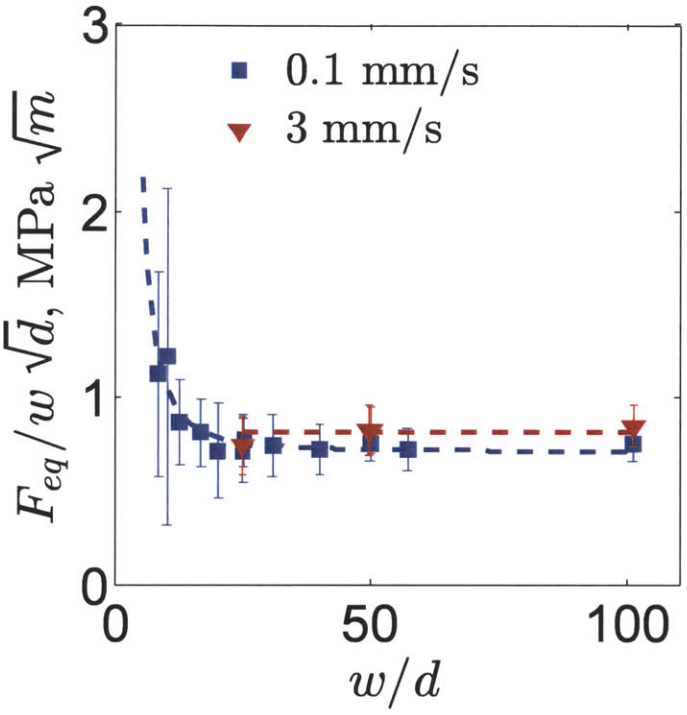

Figure 9-7: Macro-scratch test data on Niobrara sample direction x31.

$V(mm/s)$	$K_c(x13)$, MPa$\sqrt{\text{m}}$	$K_c(x31)$, MPa$\sqrt{\text{m}}$
0.1	1.10 ± 0.22	0.71 ± 0.10

Table 9.4: Macro-scratch tests results on Niobrara sample. Fracture toughness in function of scratch direction.

study confirms this statement. In fact, using the same principle (i.e., driving a hard material through a weaker material (shale)), for different geometries (rectangular inclined blade versus axisymmetric probe), at different scales (macroscopic versus microscopic), and with different loading rates, we are able to apprehend two important physical phenomena:

- Energetic size effects: due to a redistribution of stresses during crack initiation and propagation, the nominal strength depends on the nominal size of the system. In the case of Linear Elastic Fracture Mechanics, the nominal strength is inversely proportional to the square root of the nominal size of the system. This is seen in the convergence of $F_T/\sqrt{2pA_{LB}}$ for large d/R in micro scratch tests and in the convergence of $F_{eq}/(w\sqrt{d})$ for large w/d ratios in macro scratch tests.

- Increase of the fracture toughness with the scratching speed: this is due to the competition between fracture dissipation and viscous bulk dissipation. At high rates, viscous dissipation becomes negligible and the behavior is essentially elastic.

In the case of gas shale, the anisotropy of the fracture behavior is confirmed at both the microscopic and the macroscopic scale. In particular, the fracture resistance is the smallest when the crack lies in the bedding plane, $x31$; and it is the greatest when the crack is aligned with the bedding plane; while the crack opening is aligned with the bedding direction, $x12$. This can be summarized by:

$$K_c(x12) \geq K_c(x13) > K_c(x31) \tag{9.2}$$

However, there is a reduction of 60% in the fracture toughness from the microscopic scale to the macroscopic scale. This behavior was not observed for homogeneous materials (paraffin wax, see Section 7.3.2); it may be attributed to the presence of inhomogeneities and inclusions; that may explain microscopic toughening mechanism of the heterogeneous materials.

Part V

Conclusion

Chapter 10

Summary of Results and Perspectives

The main goal of this thesis was to formulate a framework to assess the fracture resistance at the microscopic scale via micro scratch tests. Thus chapter recalls what has been learned through the development of analytical models and multi-scale experiments. Based on these findings, we highlight the potential impact of this work from an academic and industrial perspective, and stress the limitations as well as potential axes for further research.

10.1 Summary of Main Findings

The main findings of this work can be classed in three categories: analytical models, experimental methods and application to gas shale.

10.1.1 Analytical Models

The rationale for Fracture Mechanics modeling was the presence of experimental clues hinting towards fracture processes at work during scratch test. As described in Chapter 2, these clues include the scaling of the scratch force as well as the presence of physical

fracture surfaces observed on the residual groove after scratch testing on metals and ceramics. Linear Elastic Fracture Mechanics was thus employed to express the scratch forces in function of the scratch probe geometry and the material fracture toughness, K_c, using an energy-based approach. The assumption of the model is that the material behavior is linear isotropic and rate-independent. Brittle fracture is considered the main mode of failure, based on the accumulation of cracks experimentally observed at large depths of penetrations on the residual groove after scratch testing. Advanced imaging of the residual groove also yielded the geometry of the generated crack surfaces: curved, horizontal and perpendicular to the direction of scratch testing. The analytical model considered thus a semi-circular horizontal crack ahead of the scratch tip. For a spherical probe, the horizontal force, F_T, scales linearly with the penetration depth; whereas for a conical probe, F_T is proportional to $d^{3/2}$. In the general axisymmetric case, F_T and K_c are linked by the equation:

$$\frac{F_T}{\sqrt{2pA_{LB}}} = K_c \tag{10.1}$$

where p is the scratch probe perimeter, A_{LB} is the projected horizontal load-bearing contact area and $2pA$ is the scratch probe function. By appropriately evaluating the scratch probe function, this framework is easily adaptable to all kinds of scratch probes used in industrial micro and macro scratch apparatus.

In the case of linear visco-elastic materials, a framework was developed to account for the viscous bulk dissipation in the energy balance. In particular, the energy release rate, that can be evaluated via a path-independent contour integral, remains the driving force of crack propagation. As a result of the visco-elastic behavior, the fracture criterion above is altered by the introduction of a visco-elastic correction factor, $\mathcal{H}(t)$, that accounts for the rate-dependence of the mechanical constants as well as the presence of a frozen energy:

$$K_c^a = \frac{F_T}{\sqrt{2pA}} = K_c\mathcal{H}(t) \tag{10.2}$$

Herein, t is the time-to-fracture that defines the onset of crack propagation. The expression of the visco-elastic correction factor, $\mathcal{H}(t)$, and of the viscous dissipation rate was developed for some classical isotropic visco-elastic models, assuming a constant Poisson's ratio and plane strain conditions. In particular, for a Maxwell model, it was shown that the ratio of the apparent to the intrinsic fracture toughness, $F_T/(K_c\sqrt{2pA_{LB}})$, increases from 0 to an asymptotic value of 1 due to the competition between viscous and fracture dissipation. Otherwise said, function $\mathcal{H}(t)$ allows separating creep and fracture in scratch tests, and the determination of the intrinsic (i.e. rate-insensitive) fracture toughness.

10.1.2 Experimental Methods

The analytical models were transformed into a series of experimental methods that aim at quantitatively measuring the fracture toughness using micro scratch tests. A rigorous experimental procedure for the calibration of the scratch probe function, $2pA_{LB}$ was introduced, for scratch tests with a Rockwell C diamond probe using Lexan 9034 as a reference material. For clean, unbroken and new (less than 150 scratch tests performed) Rockwell C probe, the calibration method yielded a shape function that depends solely on the geometry of the probe and is insensitive to external factors such as the choice of the reference material.

Using the scratch probe calibration protocol, the method for fracture determination using micro scratch tests was applied to ten materials including ceramics, metals and polymers, and for macroscopic fracture toughness values spanning almost three orders of magnitude. The scaling of the scratch force were in agreement with the prediction from the LEFM scratch model. Moreover, the quantity $F_T/\sqrt{2pA_{LB}}$ converged towards an asymptotic value for large depths of penetration, confirming the shift from a strength-dominated to a fracture-dominated process, as postulated by the analytical model. Finally the predicted values of fracture toughness were in excellent agreement with the values obtained through macroscopic conventional fracture testing methods such as the three-point bending test on single-edge notched specimens or the compact tension test.

On these homogeneous materials. the method for fracture toughness determination using microscopic scratch tests was found to be reproducible, accurate with a relative error of less than 7% and precise with a relative uncertainty of less than 10%.

Furthermore, the method for fracture determination using microscopic scratch tests was extended to rate-dependent materials. For these materials, the apparent fracture toughness, K_c^a, depends on both the scratch speed, V, and the loading rate, $\dot{F}_V$. In particular, given a loading rate, the apparent fracture toughness rises towards an asymptotic value. On the other hand, K_c^a is a decreasing function of the loading rate. These experimental observations suggest that the time-to-fracture is proportional to the loading rate and inversely proportional to the scratching speed:

$$t = c\frac{\dot{F}_V}{V} + l\frac{1}{V} \tag{10.3}$$

Thus, micro scratch testing and micro indentation were combined to decouple creep and fracture. Micro indentation is applied to measure the material visco-elastic behavior, which is then entered as input for the scratch test analysis via the correction factor $\mathcal{H}(t)$ defined by Eq. (10.2). The inverse method, which involves only three materials constant, c, l and K_c, is able to accurately reproduce the experimental fracture behavior of four polymers, Delrin, paraffin wax Exxon mobil, polycarbonate and polyvinyl chloride, for three loading rates and over a range of scratch speeds spanning two orders of magnitude. l is a length scale activated by the fracture process in scratch tests with a constant vertical force, whereas c is found to be proportional to the material creep modulus. Thus, we have a reliable inverse method for the determination of intrinsic fracture properties of rate-dependent materials using microscopic scratch tests.

10.1.3 Application to Gas Shale

In the case of gas shale, new challenges arise due to the heterogeneity, anisotropy and rate-dependence of the material. A protocol was developed to account for this complex-

ity. In particular, scratch directions are defined and a filtering procedure of the scratch test results becomes necessary. The fracture behavior is similar to the one observed on homogeneous materials. That is, the apparent fracture toughness increases with the scratch speed and decreases with the loading rate. The application of the experimental method to decouple creep and fracture yields values of the intrinsic fracture toughness that depend on the direction. In particular, a crack lying in the bedding plane is more likely to propagate than a crack normal to the bedding plane. This is expressed by the following inequality:

$$K_c(X12) \geq K_c(X13) > K_c(X31) \tag{10.4}$$

Interestingly, this inequality remains valid at the macroscopic scale. At that scale, the fracture toughness also slightly increases with the scratch speed. However, there is a reduction of 70% in the value of the fracture resistance, which could be attributed to the heterogeneous micro-structure.

10.2 Research Contribution

This work confirms the existence of an intrinsic fracture toughness, hence an intrinsic fracture energy, for homogeneous linear elastic isotropic materials. This fracture toughness is intrinsic because it is invariant with regard to the geometry of the test (parallelepiped scratch tool versus axisymmetric scratch probe), the loading conditions (linearly increasing vertical force versus constant penetration depth), the prescribed rates (loading rate and scratch speed) and the length scale of the test (macroscopic scratch test versus microscopic scratch test). This is an important development in the physics of fracture.

Another contribution is the fundamental understanding of the underlying mechanisms behind scratch tests. Despite the intensive use of scratch tests in the industry, from the introduction of the Mohs scale in 1824 [104, 21] to the development of instrumented scratch testing devices in the early 1990s [90, 91, 103, 110], the underlying mechanics

was still aloof. We postulate three modes of dissipation of the provided external work: plastic dissipation, bulk viscous dissipation and crack propagation. The plastic dissipation becomes negligible for large d/R ratios for micro scratch tests, and for large w/d ratios for macro scratch tests. As for the viscous bulk dissipation, it becomes negligible for small loading-rate-to-scratch-speed ratios, $\dot{F}_V/V$. This assumption enables us to accurately match the fracture resistance, at both the microscopic and the macroscopic scale, for different scratch probe geometries, for several loading rates and scratch speeds, and for a wide range of rate-dependent materials, including amorphous and semi-crystalline polymers, gas shale and other geologic materials.

10.3 Industrial Impact

This research work opens new venues of application of micro scratch tests. While scratch tests are relevant in several fields of science and engineering such as wear and damage of metals [1, 99, 26], thin films and coatings [85, 29, 33, 51], hardness of ceramics [41, 7] and strength characterization of rocks [90, 91, 12], this thesis introduces yet another powerful application of scratch tests as an alternative means to characterize the fracture toughness at the microscopic scale.

In the field of energy exploration and production, we present an innovative and robust method to assess the fracture properties of geological materials, which is of capital importance to address current research topics such as shale gas production or hydraulic fracturing. In the particular case of gas shale, we found an anisotropy of the fracture behavior:

$$K_c(X12) \geq K_c(X13) > K_c(X31) \tag{10.5}$$

10.4 Limitations and Future Perspectives

In this section we present the limitations of our work and identify potential axes of further research. The following points are recognized to be limitations of our work:

- Throughout this thesis work, we have considered only brittle fracture processes. Incorporating ductile fracture processes could enable one to address the case of shallow scratching, ultimately leading to a miniaturization of the technique to the nanometer scale.

- The contact area was calculated directly from the penetration depth. In particular we neglected any pile-up of material ahead of the scratch probe. This could be problematic in the case of ductile hard materials such as materials where a significant pile-up of material ahead of the probe could lead to an underestimation of the actual contact area.

- In the case of anisotropic materials such as gas shale, the anisotropic of the creep and fracture behavior is not fully accounted in the current visco-elastic scratch model

- The observed reduction in the fracture toughness values from the microscopic scale to the macroscopic scale, that seems to characterize heterogeneous materials, requires further investigation

Despite these limitations, the set of analytical models and experimental methods developed in this thesis is an important development in the field of nano-mechanics and multi-scale fracture characterization.

Bibliography

[1] T. A. Adler and R. P. Walters, Wear and Scratch Hardness of 304 Stainless Steel Investigated With a Single Scratch Test, *Wear* Vol. 162-164, pp. 713-720, (1993)

[2] A.-T. Akono, P. M. Reis, and F.-J. Ulm, Scratching as a Fracture Process: From butter to Steel, *Physical Review Letters*, Vol. 106, pp. 4302 (2011)

[3] A.-T. Akono and F.-J. Ulm, Scratch test Model for the Determination of Fracture Toughness,*Engineering Fracture Mechanics*, Vol. 78, pp. 334, (2011)

[4] L. Anand, Mechanics of Solid Materials, Lecture Notes, Massachusetts Institute of Technology, (2011)

[5] ASM Metals Reference Book, Third edition, Michael Bauccio, Ed. ASM International, Materials Park, OH, (1993)

[6] ASTM E-399 72 T, Standard Test Method for Linear-Elastic Plane-Strain Fracture Toughness KIc of Metallic Materials

[7] N. Axén, L. Kahlman, I. M. Hutchings, Correlation Between Tangential Force and Damage Mechanisms in the Scratch Testing of Ceramics, *Tribology International* Vol. 30, N0. 7,pp. 467-474, (1997)

[8] M.R. Ayatollahi, M. R. M., Aliha, On Determination of Mode II Fracture Toughness Using of Semi-Circular Bend Specimen, *International Journal of Solids and Structures*, Vol. 43, pp. 5217-5227, (2006)

[9] T. Backers, O. Stephansson, E. Rybacki, Rock Fracture Toughness Testing in Mode II-punch-through Shear Test, *International Journal of Rock Mechanics and Mining Sciences*, Vol. 39, pp. 755-769, (2002)

[10] R. Ballarini, S. P. Shah, L. M. Keer, Failure Characteristics of Short Anchor Bolts Embedded in a Brittle Material, *Proceedings of the Royal Society of London* A 404, pp. 35-54, (1985)

[11] M. Barber, J. DOnley and J.S. Langer, Steady-state Propagation of a Crack in a Viscoelastic Strip, *Physical Review A*, Vol. 40 (1),pp. 366-376 (1989)

[12] R. Bard, F.-J. Ulm, Scratch Hardness-strength Solutions for Cohesive Frictional Materials, *International Journal for Numerical and Analytical Methods in Geomechanics*, Vol. 36 (3), pp. 307-326, (2012)

[13] G. I. Barenblatt, Dimensional Analysis, Taylor & Francis US, (1987)

[14] Z. P. Bažant, S.-P. Bai, R. Gettu, Fracture of Rock: Effect of Loading Rate, *Engineering Fracture Mechanics*, VOl. 45 (5), pp. 393-398, (1993)

[15] Z. P. Bažant, R. Gettu, Rate Effects and Load Relaxation in Static Fracture of Concrete, *American Concrete Institutw*, Vol. 89 (5), pp. 456-468, (1992)

[16] Kirit J. Bhansali and Theo Z. Kattamis, Quality Evaluation of Coatings by Automatic Scratch Testing, *Wear*, Vol. 141, pp. 59-71, (1990)

[17] S. S. Bhattacharjee, P. Leger, Fracture Response of Gravity Dams due to Rise of Reservoir Elevation, *Journal of Structural Engineering*, pp. 1298-1305, (1995)

[18] Helen Lambic, Biomaterials: Mechanical Properties, ASTM International, (1994)

[19] F. P. Bowden and D. Tabor, The Friction and Lubrication of Solids, New York: Oxford University Press, (2001)

[20] W. Bradley, W. J. Cantwell, H. H. Kausch, Viscoelastic Creep Crack Growth: A Review of Fracture Mechanical Analyses, *Mechanics of Time-Dependent Materials*, Vol. 1, pp. 241-268, (1998)

[21] M. E. Broz, R. F. Cook, D. L. Whitney, Microhardness, toughness and Mohs scale minerals, *American Mineralogist*, Vol. 91, pp. 135142, (2006)

[22] Brian J. Briscoe, Paul D. Evans, Enrico Pellilo, Sujet K. Sinha, Scratching Maps for Polymers, emphWear, Vol. 200, No. 1-2, pp. 137-147, (1996)

[23] B. J. Briscoes, S. K. Biswas, S. K. Sinha, S. S. Panesar, The Scratch Hardness and Friction of a Soft Rigid-plastic Solid, *Tribology International*, Vol. 26 (3), pp. 183-193, (1993)

[24] J. . Bucaille, C. Gauthier, E. Felder and R. Schirrer, The Influence of Strain Hardening of Polymers on the Piling-up Phenomenon in Scratch Tests: Experiments and Numerical Modelling, *Wear*, Vol. 260, pp. 803-814, (2006)

[25] L. Bucaille, E. Felder, G. Hochstetter, Mechanical Analysis of the Scratch Test on Elastic and Perfectly Plastic Materials With the Three-dimensional Finite Element Modeling, *Wear*, Vol. 249, pp. 422-432,(2001)

[26] S. J. Bull, D. S. Rickerby, Multipass Scratch Testing as a Model for Abrasive Wear, *Thin Solid Films*, Vol. 18 (1-2), pp. 545-553, (1989)

[27] S. J. Bull, D. S. Rickerby, A. Matthews, A. Leyland, A. R. Pace, J. Valli, The Use of Scratch Adhesion Testing for the Determination of Interfacial Adhesion: The Importance of Frictional Drag, *Surface and Coatings Technology*, Vol. 36 (1-2), pp. 503-517, (1988)

[28] S. J. Bull, Failure Mode Maps in the Thin Film Scratch Adhesion Test, *Tribology International*, Vol. 30 No. 7, pp. 491-498, (1997)

[29] S. J. Bull, E. G. Berasetegui, An Overview of the Potential of Quantitative Coating Adhesion measurement by Scratch Testing, *Tribology International*, Vol. 39, pp. 99-114, (2006)

[30] E. E. Cabezas, D. J. Celentano, Experimental and Numerical Analysis of the Tensile Test Using Sheet Specimens, *Finite Elements in Analysis and Design*, Vol. 40, pp. 555-575, (2004)

[31] R. M. Christensen, Theory of Viscoelasticity: An Introduction, Second Edition, Academic Press, (1992)

[32] G.P. Cherepanov, Crack Propagation in Continuous Media, *Journal of Applied Mathematics and Mechanics* **31**, 467 (1967)

[33] R. Consiglio, N. X. Randall, B. Bellaton, J. V. Stebut, The Nano-scratch Tester (NST) as a New Tool for Assessing the Strength of Ultrathin Hard Coatings and the Mar Resistance of Polymer Films, *Thin Solid Films*, Vol. 332 (1-2), pp. 151-156, (1998)

[34] O. Coussy, Mechanics of Porous Continua, Wiley, (1995)

[35] http://www.csm-instruments.com/

[36] A. H. England, Complex Variable Methods in Elasticity, Dover Publications, (2003)

[37] R. Frassine and A. Pavan, An Application of Viscoelastic Fracture Criteria to Steady Crack Propagation in a Polymeric Material Under Fixed Deformation, *International Journal of Fracture*, Vol. 43, pp. 303-317, (1990)

[38] J. C. Gibbing, Dimensional Analysis, London; New York: Springer, (2011)

[39] P. Gilormini and E. Felder. Theoretical and Experimental Study of the Ploughing of a Rigid-plastic Semi-infinite Body by a Rigid Pyramidal Indenter, *Wear*, Vol. 88, No. 2, pp. 195-206,(1983)

[40] J. Gittus, Creep, Viscoelasticity and Creep Fracture in Solids, Wiley, (1975)

[41] Stephen Gonczy and N. X. Randall. An Astm Standard for Quantitative Scratch Adhesion Testing of Thin, Hard Ceramic Coatings, *International Journal of Applied Ceramic Technology*, Vol. 2, No. 5, pp. 422-428, (2005)

[42] C. G. Granqvist, Window Coatings for the Future, *Thin Solid Films*, Vol. 193-194 (2), pp. 730-741, (1990)

[43] A. A. Griffith, The Phenomena of Rupture and Flow in Solids, *Philosophical transactions of the Royal Society of London. Series A.* VOl. 43, pp.163-198, (1921)

[44] H. Guo, N. I. Aziz, L. C. Schmidt, Rock Fracture-Toughness Determination by the Brazilian Test, *Engineering Geology*, Vol. 33, 177-188, (1993)

[45] Handbook of Polycarbonate Science and Technology, D. G. Legrand and J. T. Bendler, (2000)

[46] D.S. Harding, W.C. Oliver, and G.M. Pharr, Cracking During Nano Indentation and Its Use in The Measurement of Fracture Toughness, *Materials Research Society Proceedings*, Vol. 356, pp. 663 (1994)

[47] Per Hedenqvist and Sture Hogmark, Experiences from Scratch Testing of Tribological PVD Coatings, *Tribology International*, Vol. 30, No. 7, pp. 507-516, (1997)

[48] R. W. Hertzberg, M. D. Skibo and J. A. Manson, Fatigue Crack Propagation in Polyacetal, *Journal of Materials Science*, Vol. 13 (5), pp.1038-1044, (1978)

[49] J. Hill, C. Agrawal, Positron Lifetime Spectroscopy Characterization of Thermal History Effects on Polycarbonate, *Journal of Materials Science*, Vol. 25, pp. 5036, (1990)

[50] James D. Holbery, Richard Consiglio, Characterization of Thin Film Adhesion with the Nano-Scratch Tester (NST), *Adhesion Measurements of Thin Films and Coatings*, Vol. 2, pp. 131-140, (2001)

[51] S. Hogmark, S. Jacobson, M. Larrsson, Design and Evaluation of Tribological Coatings, *Wear*, **246** (1-2), pp. 20-33, (2000)

[52] H. Ichimura, Y. Ishii, Effects of Indenter Radius on the Critical Load in Scratch Testing, *Surface and Coating Technology*, Vol. 165 (1), pp. 1-7, 2003

[53] G. R. Irwin, Analysis of Stresses and Strains Near the End of a Crack Traversing a Plate, *Journal of Applied Mechanics*, Vol. 24, pp. 361-364

[54] International Society for Rock Mechanics Commission on Testing Methods (ISRMCTM), Suggested Methods for Determining the Fracture Toughness of Rock,*International Journal of Rock Mechanics and Mining Sciences and Geomechanics Abstracts*, Vol. 25 (2), pp.71-96, (1988)

[55] M. N. James, C. J. Christopher, Y. Lu, E. A. Patterson, Fatigue Crack Growth and Craze-induced Crack Tip Shielding in Polycarbonate, *Polymer*, Vol. 53, pp. 1558-1570, (2012)

[56] Wataru Kanematsu, Subsurface Damage in Scratch Testing of Silicon Nitride, *Wear*, Vol. 256, pp. 100-107, (2004)

[57] B. L. Karihaloo, S. Santhikumar, Application of a Visco-elastic Tension-softening Constitutive Model to Cracked and Aging Concrete, *Construction and Building Materials*, Vol. 13, pp. 15-21, (1999)

[58] B. L. Karihaloo, Pull-out of Axisymmetric Headed anchors, *Materials and Structures*, Vol. 29, pp. 152-157, (1996)

[59] M. M. Karnowsky and W. B. Estill, Scratch Test for Measuring Adherence of Thin Films to Oxide Substrates, *The Review of Scientific Instruments*, Vol. 35, No. 10, (1964)

[60] M. D., Kuruppu, K. P. Chong, Fracture Toughness Testing of Brittle Materials Using Semi-Circular Bend (SCB) Specimen, *Engineering Fracture Mechanics*, Vol. 91, pp.133-150, (2012)

[61] W. R. Lacefield, Current Status of Ceramic Coatings for Dental Implants, *Implant Dentistry*, Vol. 7 (4), (1998)

[62] Biomaterials: Mechanical Properties, Helen Lambic, ASTM International, (1994)

[63] C. M. Landis, T. Pardoen, J. W. Hutchinson, Crack Velocity Dependent Toughness in Rate Dependent Materials, *Mechanics of Materials*, Vol. 32, pp. 663-678, (2000)

[64] S. Lafaye, C. Gauthier and R. Schirrer, Analyzing Friction and Scratch Tests Without *In Situ* Observation, *Wear*, Vol. 265, pp. 664-673, (2008)

[65] B. Lecampion, S. Abbas and R. Prioul, Competition Between Transverse and Axial Hydraulic Fractures in Horizontal Wells, *SPE* 163848, (2013)

[66] D. G. Legrand and J. T. Bendler, Handbook of Polycarbonate Science and Technology, CRC Press, (2000)

[67] A. H. Lettington, Applications of Diamond-like Carbon Thin Films, *Carbon*, Vol. 36 (5-6), pp. 555-560, (1998)

[68] T. Lhomme, E. Detournay, R. Jeffrey, Effect of Fluid Compressibility and Borehole Radius on the Propagation of a Fluid-driven Fracture, In *Proceedings of the 11th International Conference on Fracture*, Turin, Italy (2005)

[69] Z.-M. Li, Z.-Q. Qian, M.-B. Yang, W. Yang, B.-H. Xie, R. Huang, Anisotropic Microstructure-impact Fracture Behavior Relationship of Polycarbonate/Polyethylene Blends Injection-Model at Different Temperatures, *Polymer*, Vol. 46, pp. 10466-10477, (2005)

[70] L. Ma,J. Zhou, A. Lau, S. Low, R. Dewit, Self-similarity simplification Approaches for the Modeling and Analysis of Rockwell Hardness Indentation, *Journal of Research of The National Institute of Standards and Technology*, Vol. 107 (5), pp. 401-412, (2002)

[71] Z. Major and R. Lang, Rate-Dependent Fracture Toughness of Plastics, *Journal of Physics IV France*, Vol. 110, DOI: 10.1051/p4: 20030748, (2003)

[72] J. F. Mandell, A. Y. Darwish, F. J. McGarry, Effects of Processing Conditions and Aging on the Fracture Toughness of Rigid PVC Pipe Materials, *Journal of Vinyl Technology*, Vol. 4 (3), pp. 95-100, (1982)

[73] W. T. Matthews: Data handbook for metals. AMMRC MS73-6, U.S. Army Materials and Mechanics Research Center, Watertown, MA, (1973)

[74] K. Matsuki, S. S. Hasibuan, H. Takashashi, Specimen Size Requirement for Determining the Inherent Fracture Toughness of Rocks According to the ISRM Suggested Methods, *International Journal of Rock Mechanics and Mining Sciences and Geomechanics Abstracts*, Vol. 28 (5), pp. 365-374, (1991)

[75] D. Maugis, Review Subcritical Crack Growth, Surface Energy, Fracture Toughness, Stick-slip and Embrittlement, *Journal of Materials Science*, Vol. 20, pp. 3041-3073, (1985)

[76] L. N. McCartney, Crack Growth Laws for a Variety of Viscoelastic Solids using Energy and COD Fracture Criteria, *International Journal of Fracture*, Vol. 15 (1), (1979)

[77] M. Miller, C. Bobko, M. Vandamme, and F.-J. Ulm: Surface Roughness Criteria for Cement Paste Nanoindentation, *Cement and Concrete Research*, Vol. 38, 467 (2008)

[78] A. D. Mulliken, M. C. Boyce, Mechanics of the Rate-dependent Elastic-plastic Deformation of Glassy Polymers From Low to High Strain Rates, *International Journal of Solids and Structures*, Vol. 43, pp. 1331-1356, (2006)

[79] S. T. Nguyen, L. Dormieux, Y. L. Pape, J. Sanahuja, Crack Propagation in Viscoelastic Structures: Theoretical and Numerical Analyses, *Computational Materials Science*, Vol. 50, pp. 83-91, (2010)

[80] I. Nieminen, P. Andersson and K. Holmberg, Friction Measurement by Using a Scratch Test Method

[81] J. A. Ortega, F.-J. Ulm, and Y. Abousleiman, The effect of the Nanogranular Nature of Shale on Their Poroelastic Behavior, *Acta Geotechnica*, **2**(3), pp. 155-182, (2007)

[82] J. Alberto Ortega, Microporomechanical Modeling of Shale, Ph.D. Thesis, Massachusetts Institute of Technology, (2010)

[83] F. Ouchterlony, Fracture Toughness testing of Rock with Core Based Specimens, *Engineering Fracture Mechanics*, Vol. 35, pp. 351-366, (1990)

[84] M. Parvin, J. G. Williams, Ductile-brittle Fracture Transitions in Polycarbonate, *International Journal of Fracture*, Vol. 11 (6), pp. 963-972, (1975)

[85] A. J. Perry, Scratch Adhesion Testing of Hard Coatings, *Thin Solid Films*, Vol. 107 (2), pp. 167-180, (1983)

[86] Polymer Data Handbook, Oxford University Press, (1999)

[87] S. V. Prasad and T. H. Kosel, A Study of Carbide Removal Mechanisms During Quartz Abrasion I: *In Situ* Scratch Test Studies, *Wear*, Vol. 922, pp. 253-268, (1983)

[88] N. X. Randall, G. Favaro, C. H. Frankel, The Effect of Intrinsic Parameters on the Critical Load as Measured with the Scratch Test Method, *Surface and Coatings Technology*, Vol. 137 (2-3), pp. 146-151, (2001)

[89] J.R. Rice, A path Independent Integral and the Approximate Analysis of Strain Concentration by Notches and Cracks, *J. Appl. Mech.* **35**, 379 (1968)

[90] T. Richard, E. Detournay, A. Drescher, P. Nicodeme, D. Fourmaintraux, The scratch test as a Means to Measure Strength of Sedimentary Rocks, *SPE/ISRM 47196*, (1998)

[91] G. Schei, E. Fjaer, E. Detournay, C. J. Kenter, G. F. Fuh, The Scratch Test: An Attractive Technique for Determining Strength and Elastic Properties of Sedimentary Rocks, *SPE 63255*, (2000)

[92] J. L. Schiff, The Laplace transform: theory and applications, New York: Springer, (1999)

[93] R. A. Schmidt, C. W. Huddle, Effect of Confining Pressure on the Fracture Toughness of Indiana Limestone, *International Journal of Rock Mechanics and Mining Sciences and Geomechanics Abstracts*, Vol. 14, pp.289-293, (1977)

[94] R. A. Schmidth, A Microcrack Model and its Significance to Hydraulic Fracturing and Fracture Toughness Testing, Sandia National Laboratories, Albuquerque, NM 87185, (1980)

[95] C. G. Scott and S. Danyluk, Examination of Silicon Wear Debris Generated in a Linear Scratch Test, *Wear*, Vol. 152, pp. 183-185, (1992)

[96] J. Sekler, P. A. Steinmann, H. E. Hintermann, The scratch Test: Different Critical Load Determination Techniques, *Surface and Coatings Technology*, Vol. 36 (1-2), pp. 519-529, (1988)

[97] P. E. Senseny, T. W. Pfeifle, Fracture Toughness of Sandstone and Shales, American Rock Mechanics Association, (1984)

[98] C. Seubert, K. Nietering, M. Nichols, R. Wykoff and S. Bolling, An Overview of the Scratch Resistance of Automotive Coatings: Exterior Clearcoats and Polycarbonate Hardcoats, *Coatings*, Vol. 2, pp. 221-234, (2012)

[99] H. R. Shetty, T. H. Khosel and N. F. Fiore, A Study of Abrasive Wear Mechanisms Using Diamond and Alumina Scratch Tests, *Wear*, Vol. 80, pp. 347-376, (1982)

[100] J. Shlyapobersky, Energy Analysis of Hydraulic Fracturing, 26^{th} US Symposium on Rock Mechanics, (1985)

[101] I. N. Sneddon, S. Ulam, The Theory of Linear Viscoelasticity, International Series of Monographs on Pure and Applied Mathematics, Vol. 10, (1960)

[102] http://help.solidworks.com/2012/English/SolidWorks/cworks/Generalized_Maxwell_Model.htm

[103] P. A. Steinmann, Y. Tardy, H. E. Hintermann, Adhesion Testing by the Scratch Test Method: The Influence of Intrinsic and Extrinsic Parameters on the Critical Load, *Thin Solid Films*, Vol. 154 (1-2), pp. 333-349, (1987)

[104] D. Tabor, Mohss Hardness Scale-A Physical Interpretation. *Proceedings of the Physical Society*, Vol. 67, pp. 249, (1954)

[105] S. Tang, T. F. Guo, L. Cheng, Rate effects on Toughness in Elastic Nonlinear Viscous Solids, *Journal of the Mechanics and Viscous Solids*, Vol. 56, pp. 974-992 (2008)

[106] Franz-Josef Ulm Micromechanics and Durability of Solids, Lecture Notes, Massachusetts Institute of Technology, 2012.

[107] F.-J. Ulm, and Y. Abousleiman, The Nanogranular Nature of Shale, *Acta Geotechnica*, **1**(2), pp. 77-88, (2006)

[108] F.-J. Ulm, A. Delafargue, and G. Constantinides,Experimental microporomechanics, In: Applied Micromechanics of Porous Materials, L. Dormieux and F.-J. Ulm, eds., Springer, Wien, 207-288, (2005)

[109] F.-J. Ulm, G. Constantinides, A. Delafargue, R. Ewy, L. Duranti, and D. K. McCarty, Material Invariant Poromechanics Properties of Shales, In: Poromechanics III. Biot Centennial (1905-2005), Y. Abousleiman, A. H.-D. Cheng, and F.-J. Ulm, eds., A. A. Balkema Publishers, Norman, OK, 627-644, (2005)

[110] Juhani Valli and Ulla Mäkelä, Applications of the Scratch Test Method for Coating Adhesion Assessment, *Wear*, Vol. 115, pp. 215-221, (1987)

[111] J. Valsa and L. Brancik, A Fast Computing Method of Numerical Inversion of Two-dimensional Laplace transforms using FFT algorithms, *International Journal of Numerical Modelling: Electronic Networks, Devices and Fields*, Vol. 11, pp. 153-166, (1998)

[112] Matthieu Vandamme, The Nanogranular Origin of Concrete Creep: A Nanoindentation Investigation of Microstructure and Fundamental Properties of Calcium-Silicate-Hydrates, Ph.D. Thesis, Massachusetts Institute of Technology, (2008)

[113] M. Vandamme, F.-J. Ulm, Nanogranular Origin of Concrete Creep, *Proceedings of the national Academy of Sciences of the United States of America*, Vol. 106 (26), pp. 10552-10557, (2009)

[114] M. Vandamme, C. A. Tweedie, G. Constantinides, F.-J. Ulm, K. J. Van Vliet, Quantifying Plasticity-independent Creep Compliance and Relaxation of Viscoelastoplastic Materials Under Contact Loading, *Journal of Materials Research*, Vol. 27 (1), pp. 302-312, (2012)

[115] J. A. Williams, Analytical Models of Scratch Hardness, *Tribology International*, Vol. 29, No. 8, pp. 675-694, (1996)

[116] M. Wong, G. T. Lim, J. N. Reddy and H.-J. Sue, A New Test Methodology for Evaluating Scratch Resistance of Polymers, *Wear*, Vol. 256, pp. 1214-1227, (2004)

[117] F.-J. Ulm and R. Pelleng, X-Shale Project - Year 1, Progress Report, (2012)

[118] H. Zaidi, A. Djamai, K. J. Chin and T. Mathia, Characterization of DLC Coating Adherence by Scratch Testing, *Tribology International*, Vol. 39, pp. 124-128, (2006)

[119] Sam Zhang, Deen Sun, Yongqing Fu, Hejun Du, Toughness Measurements of Thin Films: a Critical Review, Surface and Coatings Technology, Vol. 198, pp. 74-84, (2005)

[120] C. Zhixi, C. Mian, J. Yan, H. Rongzun, Determination of Rock Fracture Toughness and its Relationship with Acoustic Velocity, *International Journal of Rock Mechanics and Mining Sciences*, Vol. 34 (3-4), (1997)

Appendix A

Fracture Scaling for Axisymmetric Scratch Probe

The goal of this Chapter is to provide an analytical expression of the energy release rate in the case of scratch tests with an axisymmetric and when the vertical force influences the fracture process. For this purpose spherical coordinates are used to represent the probe-material interface. Then an Airy stress function is used to calculate the stress, strain and displacement fields. Finally the energy release rate is evaluated using a J-integral.

A.1 Geometric description

From the self-similarity analysis the shape of an axisymmetric probe can be described by:

$$d(r) = Br^{\epsilon} \tag{A.1}$$

Therefore we will use the following parametrization of the interface:

$$x = r\cos\phi, \quad z = -\frac{d}{2} + Br^{\epsilon} \tag{A.2}$$

$$r = 0 \ldots \left(\frac{d}{B}\right)^{\frac{1}{\epsilon}}, \quad \phi = -\frac{\pi}{2} \ldots \frac{\pi}{2} \tag{A.3}$$

The differential element:

$$ds = \frac{ds}{dr}dr = \sqrt{1 + (\epsilon B r^{\epsilon-1})^2}dr$$

and the outward unit normal is:

$$\underline{n} = -\frac{\epsilon B r^{\epsilon-1}\cos\phi}{\sqrt{1 + (\epsilon B r^{\epsilon-1})^2}}\,\underline{e}_r + \frac{1}{\sqrt{1 + (\epsilon B r^{\epsilon-1})^2}}\,\underline{e}_z$$

The differential surface element is $da = r\, d\phi\, ds$.

A.2 Integrals of reference

The table below lists some useful integrals that will be used to provide a closed form expression of the energy release rate. A demonstration of the results is provided later in section A.6.

A.3 Airy stress function

The airy stress function is given by:

$$\varphi(x,z) = -bx\left(z^3 - \frac{3}{4}zd^2\right) + cz^2 \tag{A.4}$$

Integral	Expression	Value
$I_1 = \int_{Interface} n_x da$	$f_1(\epsilon)\left(\frac{d}{B}\right)^{\frac{1}{\epsilon}} d$	$f_1(\epsilon) = -\frac{2\epsilon}{\epsilon+1}$
$I_2 = \int_{Interface} n_z da$	$f_2(\epsilon)\left(\frac{d}{B}\right)^{\frac{2}{\epsilon}}$	$f_2(\epsilon) = \frac{\pi}{2}$
$I_3 = \int_{Interface} n_z\ z^2 da$	$f_3(\epsilon)\left(\frac{d}{B}\right)^{\frac{2}{\epsilon}} d^2$	$f_3(\epsilon) = \frac{\pi}{8}\frac{\epsilon^2-\epsilon+2}{(\epsilon+2)(\epsilon+1)}$
$I_4 = \int_{Interface} n_x z^2\ da$	$f_4(\epsilon)\left(\frac{d}{B}\right)^{\frac{1}{\epsilon}} d^3$	$f_4(\epsilon) = -\frac{1}{2}\frac{\epsilon(2\epsilon^2+\epsilon+1)}{(\epsilon+1)(2\epsilon+1)(3\epsilon+1)}$
$I_5 = \int_{Interface} n_z xz\ da$	$f_5(\epsilon)\left(\frac{d}{B}\right)^{\frac{3}{\epsilon}} d$	$f_5(\epsilon) = -\frac{1}{3}\frac{\epsilon-3}{\epsilon+3}$
$I_6 = \int_{Interface} n_x xz\ da$	$f_6(\epsilon)\left(\frac{d}{B}\right)^{\frac{2}{\epsilon}} d^2$	$f_6(\epsilon) = -\frac{\pi}{4}\frac{\epsilon}{(\epsilon+2)(\epsilon+1)}$
$I_7 = \int_{Interface} n_z xz^3\ da$	$f_7(\epsilon)\left(\frac{d}{B}\right)^{\frac{3}{\epsilon}} d^3$	$f_7(\epsilon) = -\frac{1}{12}\frac{2\epsilon^3-5\epsilon^2-9}{(\epsilon+3)(2\epsilon+3)(\epsilon+1)}$
$I_8 = \int_{Interface} n_x x^2 z^2\ da$	$f_8(\epsilon)\left(\frac{d}{B}\right)^{\frac{3}{\epsilon}} d^3$	$f_8(\epsilon) = -\frac{1}{9}\frac{\epsilon(2\epsilon^2+3\epsilon+9)}{(\epsilon+3)(2\epsilon+3)(\epsilon+1)}$
$I_9 = \int_{Interface} n_x z^4\ da$	$f_9(\epsilon)\left(\frac{d}{B}\right)^{\frac{1}{\epsilon}} d^5$	$f_9(\epsilon) = -\frac{\epsilon}{8}\frac{24\epsilon^4+18\epsilon^3+23\epsilon^2+6\epsilon+1}{(\epsilon+1)(2\epsilon+1)(3\epsilon+1)(4\epsilon+1)(5\epsilon+1)}$
$I_{10} = \int_{Interface} n_x x^2\ da$	$f_{10}(\alpha)\left(\frac{d}{B}\right)^{\frac{3}{\epsilon}} d$	$f_{10}(\epsilon) = -\frac{4}{3}\frac{\epsilon}{\epsilon+3}$

Table A.1: Integrals of reference for the derivation of the analytical expression of the energy release rate

The stress field is given by:

$$\sigma_{xx} = -6bxz + 2c \tag{A.5}$$

$$\sigma_{xz} = b\left(3z^2 - \frac{3}{4}d^2\right) \tag{A.6}$$

$$\sigma_{zz} = 0 \tag{A.7}$$

$$\tag{A.8}$$

Where the constant b and c are related to the vertical and horizontal forces by applying the traction boundary conditions at the probe-material interface. The Interface boundary condition reads:

$$F_T = \int_{Interface} (\sigma_{xx} n_x + \sigma_{xz} n_z)\, da \tag{A.9}$$

$$-F_V = \int_{Interface} (\sigma_{xz} n_x)\, da \tag{A.10}$$

By replacing the stress components by tehir expressions provided above, it follows:

$$
\begin{aligned}
F_T &= \int_{Interface} \left[\left(-6bxz + 2c\right) n_x + b\left(3z^2 - \frac{3}{4}d^2\right) n_z \right] da \\
&= -6bI_6 + 2cI_1 + b\left(3I_3 - \frac{3}{4}d^2 I_2\right) \\
&= 2cI_1 + b\left(-\frac{3}{4}d^2 I_2 + 3I_3 - 6I_6\right) \\
&= 2cf_1(\epsilon)\left(\frac{d}{B}\right)^{\frac{1}{\epsilon}} d + b\left[-\frac{3}{4}f_2(\epsilon)\left(\frac{d}{B}\right)^{\frac{2}{\epsilon}} d^2 + 3f_3(\epsilon)\left(\frac{d}{B}\right)^{\frac{2}{\epsilon}} d^2 - 6f_6(\epsilon)\left(\frac{d}{B}\right)^{\frac{2}{\epsilon}} d^2\right] \\
&= 2cf_1(\epsilon)\left(\frac{d}{B}\right)^{\frac{1}{\epsilon}} d + 3b\left(\frac{d}{B}\right)^{\frac{2}{\epsilon}} d^2 \left[-\frac{1}{4}f_2(\epsilon) + f_3(\epsilon) - 2f_6(\epsilon)\right] \\
&= -\frac{4\epsilon}{\epsilon+1}c\left(\frac{d}{B}\right)^{\frac{1}{\epsilon}} d + 3b\left(\frac{d}{B}\right)^{\frac{2}{\epsilon}} d^2 \left[-\frac{1}{4}\frac{\pi}{2} + \frac{\pi}{8}\frac{\epsilon^2 - \epsilon + 2}{(\epsilon+2)(\epsilon+1)} + (-2)(-1)\frac{\pi}{4}\frac{\epsilon}{(\epsilon+2)(\epsilon+1)}\right] \\
&= -\frac{4\epsilon}{\epsilon+1}c\left(\frac{d}{B}\right)^{\frac{1}{\epsilon}} d
\end{aligned}
$$

Therefore

$$
c = -\frac{\epsilon+1}{4\epsilon}\frac{F_T}{\left(\frac{d}{B}\right)^{\frac{1}{\epsilon}} d} \tag{A.11}
$$

In the same way:

$$\begin{aligned}
-F_V &= \int_{Interface} (\sigma_{xz} n_x)\, da \\
&= \int_{Interface} \left[b\left(3z^2 - \frac{3}{4}d^2\right) n_x \right] da \\
&= b\left(3I_4 - \frac{3}{4}d^2\, I_1\right) \\
&= b\left[3f_4(\epsilon)\left(\frac{d}{B}\right)^{\frac{1}{\epsilon}} d^3 - \frac{3}{4}d^2 f_1(\epsilon)\left(\frac{d}{B}\right)^{\frac{1}{\epsilon}} d\right] \\
&= 3b\left(\frac{d}{B}\right)^{\frac{1}{\epsilon}} d^3 \left[f_4(\epsilon) - \frac{1}{4}f_1(\epsilon)\right] \\
&= 3b\left(\frac{d}{B}\right)^{\frac{1}{\epsilon}} d^3 \left[-\frac{1}{2}\frac{\epsilon(2\epsilon^2+\epsilon+1)}{(\epsilon+1)(2\epsilon+1)(3\epsilon+1)} - \frac{1}{4}(-1)\frac{2\epsilon}{\epsilon+1}\right] \\
&= 3b\left(\frac{d}{B}\right)^{\frac{1}{\epsilon}} d^3 \frac{2\epsilon^2}{(2\epsilon+1)(3\epsilon+1)}
\end{aligned}$$

Therefore:

$$b = -\frac{(2\epsilon+1)(3\epsilon+1)}{6\epsilon^2} \frac{F_V}{\left(\frac{d}{B}\right)^{\frac{1}{\epsilon}} d^3} \tag{A.12}$$

A.4 J-Integral

Having derived the expression of the stress components, we will evaluate the j-Integral. The integrand in the J-Integral is:

$$j = \psi n_x - \underline{T}\frac{\partial \underline{\xi}}{\partial x}$$

The first term of the integrand j is $j_1 = \psi n_x = \left[\kappa \frac{\sigma_{xx}^2}{2E} + (1+\nu)\frac{\sigma_{xz}^2}{E}\right]$. The second term is :

$$j_2 = -\underline{T}\frac{\partial \underline{\xi}}{\partial x} = -(\sigma_{xx}n_x + \sigma_{xz}n_z)\frac{1}{E}\left(-(1+\nu)\varphi_{,xx} + \kappa V_{,xz}\right) - \sigma_{xz}n_x \frac{1}{E}\left(-(1+\nu)\varphi_{,zx} + \kappa V_{,xx}\right)$$

Knowing that: $\varphi_{,xx} = \sigma_{zz} = 0$, $\varphi_{,xz} = -\sigma_{xz}$ and $V_{,xz} = \Delta\varphi = \varphi_{,xx} + \varphi_{,zz} = \sigma_{xx}$, we can make the following simplification:

$$j_2 = -\kappa\frac{\sigma_{xx}}{E}\left(\sigma_{xx}n_x + \sigma_{xz}n_z\right) - \frac{\sigma_{xz}}{E}n_x\left((1+\nu)\sigma_{xz} + \kappa V_{,xx}\right)$$

Finally:

$$j = j_1 + j_2 = -\frac{\kappa}{E}\left[\frac{\sigma_{xx}^2}{2}n_x + \sigma_{xx}\sigma_{xz}n_z + \sigma_{xz}V_{,xx}n_x\right]$$

If we replace σ_{xx},σ_{xz} and $V_{,xx}$ by their respective values, it comes:

$$\begin{aligned} j = &-\frac{\kappa}{E}\left[2n_x c^2 + bc\left(-\frac{3}{2}d^2\ n_z + 6\ n_z z^2 - 12\ n_x xz\right) + b^2\left(\frac{9}{4}d^2\ n_x z^2 - \frac{9}{4}d^2\ n_x x^2\right)\right] \\ &-\frac{\kappa}{E}b^2\left(+\frac{9}{2}d^2\ n_z xz - 9\ n_x z^4 - 18\ n_z xz^3 + 27 n_x x^2 z^2\right) \end{aligned}$$

Therefore the J-Integral $J = \int_{Interface} j da$ is related to the integrals defined in section A.2 by:

$$\begin{aligned} J = &-\frac{\kappa}{E}\left[2I_1 c^2 + bc\left(-\frac{3}{2}d^2\ I_2 + 6\ I_3 - 12\ I_6\right) + b^2\left(\frac{9}{4}d^2\ I_4 - \frac{9}{4}d^2\ I_{10}\right)\right] \\ &-\frac{\kappa}{E}b^2\left(\frac{9}{2}d^2\ I_5 - 9\ I_9 - 18\ I_7 + 27 I_8\right) \end{aligned} \tag{A.13}$$

that can be rewritten:

$$J = J_{c^2} + J_{bc} + J_{b^2}$$

There is three terms: one in c^2, one in bc and one in b^2.

A.4.1 Term in c^2

$$
\begin{aligned}
J_{c^2} &= -\frac{\kappa}{E} 2 I_1 c^2 \\
&= -\frac{\kappa}{E}(2)(-1)\frac{2\epsilon}{\epsilon+1}\left(\frac{d}{B}\right)^{\frac{1}{\epsilon}} d\, c^2 \\
&= 2\frac{\kappa}{E}\frac{2\epsilon}{\epsilon+1}\left(\frac{d}{B}\right)^{\frac{1}{\epsilon}} d \left[-\frac{\epsilon+1}{4\epsilon}\frac{F_T}{\left(\frac{d}{B}\right)^{\frac{1}{\epsilon}} d}\right]^2 \\
&= \frac{\kappa}{E}\frac{\epsilon+1}{4\epsilon}\frac{F_T^2}{\left(\frac{d}{B}\right)^{\frac{1}{\epsilon}} d}
\end{aligned}
$$

A.4.2 Term in bc

$$
\begin{aligned}
J_{bc} &= -\frac{\kappa}{E} bc \left[-\frac{3}{2} d^2\, I_2 + 6\, I_3 - 12\, I_6\right] \\
&= -\frac{\kappa}{E} bc \left[-\frac{3}{2} d^2\, f_2(\epsilon) \left(\frac{d}{B}\right)^{\frac{2}{\epsilon}} + 6 f_3(\epsilon) \left(\frac{d}{B}\right)^{\frac{2}{\epsilon}} d^2 - 12 f_6(\epsilon)\left(\frac{d}{B}\right)^{\frac{2}{\epsilon}} d^2\right] \\
&= -\frac{\kappa}{E} bc \left(\frac{d}{B}\right)^{\frac{2}{\epsilon}} d^2 \left[-\frac{3}{2} f_2(\epsilon) + 6 f_3(\epsilon) - 12 f_6(\epsilon)\right] \\
&= -\frac{\kappa}{E} bc \left(\frac{d}{B}\right)^{\frac{2}{\epsilon}} d^2 \left[-\frac{3}{2}\frac{\pi}{2} + 6\frac{\pi}{8}\frac{\epsilon^2-\epsilon+2}{(\epsilon+2)(\epsilon+1)} - 12(-1)\frac{\pi}{4}\frac{\epsilon}{(\epsilon+2)(\epsilon+1)}\right] \\
&= -\frac{\kappa}{E} bc \left(\frac{d}{B}\right)^{\frac{2}{\epsilon}} d^2 \frac{3\pi}{4}\left[-1 + \frac{\epsilon^2-\epsilon+2}{(\epsilon+2)(\epsilon+1)} + 4\frac{\epsilon}{(\epsilon+2)(\epsilon+1)}\right] \\
&= -\frac{\kappa}{E} bc \left(\frac{d}{B}\right)^{\frac{2}{\epsilon}} d^2 \frac{3\pi}{4}\left[-1 + \frac{\epsilon^2+3\epsilon+2}{(\epsilon+2)(\epsilon+1)}\right] \\
&= 0
\end{aligned}
$$

A.4.3 Term in b^2

$$\begin{aligned} J_{b^2} &= -\frac{\kappa}{E} b^2 \left(\frac{9}{4} d^2 \, I_4 - \frac{9}{4} d^2 \, I_{10} + \frac{9}{2} d^2 \, I_5 - 9 \, I_9 - 18 \, I_7 + 27 I_8 \right) \\ &= -9 \frac{\kappa}{E} b^2 \left[\frac{d^2}{4} \left(I_4 - I_{10} + 2 I_5 \right) + \left(-I_9 - 2 I_7 + 3 I_8 \right) \right] \\ &= -9 \frac{\kappa}{E} b^2 I \end{aligned}$$

On the one hand,

$$I_4 - I_{10} + 2 I_5 = f_4(\epsilon) \left(\frac{d}{B} \right)^{\frac{1}{\epsilon}} d^3 - f_{10}(\alpha) \left(\frac{d}{B} \right)^{\frac{3}{\epsilon}} d + 2 f_5(\epsilon) \left(\frac{d}{B} \right)^{\frac{3}{\epsilon}} d$$

So

$$\frac{d^2}{4} \left(I_4 - I_{10} + 2 I_5 \right) = f_4(\epsilon) \left(\frac{d}{B} \right)^{\frac{1}{\epsilon}} \frac{d^5}{4} - f_{10}(\alpha) \left(\frac{d}{B} \right)^{\frac{3}{\epsilon}} \frac{d^3}{4} + f_5(\epsilon) \left(\frac{d}{B} \right)^{\frac{3}{\epsilon}} \frac{d^3}{2}$$

On the other hand

$$\left(-I_9 - 2 I_7 + 3 I_8 \right) = -f_9(\epsilon) \left(\frac{d}{B} \right)^{\frac{1}{\epsilon}} d^5 - 2 f_7(\epsilon) \left(\frac{d}{B} \right)^{\frac{3}{\epsilon}} d^3 + 3 f_8(\epsilon) \left(\frac{d}{B} \right)^{\frac{3}{\epsilon}} d^3$$

By summing the two quantities, it comes:

$$I = \left[\frac{1}{4} f_4(\epsilon) - f_9(\epsilon) \right] \left(\frac{d}{B} \right)^{\frac{1}{\epsilon}} d^5 + \left[-\frac{1}{4} f_{10}(\alpha) + \frac{1}{2} f_5(\epsilon) - 2 f_7(\epsilon) + 3 f_8(\epsilon) \right] \left(\frac{d}{B} \right)^{\frac{3}{\epsilon}} d^3$$

Knowing that:

$$\frac{1}{4} f_4(\epsilon) - f_9(\epsilon) = -\frac{1}{2} \frac{\epsilon^2 (4\epsilon^2 + \epsilon + 1)}{(2\epsilon + 1)(3\epsilon + 1)(4\epsilon + 1)(5\epsilon + 1)}$$

and

$$-\frac{1}{4} f_{10}(\alpha) + \frac{1}{2} f_5(\epsilon) - 2 f_7(\epsilon) + 3 f_8(\epsilon) = 0$$

it comes

$$J_{b^2} = \frac{\kappa}{E} b^2 \frac{9}{2} \frac{\epsilon^2(4\epsilon^2+\epsilon+1)}{(2\epsilon+1)(3\epsilon+1)(4\epsilon+1)(5\epsilon+1)} \left(\frac{d}{B}\right)^{\frac{1}{\epsilon}} d^5$$

and the expression of b^2 is:

$$b^2 = \left[-\frac{(2\epsilon+1)(3\epsilon+1)}{6\epsilon^2} \frac{F_V}{\left(\frac{d}{B}\right)^{\frac{1}{\epsilon}} d^3} \right]^2$$

Thus

$$J_{b^2} = \frac{\kappa}{E} \frac{1}{8} \frac{(4\epsilon^2+\epsilon+1)(2\epsilon+1)(3\epsilon+1)}{\epsilon^2(4\epsilon+1)(5\epsilon+1)} \frac{F_V^2}{\left(\frac{d}{B}\right)^{\frac{1}{\epsilon}} d}$$

Therefore the values of the J-Integral is:

$$\begin{aligned} J &= J_{c^2} + J_{bc} + J_{b^2} \\ &= \frac{\kappa}{E} \frac{\epsilon+1}{4\epsilon} \frac{F_T^2}{\left(\frac{d}{B}\right)^{\frac{1}{\epsilon}} d} + \frac{\kappa}{E} \frac{1}{8} \frac{(4\epsilon^2+\epsilon+1)(2\epsilon+1)(3\epsilon+1)}{\epsilon^2(4\epsilon+1)(5\epsilon+1)} \frac{F_V^2}{\left(\frac{d}{B}\right)^{\frac{1}{\epsilon}} d} \\ &= \frac{\kappa}{E} \frac{\epsilon+1}{4\epsilon} \frac{F_T^2}{\left(\frac{d}{B}\right)^{\frac{1}{\epsilon}} d} \left[1 + \frac{1}{2} \frac{(4\epsilon^2+\epsilon+1)(2\epsilon+1)(3\epsilon+1)}{\epsilon(\epsilon+1)(4\epsilon+1)(5\epsilon+1)} \frac{F_V^2}{F_T^2} \right] \end{aligned}$$

Finally

$$J = \frac{\kappa}{E} \frac{\epsilon+1}{4\epsilon} \frac{F_T^2}{\left(\frac{d}{B}\right)^{\frac{1}{\epsilon}} d} \left[1 + \frac{1}{2} \frac{(4\epsilon^2+\epsilon+1)(2\epsilon+1)(3\epsilon+1)}{\epsilon(\epsilon+1)(4\epsilon+1)(5\epsilon+1)} \frac{F_V^2}{F_T^2} \right] \tag{A.14}$$

A.5 Energy release rate

The energy release rate is related to the J-Integral by:

$$G = \frac{J}{p} \tag{A.15}$$

where p is the perimeter that is given by:

$$p(d) = \left(\frac{d}{B}\right)^{\frac{1}{\epsilon}} \beta \quad \beta = 2\int_0^1 \sqrt{1+\epsilon^2 d^2 \left(\frac{d}{B}\right)^{-\frac{2}{\epsilon}} x^{2\epsilon-2}}\, dx \tag{A.16}$$

Therefore the energy release rate is given by:

$$\begin{aligned} G &= \frac{\kappa}{E}\frac{\epsilon+1}{4\beta\epsilon}\frac{F_T^2}{\left(\frac{d}{B}\right)^{\frac{2}{\epsilon}} d}\left[1+\frac{1}{2}\frac{(4\epsilon^2+\epsilon+1)(2\epsilon+1)(3\epsilon+1)}{\epsilon(\epsilon+1)(4\epsilon+1)(5\epsilon+1)}\frac{F_V^2}{F_T^2}\right] \\ &= \frac{\kappa}{E}\frac{\epsilon+1}{4\beta}\frac{1}{\epsilon B}\frac{F_T^2}{\left(\frac{d}{B}\right)^{\frac{2}{\epsilon}+1}}\left[1+\frac{1}{2}\frac{(4\epsilon^2+\epsilon+1)(2\epsilon+1)(3\epsilon+1)}{\epsilon(\epsilon+1)(4\epsilon+1)(5\epsilon+1)}\frac{F_V^2}{F_T^2}\right] \end{aligned}$$

Finally

$$G = \frac{\kappa}{E}\frac{\epsilon+1}{4\beta}(\epsilon B)^{-1}\left(\frac{B}{d}\right)^{\frac{2}{\epsilon}+1} F_T^2\left[1+\frac{1}{2}\frac{(4\epsilon^2+\epsilon+1)(2\epsilon+1)(3\epsilon+1)}{\epsilon(\epsilon+1)(4\epsilon+1)(5\epsilon+1)}\frac{F_V^2}{F_T^2}\right] \tag{A.17}$$

A.6 Integrals of reference-demonstration

In this section we demonstrate the analytical expressions for the integrals of reference that were presented in Table A.2.

A.6.1 Integral I_1

$$I_1 = \int_{Interface} n_x da \tag{A.18}$$

We have

$$I_1 = \int_{r=0}^{(d/B)^{1/\epsilon}} \int_{\phi=-\pi/2}^{\phi=\pi/2} n_x r d\phi ds = \int_{r=0}^{(d/B)^{1/\epsilon}} \int_{\phi=-\pi/2}^{\phi=\pi/2} -B\epsilon r^{\epsilon-1}\cos\phi\, r d\phi dr = \int_{r=0}^{(d/B)^{1/\epsilon}} -2B\epsilon r^{\epsilon}\, dr$$

Finally:

$$I_1 = -2\frac{\epsilon}{\epsilon+1}d\left(\frac{d}{B}\right)^{\frac{1}{\epsilon}} \tag{A.19}$$

A.6.2 Integral I_2

$$I_2 = \int_{Interface} n_z da \tag{A.20}$$

We have

$$I_1 = \int_{r=0}^{(d/B)^{1/\epsilon}} \int_{\phi=-\pi/2}^{\phi=\pi/2} n_z r d\phi ds = \int_{r=0}^{(d/B)^{1/\epsilon}} \int_{\phi=-\pi/2}^{\phi=\pi/2} 1 \; r d\phi dr$$

Finally

$$I_2 = \frac{\pi}{2}\left(\frac{d}{B}\right)^{\frac{2}{\epsilon}} \tag{A.21}$$

A.6.3 Integral I_3

$$I_3 = \int_{Interface} n_z z^2 \; da \tag{A.22}$$

We have

$$
\begin{aligned}
I_3 &= \int_{r=0}^{(d/B)^{1/\epsilon}} \int_{\phi=-\pi/2}^{\phi=\pi/2} n_z z^2 r d\phi ds \\
&= \int_{r=0}^{(d/B)^{1/\epsilon}} \int_{\phi=-\pi/2}^{\phi=\pi/2} 1 \times \left(-\frac{d}{2} + Br^{\epsilon}\right)^2 r d\phi dr \\
&= \int_{r=0}^{(d/B)^{1/\epsilon}} \pi \left[\frac{d^2}{4} - dBr^{\epsilon} + B^2 r^{2\epsilon}\right] r dr \\
&= \frac{\pi}{2}\frac{d^2}{4}\left(\frac{d}{B}\right)^{\frac{2}{\epsilon}} - \frac{\pi}{\epsilon+2} dB \left(\frac{d}{B}\right)^{\frac{\epsilon+2}{\epsilon}} + \frac{\pi}{2\epsilon+2} B^2 \left(\frac{d}{B}\right)^{\frac{2\epsilon+2}{\epsilon}} \\
&= \pi \left(\frac{d}{B}\right)^{\frac{2}{\epsilon}} d^2 \left[\frac{1}{8} - \frac{1}{\epsilon+2} + \frac{1}{2\epsilon+2}\right]
\end{aligned}
$$

Finally

$$
I_3 = \frac{\pi}{8} \frac{\epsilon^2 - \epsilon + 2}{(\epsilon+2)(\epsilon+1)} \left(\frac{d}{B}\right)^{\frac{2}{\epsilon}} d^2 \tag{A.23}
$$

A.6.4 Integral I_4

$$
I_4 = \int_{Interface} n_x z^2 \, da \tag{A.24}
$$

We have

$$
\begin{aligned}
I_4 &= \int_{r=0}^{(d/B)^{1/\epsilon}} \int_{\phi=-\pi/2}^{\phi=\pi/2} n_x z^2 r d\phi ds \\
&= \int_{r=0}^{(d/B)^{1/\epsilon}} \int_{\phi=-\pi/2}^{\phi=\pi/2} -B\epsilon r^{\epsilon-1}\cos\phi \left(-\frac{d}{2}+Br^{\epsilon}\right)^2 r d\phi dr \\
&= \int_{r=0}^{(d/B)^{1/\epsilon}} -2\epsilon B r^{\epsilon}\left[\frac{d^2}{4} - dBr^{\epsilon} + B^2 r^{2\epsilon}\right] dr \\
&= -2\epsilon B\left[\frac{d^2}{4}\frac{1}{\epsilon+1}\left(\frac{d}{B}\right)^{\frac{\epsilon+1}{\epsilon}} - dB\frac{1}{2\epsilon+1}\left(\frac{d}{B}\right)^{\frac{2\epsilon+1}{\epsilon}} + B^2\frac{1}{3\epsilon+1}\left(\frac{d}{B}\right)^{\frac{3\epsilon+1}{\epsilon}}\right] \\
&= -2\epsilon B d^2\left(\frac{d}{B}\right)^{\frac{\epsilon+1}{\epsilon}}\left[\frac{1}{4}\frac{1}{\epsilon+1} - \frac{1}{2\epsilon+1} + \frac{1}{3\epsilon+1}\right] \\
&= -2\epsilon d^3\left(\frac{d}{B}\right)^{\frac{1}{\epsilon}}\frac{1}{4}\frac{2\epsilon^2+\epsilon+1}{(\epsilon+1)(2\epsilon+1)(3\epsilon+1)}
\end{aligned}
$$

Finally

$$
I_4 = -\frac{1}{2}\frac{\epsilon(2\epsilon^2+\epsilon+1)}{(\epsilon+1)(2\epsilon+1)(3\epsilon+1)}\left(\frac{d}{B}\right)^{\frac{1}{\epsilon}} d^3 \tag{A.25}
$$

A.6.5 Integral I_5

$$
I_5 = \int_{Interface} n_z x z \, da \tag{A.26}
$$

We have

$$
\begin{aligned}
I_5 &= \int_{r=0}^{(d/B)^{1/\epsilon}} \int_{\phi=-\pi/2}^{\phi=\pi/2} n_z \; xz \; r d\phi ds \\
&= \int_{r=0}^{(d/B)^{1/\epsilon}} \int_{\phi=-\pi/2}^{\phi=\pi/2} 1 \times r\cos\phi \left(-\frac{d}{2} + Br^{\epsilon}\right) \; r d\phi dr \\
&= \int_{r=0}^{(d/B)^{1/\epsilon}} 2r^2 \left(-\frac{d}{2} + Br^{\epsilon}\right) \; dr \\
&= 2\left[-\frac{d}{2}\frac{1}{3}\left(\frac{d}{B}\right)^{\frac{3}{\epsilon}} + B\frac{1}{\epsilon+3}\left(\frac{d}{B}\right)^{\frac{\epsilon+3}{\epsilon}}\right] \\
&= 2d\left(\frac{d}{B}\right)^{\frac{3}{\epsilon}}\left[-\frac{1}{6} + \frac{1}{\epsilon+3}\right]
\end{aligned}
$$

Finally

$$
I_5 = -\frac{1}{3}\frac{\epsilon-3}{\epsilon+3}\left(\frac{d}{B}\right)^{\frac{3}{\epsilon}} d \tag{A.27}
$$

A.6.6 Integral I_6

$$
I_6 = \int_{Interface} n_x xz \; da \tag{A.28}
$$

We have

$$
\begin{aligned}
I_6 &= \int_{r=0}^{(d/B)^{1/\epsilon}} \int_{\phi=-\pi/2}^{\phi=\pi/2} n_x \; xz \; r d\phi ds \\
&= \int_{r=0}^{(d/B)^{1/\epsilon}} \int_{\phi=-\pi/2}^{\phi=\pi/2} -B\epsilon r^{\epsilon-1} \cos\phi \; r \cos\phi \left(-\frac{d}{2} + Br^{\epsilon}\right) \; r d\phi dr \\
&= \int_{r=0}^{(d/B)^{1/\epsilon}} -\frac{\pi}{2} B\epsilon r^{\epsilon+1} \left(-\frac{d}{2} + Br^{\epsilon}\right) \; dr \\
&= -\frac{\pi}{2} B\epsilon \left[-\frac{d}{2} \frac{1}{\epsilon+2} \left(\frac{d}{B}\right)^{\frac{\epsilon+2}{\epsilon}} + B \frac{1}{2\epsilon+2} \left(\frac{d}{B}\right)^{\frac{2\epsilon+2}{\epsilon}} \right] \\
&= -\frac{\pi}{2} B\epsilon d \left(\frac{d}{B}\right)^{\frac{\epsilon+2}{\epsilon}} \left[-\frac{1}{2} \frac{1}{\epsilon+2} + \frac{1}{2\epsilon+2} \right] \\
&= -\frac{\pi}{2} B\epsilon d \left(\frac{d}{B}\right)^{\frac{\epsilon+2}{\epsilon}} \frac{1}{2(\epsilon+2)(\epsilon+1)}
\end{aligned}
$$

Finally

$$
I_6 = -\frac{\pi}{4} \frac{\epsilon}{(\epsilon+2)(\epsilon+1)} \left(\frac{d}{B}\right)^{\frac{2}{\epsilon}} d^2 \tag{A.29}
$$

A.6.7 Integral I_7

$$
I_7 = \int_{Interface} n_z x z^3 \; da \tag{A.30}
$$

We have

$$
\begin{aligned}
I_7 &= \int_{r=0}^{(d/B)^{1/\epsilon}} \int_{\phi=-\pi/2}^{\phi=\pi/2} n_z\, xz^3\, r d\phi ds \\
&= \int_{r=0}^{(d/B)^{1/\epsilon}} \int_{\phi=-\pi/2}^{\phi=\pi/2} 1 \times r\cos\phi \left(-\frac{d}{2} + Br^{\epsilon}\right)^3 r d\phi dr \\
&= \int_{r=0}^{(d/B)^{1/\epsilon}} 2r^2 \left[-\frac{d^3}{8} + \frac{3}{4}d^2 Br^{\epsilon} - \frac{3}{2}dB^2 r^{2\epsilon} + B^3 r^{3\epsilon}\right] \\
&= 2\left[-\frac{d^3}{8}\frac{1}{3}\left(\frac{d}{B}\right)^{\frac{3}{\epsilon}} + \frac{3}{4}d^2 B\frac{1}{\epsilon+3}\left(\frac{d}{B}\right)^{\frac{\epsilon+3}{\epsilon}} - \frac{3}{2}dB^2\frac{1}{2\epsilon+3}\left(\frac{d}{B}\right)^{\frac{2\epsilon+3}{\epsilon}} + B^3\frac{1}{3\epsilon+3}\left(\frac{d}{B}\right)^{\frac{3\epsilon+3}{\epsilon}}\right] \\
&= 2d^3\left(\frac{d}{B}\right)^{\frac{3}{\epsilon}}\left[-\frac{1}{24} + \frac{3}{4}\frac{1}{\epsilon+3} - \frac{3}{2}\frac{1}{2\epsilon+3} + \frac{1}{3\epsilon+3}\right] \\
&= -\frac{1}{12}\frac{2\epsilon^3 - 5\epsilon^2 - 9}{(\epsilon+3)(2\epsilon+3)(\epsilon+1)} d^3\left(\frac{d}{B}\right)^{\frac{3}{\epsilon}}
\end{aligned}
$$

Finally

$$
I_7 = -\frac{1}{12}\frac{2\epsilon^3 - 5\epsilon^2 - 9}{(\epsilon+3)(2\epsilon+3)(\epsilon+1)}\left(\frac{d}{B}\right)^{\frac{3}{\epsilon}} d^3 \tag{A.31}
$$

A.6.8 Integral I_8

$$
I_8 = \int_{Interface} n_x x^2 z^2\, da \tag{A.32}
$$

We have

$$
\begin{aligned}
I_8 &= \int_{r=0}^{(d/B)^{1/\epsilon}} \int_{\phi=-\pi/2}^{\phi=\pi/2} n_x\, x^2 z^2\, r d\phi ds \\
&= \int_{r=0}^{(d/B)^{1/\epsilon}} \int_{\phi=-\pi/2}^{\phi=\pi/2} -B\epsilon r^{\epsilon-1} \cos\phi\, r^2 \cos^2\phi \left(-\frac{d}{2} + Br^{\epsilon}\right)^2 r d\phi dr \\
&= \int_{r=0}^{(d/B)^{1/\epsilon}} -\frac{4}{3} B\epsilon r^{\epsilon+2} \left[\frac{d^2}{4} - dBr^{\epsilon} + B^2 r^{2\epsilon}\right] dr \\
&= -\frac{4}{3} B\epsilon \left[\frac{d^2}{4}\frac{1}{\epsilon+3}\left(\frac{d}{B}\right)^{\frac{\epsilon+3}{\epsilon}} - dB\frac{1}{2\epsilon+3}\left(\frac{d}{B}\right)^{\frac{2\epsilon+3}{\epsilon}} + B^2\frac{1}{3\epsilon+3}\left(\frac{d}{B}\right)^{\frac{3\epsilon+3}{\epsilon}}\right] \\
&= -\frac{4}{3} B\epsilon d^2 \left(\frac{d}{B}\right)^{\frac{\epsilon+3}{\epsilon}} \left[\frac{1}{4}\frac{1}{\epsilon+3} - \frac{1}{2\epsilon+3} + \frac{1}{3\epsilon+3}\right] \\
&= -\frac{4}{3} B\epsilon d^2 \left(\frac{d}{B}\right)^{\frac{\epsilon+3}{\epsilon}} \frac{1}{12}\frac{2\epsilon^2+3\epsilon+9}{(\epsilon+3)(2\epsilon+3)(\epsilon+1)}
\end{aligned}
$$

Finally

$$
I_8 = -\frac{1}{9}\frac{\epsilon(2\epsilon^2+3\epsilon+9)}{(\epsilon+3)(2\epsilon+3)(\epsilon+1)}\left(\frac{d}{B}\right)^{\frac{3}{\epsilon}} d^3 \tag{A.33}
$$

A.6.9 Integral I_9

$$
I_9 = \int_{Interface} n_x z^4\, da \tag{A.34}
$$

We have

$$
\begin{aligned}
I_9 &= \int_{r=0}^{(d/B)^{1/\epsilon}} \int_{\phi=-\pi/2}^{\phi=\pi/2} n_x\, z^4\, r d\phi ds \\
&= \int_{r=0}^{(d/B)^{1/\epsilon}} \int_{\phi=-\pi/2}^{\phi=\pi/2} -B\epsilon r^{\epsilon-1}\cos\phi \left(-\frac{d}{2}+Br^{\epsilon}\right)^4 r d\phi dr \\
&= \int_{r=0}^{(d/B)^{1/\epsilon}} -2B\epsilon r^{\epsilon}\left[\frac{d^4}{16}-\frac{d^3}{2}Br^{\epsilon}+\frac{3}{2}d^2B^2r^{2\epsilon}-2dB^3r^{3\epsilon}+B^4r^{4\epsilon}\right] dr \\
&= -2B\epsilon\left[\frac{d^4}{16}\frac{1}{\epsilon+1}\left(\frac{d}{B}\right)^{\frac{\epsilon+1}{\epsilon}}-\frac{d^3}{2}B\frac{1}{2\epsilon+1}\left(\frac{d}{B}\right)^{\frac{2\epsilon+1}{\epsilon}}+\frac{3}{2}d^2B^2\frac{1}{3\epsilon+1}\left(\frac{d}{B}\right)^{\frac{3\epsilon+1}{\epsilon}}\right] \\
&- 2B\epsilon\left[-2dB^3\frac{1}{4\epsilon+1}\left(\frac{d}{B}\right)^{\frac{4\epsilon+1}{\epsilon}}+B^4\frac{1}{5\epsilon+1}\left(\frac{d}{B}\right)^{\frac{5\epsilon+1}{\epsilon}}\right] \\
&= -2B\epsilon d^4\left(\frac{d}{B}\right)^{\frac{\epsilon+1}{\epsilon}}\left[\frac{1}{16}\frac{1}{\epsilon+1}-\frac{1}{2}\frac{1}{2\epsilon+1}+\frac{3}{2}\frac{1}{3\epsilon+1}-\frac{2}{4\epsilon+1}+\frac{1}{5\epsilon+1}\right] \\
&= -2B\epsilon d^4\left(\frac{d}{B}\right)^{\frac{\epsilon+1}{\epsilon}}\frac{1}{16}\frac{24\epsilon^4+18\epsilon^3+23\epsilon^2+6\epsilon+1}{(\epsilon+1)(2\epsilon+1)(3\epsilon+1)(4\epsilon+1)(5\epsilon+1)}
\end{aligned}
$$

Finally

$$
I_9 = -\frac{\epsilon}{8}\frac{24\epsilon^4+18\epsilon^3+23\epsilon^2+6\epsilon+1}{(\epsilon+1)(2\epsilon+1)(3\epsilon+1)(4\epsilon+1)(5\epsilon+1)}\left(\frac{d}{B}\right)^{\frac{1}{\epsilon}} d^5 \tag{A.35}
$$

A.6.10 Integral I_{10}

$$
I_{10} = \int_{Interface} n_x x^2\, da \tag{A.36}
$$

We have

$$
\begin{aligned}
I_{10} &= \int_{r=0}^{(d/B)^{1/\epsilon}} \int_{\phi=-\pi/2}^{\phi=\pi/2} n_x \, x^2 \, r d\phi ds \\
&= \int_{r=0}^{(d/B)^{1/\epsilon}} \int_{\phi=-\pi/2}^{\phi=\pi/2} -B\epsilon r^{\epsilon-1} \cos\phi \, r^2 \cos^2\phi \, r \, d\phi dr \\
&= \int_{r=0}^{(d/B)^{1/\epsilon}} -\frac{4}{3} B\epsilon r^{\epsilon+2} \\
&= -\frac{4}{3} B \frac{\epsilon}{\epsilon+3} \left(\frac{d}{B}\right)^{\frac{\epsilon+3}{\epsilon}}
\end{aligned}
$$

Finally

$$
I_{10} = -\frac{4}{3} \frac{\epsilon}{\epsilon+3} \left(\frac{d}{B}\right)^{\frac{3}{\epsilon}} d \tag{A.37}
$$